GIANLUCA SANTESARTI

# MODELLING OF EXTRUSION-BASED BIOPRINTING VIA QUASI-ANALYTICAL AND FSI COMPUTATIONAL APPROACHES

**PhD Thesis**
**JULY 2023**

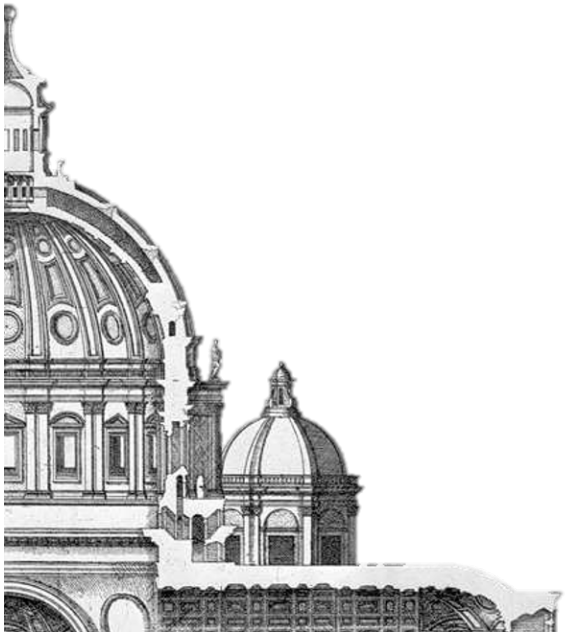

DEPARTMENT OF CIVIL ENGINEERING
AND COMPUTER SCIENCE ENGINEERING

UNIVERSITY OF ROME "TOR VERGATA", ITALY

PHILOSOPHY DOCTORATE IN CIVIL ENGINEERING
XXXV COURSE

XXXV Course of Philosophy Doctorate in Civil Engineering
Department of Civil Engineering and Computer Science Engineering
University of Rome "Tor Vergata", Italy

TOR VERGATA
UNIVERSITY OF ROME

Doctoral Programme in Structural Engineering and Geotechnics

Doctoral Thesis

# MODELLING OF EXTRUSION-BASED BIOPRINTING VIA QUASI-ANALYTICAL AND FSI COMPUTATIONAL APPROACHES

dissertation submitted in partial fulfilment of the
requirements for the degree of Philosophiæ Doctor by

**Gianluca Santesarti**

*PhD Committee:*

Prof. Michele Conti
Prof. Alessio Gizzi
Prof. Gianni Pedrizzetti

*PhD Course Coordinator:*
Prof. Tullia Iori

*Doctoral Programme Coordinator:*
Prof. Paolo Bisegna

*Advisor:*
Prof. Giuseppe Vairo

*Co-Advisors:*
Prof. Roberto Verzicco
Prof. Michele Marino
Prof. Francesco Viola

Academic Year 2021/2022

# Acknowledgements

Before I tell you more about the journey through my PhD research, it is with pleasure and sincere gratitude that I would like to express my acknowledgement to the people who have stood by my side during these years, without them, I certainly would not be here today.

I am grateful to Prof. Giuseppe Vairo and Prof. Roberto Verzicco for their trust. In particular, I thank Prof. Vairo for believing in this research project at the beginning and for his insights into fluid-structure interaction (FSI). I am grateful to Prof. Verzicco for introducing me to the world of immersed boundary (IB) methods; the FSI numerical code developed by his research group is truly an incredible tool. I am very grateful to Prof. Michele Marino for introducing me to the fascinating and multi-disciplinary topic of bioprinting, for the insights into mechanics and modelling, and above all for his constant availability and proactiveness. The support he provides to his students and his willingness to analyse in detail the results obtained are truly an added value. I am very grateful to Prof. Francesco Viola for helping me with the numerical code, without him FSI simulations at low Reynolds numbers would have been really impossible.

I would like to express my thanks to my doctoral roommates for spending this time together, and for their help along the way. I am grateful to the tutoring team managed by Prof. Mauro Chinappi, getting to know you all was a great experience. I thank Prof. Aurélie Carlier and the members of the ESB student committee for the time spent and the activities we did together. The ESB conference in Porto 2022 was really exciting.

On the affective side, I am very grateful to my friends in Fiuggi, Rome and Bologna who accompanied me during this journey and supported me in the most difficult moments, in particular I thank Matteo, Danilo and Simone. I would like to thank the guys from the theatre LAB organised by Cataldo for the pleasant evenings and rehearsals we spent together. Performing De Filippo, Shakespeare and Pirandello with you was wonderful. I heartfelt thank Annamaria for her continuous

support and sustenance, her presence is truly invaluable.

And finally, as the foundations of a house are at the base, so these last thanks at the end of this page are dedicated to my family, for always supporting me. In particular, I am deeply grateful to my mother, for always standing by me and supporting my scientific education.

A last thank you goes to the musical artists listened to during the writing of this manuscript and over the years. I think about Foo Fighters, Lucio Battisti, Fabrizio De André, Pearl Jam, The Strokes, RAMONES, Rino Gaetano, Pink Floyd, The Fiuggi music band, Ligabue, Bach, Holst, John Williams, The Beatles, Hans Zimmer...what a beautiful music, what a beautiful humanity.

I conclude by quoting two sentences from two researchers of the human soul that really strike me

*"Fair lovers, you are fortunately met. Of this discourse we more will hear anon."*

W. S.

*"Ama e ridi se amor risponde, piangi forte se non ti sente, dai diamanti non nasce niente..."*

F. De A.

*Rome, 4 July 2023*
Gianluca Santesarti

# Abstract

Bioprinting is an emerging technology belonging to the class of additive manufacturing (AM) techniques applied to the biofabrication of living tissues. Through the computer-aided design (CAD), cell-laden biocompatible materials are deposited layer-by-layer in 3D scaffolds, miming the complex 3D micro-environment of the extra-cellular matrix (ECM), and allowing cells to proliferate, maturate, differentiate and secrete its own ECM in order to achieve the tissue growth [1–3].

The main aims of bioprinting are declined in several research fields such as tissues and organs transplantation [2], study of pathological conditions in human diseases [4], drug discovery and personalized-medicines development [5], and more recently printing of cultured meat [6] and support to the human space exploration [7].

The main component of this technology is the bio-ink composed by the fluid phase, made up of polymers cytocompatibles and additive chemicals to improve the printing process, and by the solid phase represented by the cells of the specific tissue to reproduce. Among all available bioprinting processes, they can be principally grouped in three categories based on the printing physical principle: the droplet-based bioprinting [8], which uses thermal, piezoelectric or acoustic sources to generate and deposit droplets onto a substrate; the light-assisted bioprinting [9], employing a laser source to irradiate a specific coated metal ribbon to produce droplets falling onto a substrate; the extrusion-based bioprinting (EB) [10], which uses mechanical screw-driven motors or a pneumatic systems to extrudes continuous filaments through a nozzle, usually a syringe equipped with a piston.

In particular, this thesis addresses the extrusion-based process which compared to the other technologies presents the advantage to have an affordable and simple setup, and a wide arrays of bio-inks in terms of viscosity and chemical properties. It is a multi-disciplinary application across biology, chemistry, medicine and engineering disciplines and it presents a multi-scale nature ranging between the cell and the nozzle dimensions. Due to the high number of variables intervening during

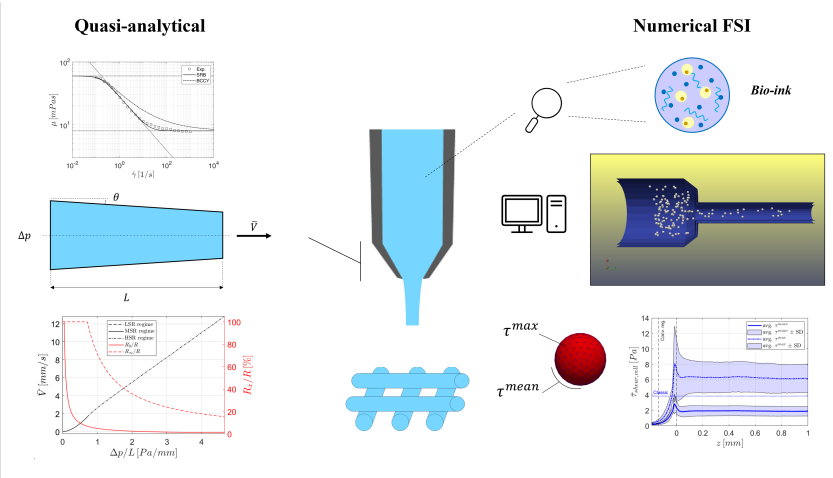


**Figure 1:** Graphical abstract of the modelling approaches presented in this thesis.

the process and specific for each bio-ink, the experimental trial and error optimization is very expensive. Therefore, computational models would allow to reduce the optimization costs accelerating the scale-up process, and to better understand the phenomena occurring during extrusion.

By focusing on the phase upstream the nozzle outlet, several works are present in literature describing the extrusion process by assuming different rheological models for the bio-ink and using different numerical techniques [11–15]. They consider the bio-ink as a homogeneous fluid and characterize its rheological behaviour through non-Newtonian inelastic models. Among the models used, the Bird-Cross-Carreau-Yasuda (BCCY) model provides a more accurate relationship and better fitting capabilities of experimental data. On the other hand, it necessitates an ad hoc optimization procedure for the calibration of model parameters. This requirement is due to its intrinsic problem of parameters identifiability as analysed by Gallagher *et al.*[16], which could in addition determine unreliable flow solutions. Regarding the fluid-structure interaction (FSI) analyses between the fluid and cells, so far only few examples has been found in literature [17–19]. In particular, Abedini *et al.*[17] analysed the cell viability of only a single cell aggregate flowing in a cylindrical nozzle within a power law fluid, and Müller *et al.*[18] evaluated the stress and strain only of a single cell flowing out the nozzle exit.

As shown in Fig. 1, the main aims of this thesis are:

- the presentation of an alternative rheological model developed to solve the parameters identifiability problem of the BCCY model, to have a more physical rheological relationship, and to derive reliable and approximated analytical solutions for bio-ink flows.
- the proposal of a quasi-analytical framework developed to provide a simple and ready-to-use solution for bio-inks flowing in cylindrical and slightly tapered nozzles.
- the presentation of a numerical FSI approach based on the immersed bound-

ary method (IB) developed to have a more detailed description of stresses experienced by a population of cells during the extrusion through a convergent-shaped nozzle and flowing in a BCCY fluid, at the expense of a higher computational cost.

Specifically, the alternative model presents a more reliable physical interpretation of rheological parameters and very good fitting capabilities with a coefficient of determination $R^2_{LMAPE}$ of 93.1 %. The quasi-analytical solution applied to cylindrical nozzles has been validated through parametric comparisons with numerical results, showing in the worst case a maximum error on the extrusion velocity about 3.5 %. It has been also applied and validated to reproduce an experimental bioprinting setup through a conical nozzle, giving a pressure drop 6.4 % greater than the experimental value. Regarding the FSI model, the comparison between the numerical results and the classic approach about the cell shear stresses shows a very different behaviour. In the convergent region of the nozzle, the FSI analyses report unsteady results with peak values of shear stresses. Next, in the following needle part of the nozzle, the classic solution overestimates and underestimates the mean and maximum shear stresses acting on cells respectively. In particular, the maximum to mean shear stress ratio can reach a value of 328 %, highlighting the need of a FSI approach to have a more accurate and detailed analysis of the cell dynamics during the extrusion.

**Keywords.** Extrusion-based bioprinting; rheological modelling; quasi-analytical solutions; FSI in particle flows; immersed-boundary method.

# Contents

# Chapter 1

# Introduction

This chapter introduces the main bioprinting technologies currently employed to reproduce human tissues through the 3D printing of cell-laden scaffolds. It focuses in particular on the extrusion-based bioprinting processe assisted by a pneumatic system, namely through the application of a dispensing pressure on the printing nozzle. The Section 1.2 briefly recalls the typology of used bio-inks made up by the biocompatible polymeric fluid and cells. In particular, it describes the most common hydrogel-based bio-inks and the crosslinking strategies adopted in extrusion process. Next, the Section 1.3 illustrates the biological structure of the human eukaryotic cell. Then, the Section 1.4 presents a summary on the state-of-the-art on the computational modelling of extrusion bioprinting. The chapter ends with the thesis organization and goals reported in Section 1.5.

## 1.1 Bioprinting

Bioprinting is the class of tissue engineering technologies based on the additive manufacturing process for the fabrication of cell-laden scaffolds. As shown for example in Fig. 1.1, through the computer-aided (CAD) technology living material is deposited layer-by-layer with an established organization [10, 20, 21].

The main aims of bioprinting technology are the tissues and organs transplantation [2], the understanding of pathological conditions in human diseases [4, 23–25], the study of drug action mechanisms and the development of patient-specific medicines [5], and more recently the printing of cultured meat [6, 26]; furthermore, since its relevant potentials this technology is also researched to support the human space exploration [7, 27].

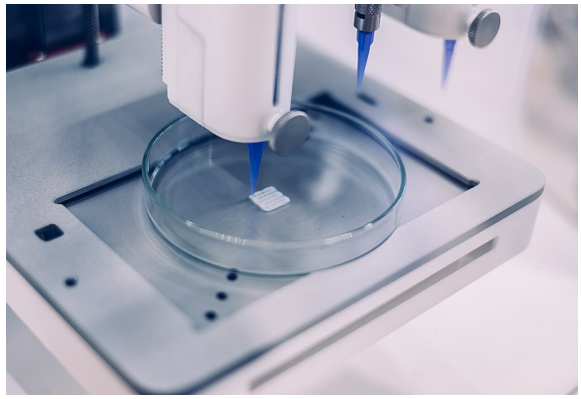

**Figure 1.1:** Bioprinting of a biological scaffold through the extrusion-based process [22].

The suitable scaffold must guarantee an optimal 3D environment for cells to adhere, proliferate, differentiate ans secrete extra cellular matrix [20], by satisfying several and cross disciplinary requirements. It must have a favourable cytocompatibility in terms of pH, absence of toxic agents, degradation capability in the human body, by ensuring an optimal geometrical porosity and interconnectivity to allow the oxygen and nutrient diffusion and metabolic waste removal. It must support the cell adhesion, migration, vascularization and new tissue ingrowth. Furthermore, it must present a structural integrity to not collapse on itself, but at the same time to be soft enough to limit cellular damages during the printing and to increase the deposition velocity in order to scale-up the process.

Among all the bioprinting technologies, they can mainly be grouped in three categories based on their printing principle [20, 28]: the droplet-based bioprinting [8], which uses thermal, piezoelectric or acoustic sources to generate local pressure increments in a cartridge containing the biomaterial to form and deposit droplets onto a substrate with a volume in the magnitude order of $pl$; the light-assisted bioprinting [9], which employs a laser source to irradiate a coated metal ribbon overlying the biomaterial film to generate droplets settling onto a substrate; and the extrusion-based bioprinting (EB) [10], which prints continuous filaments in cylindrical form through a nozzle, usually a syringe, by using or a mechanical screw-driven motor, or a pneumatic system through the application of a dispensing pressure on a piston. In particular, this work is focused on the extrusion-based bioprinting with a pneumatic system, which compared to the other processes present the advantages to have an affordable and simple setup, a high deposition speed, a room temperature process avoiding so thermal damages to the cells, and a wide variety of printing materials in terms of viscosity and chemical properties [20]. On the other hand, it is affected by a lower printing resolution (the smallest nozzle diameter used is in the order of $100\,\mu m$), the nozzle clogging defect at higher cell densities, and the difficulty to print highly complex shapes with overhangs and voids [29].

Regardless the specific technology used, the main component of bioprinting is the bio-ink composed by the fluid phase, made up of polymers cytocompatibles

and additive chemicals to improve the printing process, and by the solid phase represented by the cells of the specific tissue to reproduce. Therefore, the bio-ink has to satisfy simultaneously both types of requirements deriving from the specific fabrication process chosen and from the biological constraints of cells [30]. So far, a wide variety of bio-inks has been developed by the biological researchers working in bioprinting field and they can be classified in four main categories [10]. The first and most commonly used group is represented by the hydrogel-based bio-inks, which thanks to their capability to retain a high water-content and to be degraded upon chemical, physical, or enzymatic stimuli offer a suitable microenvironment for the tissue growth. Then, there are the decellularized-extra cellular matrix (dECM) bio-inks [31] obtained through the removal of cell content from the ECM of tissue target. They naturally simulate the complex biological microenvironment formed by the functional and structural proteins, but may cause immunoreactions when implanted and present low mechanical properties, indedd they are usually co-printed with other polymers such as the polycaprolactone (PCL) to obtain a better structural integrity of the scaffold [32, 33]. Recently, another class of bio-inks has been developed by using micro-carriers with different geometries to load and cluster multiple cells together and print them by using a hydrogel medium. They have a great potential to scale-up the process thanks to their high cell proliferation properties but are still limited difficulty to degrade without generate toxic molecules for cells and by the risk of nozzle clogging [10]. The last class is represented by the cell aggregates (also termed cell constructs) composed by an extremely high cell densities. They do not envisage the scaffold generation since they are usually printed via tissue spheroids in a confined space to form in more rapid amount of time the tissue generation, without expect the degradation of the hydrogel. Despite this advantage they present loading problems in the bioprinter cartridge and a tendency to fuse each other during the deposition process. Regarding the kind of cells to load in the bio-ink they should be autologus and patient specific, and available at high density in order to allow a suitable tissue growth [34]. The theoretically could be collect directly as mature cells from the patient, but this method would imply an invasive procedure and the risk of cell damage during the removal. Thus, researchers usually sample stem cells which can be expanded and differentiated in vitro in multiple cell lineages [35]. Commonly stem used are: embryonic stem cells (ESCs), induced pluripotent stem cells (iPSCs) and multipotent adult stem cells [36].

## 1.2 Hydrogels employed in bioprinting

The hydrogels are a class of materials characterized by hydrophilic polymer chains with a high water content [37] which mimics the natural hydrated crosslinked network of the extra-cellular matrix (ECM) [38]. They can be tailored by adding cell-adhesion motifs and cell-proteolytic domains to improve their biological properties in terms of cell adhesion, proliferation and differentiation, and biodegradation allowing the cells to undergo self-assembly and self-organization to form the own natural ECM. In addition, they usually present viscosity properties with a shear-thinning behaviour which reduces the hydraulic resistance during the printing process, resulting in a lower dispensing pressure and lower shear stresses applied

to cells. Furthermore, thanks to their printability can be printed in vascularized networks enabling the perfusion of cell culture media, nutrients, and metabolic waste removal [39]. Based on the origin materials, the hydrogels can be divided into two groups: the natural polymer-based hydrogels and synthetic polymer-based hydrogels. The natural hydrogels in general present better biocompatibility characteristics, but with lower mechanical properties. Common employed hydrogels deriving from natural proteins are: the collagen, used for connective tissue regeneration with a low gelation temperature; and the gelatin (Gel), with a high number of cell adhesion motifs and a reversible thermal gelation due to the hydrogen bonds [40], in addition it is approved by the Food and Drug Administration (FDA) and it is widely used in the meat industry at low cost [41]. Then, other natural polysaccharides-based hydrogels are: the alginate extracted from brown algae with the main characteristic to have a fast gelation rate in ionic solutions such as $CaCl_2$ baths; the hyaluronic acid (HA), used for cartilage and connective tissues; and the chitosan, with antibacterial properties mainly used for wound dressing. While the synthetic hydrogels present better mechanical properties and are more easily processable with the different bioprinting processes. The most common synthetic hydrogel used are: the polyethylene glycol (PEG), which can be crosslinked in ionic solutions and it is approved by FDA; and the pluronic, formed by two hydrophilic blocks (PEO) and a hydrophobic block (PPO) and presents a thermally sensitive sol-gel transition.

In order to improve the structural stability of the hydrogel scaffold, beside to modify the other process variables such as bio-ink composition determining its rheological behaviour, or varying the geometry of the scaffold, the most important strategy is the crosslinking process [42] that consists of increasing the bonds between the polymer chains. Depending on nature of the polymeric backbone and functional groups, the hydrogels could be crosslinked through physical or chemical methods. The physical crosslinking take places through the formation of not-covalent reversible bonds based on hydrogen bonds, hydrophobic effects, ionic bonds through the use of polar solutions (e.g. for the alginate-based bio-inks crosslinked in $CaCl_2$ baths), polymeric chain entanglements or thermally induced sol-gel transition (e.g. for the gelatin-based bio-inks) [43]. They present a better cytocompatibility, even if a lower mechanical improvement of the scaffold. While chemical crosslinking methods form stronger covalent and not reversible bonds, usually through the addition of a crosslinker. One of the most common used crosslinker is the photoinitiator methacrylate (MA) which is activated by the UV light exposure; for example, it is added to gelatin (GelMA) and hylarunic acid (HA-MA) hydrogels to increase their mechanical properties. Their drawback is the inclusion of chemical additives which may be toxic for the cells. In extrusion-based bioprinting the crosslinking is performed downstream the nozzle outlet, and it will not be taken into account in this work.

## 1.3 Biological description of the human cell

The human cells are a complex and dynamic system. They are part of the eukaryotic cells class which are characterized by an internal nucleus as opposite to the prokaryotic cells. The human cells have typically a mean diameter $\bar{D}_{cell} =$

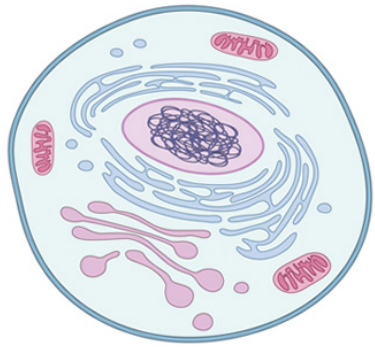

**Figure 1.2:** The main components of an eukaryotic cell: the phospholipid membrane, the organelles immersed in cytoplasm and the nucleus [45].

$5\,\mu m - 20\ \mu m$, and their dimensions can vary from the smallest ones with a $D_{cell} \simeq 2\ \mu m$, as for the sperm and red blood cells, to the biggest ones with a $D_{cell} \simeq 120\ \mu m$, as for the fat and oocyte cells [44]. Starting from outside towards the inside, the essential parts of the human cell are the cellular membrane, the cytoplasm with the immersed organelles and the nucleus as shown in Fig. 1.2.

The cell membrane chemically protects the internal environment from the outside space. It is mainly made up of phospholipids which have a hydrophilic head and two hydrophobic fatty acid tails, which tend to shape a closed surface excluding water molecules from the hydrophobic part and forming a lipid bilayer. In addition, there are also lipid cholesterol molecules in a minor part contributing to stiff the membrane. The lipid bilayer has a very small thickness of around $2\ nm - 10\ nm$, and even if the water molecules inside and outside the cell prevent the membrane lipids from leaving, nothing stop them to swap position each other, giving the membrane a fluid behaviour [44, 46].

In the middle part of the cell there are the organelles, specialized subunits for one or more specific functions (such as mitochondria, ribosomes etc.) which occupy about the 10% of the cell volume and the cytoplasm representing the greater part with a volume around 70% of the cell. The cytoplasm is composed by the cytosol, a water-based gel mainly made up of water with large and small functional molecules, and by the cytoskeleton [44]. The cytoskeleton is an intricate network of protein filaments constituting the mechanical structure of the cell by supporting the large volume of the cytoplasm. It is a not a static structure since the filaments assemble and disappear their self in a matter of minutes depending on the external stimuli and life functions of the cell. The cytoskeleton is anchored to the inner surface of the cell membrane through the spectrin vertices. It is composed by the actin filaments, responsible of the motion and contractive force of the cell, by the microtubules, which help to sort the chromosomes during the cell division, and by the intermediate filaments, which mechanically strength the cell and protect it from the mechanical strains [44]. Then, there is the nucleus with a dimension about the 20% of the cell volume, enclosed within two concentric membranes forming the nuclear envelope. In the nucleus centre there is the nucleolus region wherein the ribomosomal RNA is synthesized afterwards to form ribosomes. The whole nucleus is the information

and control centre of the cell, storing the extremely long polymers of DNA that become visible during the cellular mitosis phase by compacting in chromosomes [44].

## 1.4 Computational modelling of extrusion bioprinting

As described in Sections 1.1, 1.2,1.3, bioprinting is a multi-disciplinary application across biology, chemistry, medicine and engineering disciplines. Furthermore, it presents a multi-scale nature ranging between the cell and the nozzle dimensions. Due to the high number of variables intervening during the process and specific for each bio-ink, the experimental trial and error optimization is very expensive. Therefore, computational models would allow to reduce the optimization costs accelerating the scale-up process. In addition, they could help to have a better understanding of phenomena taking places at cellular microscales since allowing to characterize cell mechano-biological stimulus during extrusion. Among the different bioprinting technologies described in the first paragraph of this chapter, this thesis is focused on the extrusion-based bioprinting, and more specifically on the process assisted by a pneumatic dispensing system.

Several computational approaches have been developed recently to provide *in silico* answers to support the decision of extrusion bioprinting process variables [47–49]. However, it is not possible to model with a single framework all the phases of extrusion bioprinting process, namely the preprinting phase with the development and characterization of bio-ink, the printing phase to form the biological scaffold and the postprinting phase with the crosslinking and incubation stage [50]. The extrusion of bio-ink is a fluid dynamic problem, with a fluid showing both non-Newtonian inelastic and viscoelastic behaviours characterized by a non-linear mechanical response. Furthermore, it is a heterogeneous material mainly composed by the two polymeric and cellular phases, and depending on the nozzle geometry, and on the cell dimensions and density, fluid-structure phenomena may significantly influence the extrusion process. For example, the non-negligible cell dimensions could decrease the flow section, causing a local velocity gradients increment corresponding to greater shear stresses. Afterwards the nozzle outlet, two-phases interaction takes place between the extruded filament and the surrounding air with the surface tension phenomenon influencing the droplet/fiber deposition [48, 51]. Then, the bio-ink is structurally stabilized by crosslinking mechanism which significantly alter their mechanical behaviour, to a such point that is preferable to move from a fluid dynamic description to one based on solid mechanics. After this point, cell activity and tissue generation models should be introduced in the numerical framework to describe the tissue growth.

By focusing on the phase upstream the nozzle outlet, several computational models are present in literature to describe the extrusion process by assuming different rheological models for the bio-ink and using different numerical techniques. Billiet *et al.*[11] and Chiesa *et al.*[12] carried out parametric analyses to study the influence of printing parameters such as dispensing pressure, nozzle diameter, cell density, and temperature on the scaffold printability, by describing the bio-ink vis-

cosity through the non-Newtonian inelastic power law model and using a finite element method (FEM) numerical solver (COMSOL). Gòmez *et al.*[13] analysed the droplet/fiber formation and the influence of material viscosity on the dispensing pressure by assuming a Newtonian behaviour for the bio-ink and adopting a FEM solver (COMSOL) coupled with a level-set method (LT) to describe the two-phase flows dynamics between the bio-ink and air. Ingelsten *et al.*[14] studied the extrusion and laydown of fibers describing the fluid through the viscoelastic PTT model, and using both a finite volume method (FVM) solver coupled the immersed boundary technique (IB), and a volume of fluid method (VOF) to model the two-phase flow. Williams *et al.*[15] analysed a two phase coaxial flow, comparing immiscible and miscible computational models, describing the fluids with inelastic rheological laws (Bird-Cross-Carreau-Yasuda (BCCY) and Carreau respectively), by using a FVM solver (Ansys fluent) coupled with the VOF technique for the immiscible analysis, and a FEM solver (COMSOL) for the miscible model. Regarding the fluid-structure interaction analysis between the fluid and cells, so far only few examples has been found in literature [17–19]. Abedini *et al.*[17] assessed the cell viability of only a single cell aggregate flowing in a cylindrical nozzle by analysing its strains during the extrusion. They assumed a power law behaviour for the fluid and a Neo-Hookean material model for the cell aggregate, considering as elastic constant values those of a single cell nucleus. About the numerical treatment of the fluid-structure coupling at the interface, they used an arbitrary Lagrangian-Eulerian (ALE) formulation. Müller *et al.*[18] evaluated cell stress and strain caused by the elongational stresses of the flow at the nozzle exit, describing the fluid rheological behaviour through the inelastic BCCY model and a hyperelastic neo-Hooken model for cells. They used a Lattice-Boltzmann solver coupled with a IB algorithm for the fluid and a FEM solver for cells.

### 1.4.1 Limitations of the state-of-the-art

State-of-the-art approaches generally assume that the bio-ink is a homogeneous fluid with a rheological behaviour described by the simple power law model [11, 12], thus neglecting the viscosity plateau at low and high shear rates usually exhibited by bio-inks. When more refined relationships are employed, the literature is limited to the five-parameters BCCY model, such as in [15]. However, this approach requires an ad hoc optimization procedure for the parameters calibration, since it suffers from an intrinsic problem of parameters identifiability as reported by Gallagher *et al.*[16], and it may lead to unreliable flow solutions (see results in Section 3.4). Finally, very limited is the literature that considers the bio-ink as heterogeneous and analyses the FSI between the fluid and cells. To the best of author knowledge, only few studies are available, that is [17–19]. In detail, Abedini *et al.*[17] evaluated the extrusion of a single cell aggregate flowing in a cylindrical nozzle and immersed in a power law fluid, Das *et al.*[19] assume the fluid with a Newtonian behaviour, whereas Müller *et al.*[18] analysed the extrusion of a single cell within a BCCY fluid at the nozzle outlet.

## 1.5 Thesis organization and goals

The work carried out in this research starts with the Chapter 2 introducing the modelling assumptions made and the theoretical basis needed to develop the mathematical models presented. It describes the balance laws in fluid mechanics and the non-Newtonian inelastic modelling of the generalized Newtonian fluids. In particular, it presents the shear rate-based model (SRB) developed to solve the indeterminacy problem own by one of the most used inelastic rheological model present in literature (the BCCY model), with the aim to have a more physically-consistent model, and to derive reliable and quasi-analytical solutions for bio-ink flows. Next, it briefly describes the interaction phenomena occurring in multiphase flows made up of spherical particles dispersed in a Newtonian fluid. Then, the Chapter 3 presents the quasi-analytical framework developed in order to have a simple and ready-to-use solution considering the bio-ink as a homogeneous material. It evaluates with a good accuracy the main flow problem variables such as the extrusion velocity, the dispensing pressure, and the fluid shear stress applied on cells as a function of nozzle geometries and of rheological material proprieties of bio-ink. Specifically, it provides a quasi-analytical solution for inelastic fluids flowing in cylindrical and slightly tapered nozzles, with an application of the latter case to an experimental setup. Then, the Chapter 4 presents the numerical modelling of fluid-structure interaction implemented to accurately reproduce the fully 3D phenomena occurring at local scale between the polymeric fluid and cells. In particular, it is well known in literature the fluid shear stresses may cause cell damages by decreasing the cell vitality and affecting its proliferation capability [49, 52–56]. They may cause cell apoptosis by triggering reactive oxigen species [57, 58], mechanobiological transduction signals in cells and nucleus [59, 60] or direct deformation and rupture of cell membranes [61]. Therefore, through the developed FSI model, a high-fidelity and quantitative measure of the shear stresses has been performed, by statistically analysing the load history of a cell population, with densities typically used in application, immersed in GelMA and extruded through a nozzle with standard commercial sizes [49, 62]. In particular, the mean shear stress acting on the cell surface and the maximum shear stress have been analysed and compared with the classic estimate present in literature [49]. Finally, the thesis concludes with a remark on the developed models and obtained results and with the future steps.

# Chapter 2

# Theoretical framework

This chapter introduces the physical and mathematical background from which the research work to model the extrusion bioprinting process started. The Section 2.1 describes the modelling assumptions made to develop the approaches presented in the Chapter 3 and in the Chapter 4. Next, the Section 2.2 presents the conservation equations derived from the Reynolds transport theorem to describe the fluid dynamics of the bio-ink through the Eulerian approach. Then, the Section 2.3 describes possible choices on the constitutive models used in the literature to characterize the mechanics of bio-inks flow. In particular, it introduces the shear rate based (SRB) model developed to solve the indeterminacy problem of the BCCY model parameters [16], and to derive reliable and quasi-analytical solutions for bio-ink flows presented in the next Chapter 3. The Section 2.4 reports the Navier-Stokes equations governing bio-ink fluid dynamics. Finally, the Section 2.5 briefly recalls the dynamics of multi-phase flows describing the behaviour of particles flowing in a confined fluid.

## 2.1 Modelling assumptions

This section presents the assumptions made to model the two phases of the bio-ink: the fluid phase made up of the polymeric hydrogel, and the solid phase composed by the cells.

**Fluid phase.** The mathematical frameworks presented in this thesis to model the bio-ink flow dynamics are based on the hypothesis to consider its polymeric

fluid phase as a continuum medium. It assumes that the local control volume used to study the macroscopic physical quantities of the fluid (such as the velocity, viscosity etc.) is small enough to analyse the local value of the of the quantity of interest, and at the same time large enough to contain a large number of molecules so that the molecular fluctuations have no effect on the value of the measured physical quantity [63].

A useful dimensionless number which quantify the validity of the continuum hypothesis is the Knudsen number, defined as the ratio between the mean free path $\lambda$ of molecules constituting the fluid and the characteristic length $L$ of the problem

$$Kn = \frac{\lambda}{L} \, . \tag{2.1}$$

It is also used as reference to verify the no-slip boundary condition between the fluid and a wall. Commonly, when $Kn < 10^{-4}$ the continuum hypothesis and the no-slip boundary conditions are assured [64].

In extrusion bioprinting based on hydrogel bio-inks, the main component of the fluid phase is water [43, 65–67], which has a mean free path about $\lambda \simeq 10^{-1}\, nm$ [64]; and the lowest needle diameter commonly used is $D \simeq 100\, \mu m$ [68]. Thus, the Knudsen number is of the order of $Kn = \lambda/D \simeq 10^{-6}$, thereby justifying the continuum assumption made in the following models.

**Solid phase.** Regarding the immersed cells within the hydrogel and constituting the solid phase of bio-ink they determine in general a multi-phase nature of the bio-ink flow. In particular, by considering a typical cell density employed in bio-printing of $10^6\, cells/ml$ and a mean cell radius $R_{cell} = 5\, \mu m$ (see Section 1.3), the corresponding volume fraction of the solid phase results equal to $0.0523\% \ll 1\%$, thus indicating a disperse flow [69]. In this kind of flows, depending on the ratio $t_{cell}/t_F$ between the time $t_{cell}$ required for the cell to reach its steady velocity $V_{cell}$ within the nozzle, and the characteristic flow time $t_F = L/V_0$ with $L \simeq 10\, mm$ the nozzle length and $V_0 = 20\, mm/s$ the extrusion velocity, two main flow regimes can develop. The first is the *quasi-static regime*, characterized by a $t_{cell}/t_F \ll 1$ and a negligible influence of the dispersed phase (the cells) on the continuum phase (the hydrogel). In this case the relative motion between the two phases can be neglected. The second one is the *transient regime* characterized by a $t_{cell}/t_F \gg 1$ wherein the relative motion has to be taken into account since it affects the flow dynamics [69]. In practice it is not possible to evaluate a priori the $t_{cell}$ and $V_{cell}$ values. Alternatively, the flow regime can be qualitatively predicted by the size parameter

$$X = \frac{R_{cell}}{L} \left| 1 - \frac{\rho_{cell}}{\rho} \right| \, , \tag{2.2}$$

and the density parameter

$$Y = \frac{\left| 1 - \frac{\rho_{cell}}{\rho} \right|}{1 + 2\frac{\rho_{cell}}{\rho}} \, , \tag{2.3}$$

with $\rho$ the density of the fluid phase and $\rho_{cell}$ the density of the cellular solid phase. When $X/Y^2 \ll 1$ the flow presents a quasi-static regime [69] and the bio-ink can be modelled as a homogeneous fluid. Conversely when $X/Y^2 \gtrsim 1$ the flow has a transient regime and it has to be considered as a heterogeneous flow.

Considering the reference values above, and a $\rho_{cell} = 1.1\,\rho$ (the hydrogel is a water-based fluid)[70–72], the ratio between the size and density parameters turns out $X/Y^2 = 5.12 \cdot 10^{-2}$, indicating in this case the possibility to model the bio-ink as a homogeneous fluid. This hypothesis has been assumed to develop the quasi-analytical approach presented in the Chapter 3. Whereas, by considering larger cells, for example with a $R_{cell} = 15\,\mu m$, the previous ration results $X/Y^2 = 0.154$ starting to undermine the homogeneous fluid assumption and suggesting to treat the bio-ink as a heterogeneous flow. This case has been treated in the Chapter 4 wherein the cells have been modelled as deformable spheres immersed in a hydrogel.

## 2.2 Balance laws in fluid mechanics

**Reynolds transport theorem.** The fluid motion is governed by conservation equations of physical quantities transported by the fluid which describe its evolution in time and space.

Considering the fluid as a continuum media, it is possible to consider the set of points constituting the volume occupied by the fluid as fluid elements, namely that each point corresponds to a large quantity of fluid molecules. With this assumption is possible to consider the variables associated to the physical quantities of interest as continuous and differentiable functions.

Focusing on a control volume $V$ of a space region of the moving fluid, it is possible to analyse the variation of the extensive property $\Psi$ of the fluid associated to own specific field per mass unit $\psi$, namely

$$\Psi = \int_V \psi \rho dV \ , \tag{2.4}$$

where $\rho$ is the mass density of fluid. The time variation of $\Psi$ occurring within of the control volume $V$ can be evaluated through the Reynolds transport theorem [63]

$$\frac{d\Psi}{dt} = \frac{d}{dt}\int_V \rho\psi dV = \int_V \Big[\frac{\partial\,(\rho\psi)}{\partial t} + \nabla\cdot(\rho\psi\boldsymbol{v})\Big]dV \ , \tag{2.5}$$

where $\boldsymbol{v}$ is the fluid velocity field.

**Mass conservation.** Applying the Eq. (2.5) to the fluid mass $m$, the conjugated specific field turns out to be the unity $\psi = 1$, and the mass conservation equation holds

$$\frac{dm}{dt} = \frac{d}{dt}\int_V \rho dV = \int_V \Big[\frac{\partial\rho}{\partial t} + \nabla\cdot(\rho\boldsymbol{v})\Big]dV = 0 \ . \tag{2.6}$$

An useful form of the previous equation is the differentiable form which can be obtained considering the arbitrariness of the choice of the control volume $V$ and applying the localization lemma, obtaining the equation

$$\frac{\partial \rho}{\partial t} + \nabla \cdot (\rho \boldsymbol{v}) = 0 \ , \tag{2.7}$$

also known as *continuity equation*.

In case of incompressible fluids with constant density $\rho$ the previous equation simplifies in

$$\nabla \cdot \boldsymbol{v} = 0 \ , \tag{2.8}$$

indicating in this case a solenoidal velocity field.

**Momentum conservation.** Considering the Newton's second law applied to control volume $V$, we obtain the momentum conservation equation. In this case, the conjugated specific field of the momentum $\mathbf{Q}$ is the velocity $\psi = \boldsymbol{v}$. This equation states that the momentum variation of the fluid element is equal to the sum of the resultants of volume forces $\mathbf{F}_v$ and of surface forces $\mathbf{F}_s$ applied to the volume $V$

$$\frac{d\mathbf{Q}}{dt} = \frac{d}{dt}\int_V \rho \boldsymbol{v} \ dV = \int_V \rho \mathbf{f}_v dV + \int_S \boldsymbol{\sigma}\mathbf{n} dS = \mathbf{F}_v + \mathbf{F}_s \ , \tag{2.9}$$

where $\mathbf{f}_v$ is the volume force per mass unit, $S$ is the boundary of $V$, namely $S \equiv \partial V$, and $\boldsymbol{\sigma}$ is the Cauchy stress tensor associated to the surface element $dS$ with normal $\mathbf{n}$.

By applying the Reynolds transport theorem and the divergence theorem to the surface integral term in Eq. (2.5), the momentum conservation equation holds

$$\int_V \Big[\frac{\partial \rho \boldsymbol{v}}{\partial t} + \nabla \cdot (\rho \boldsymbol{v}\boldsymbol{v})\Big] dV = \int_V \big[\rho \mathbf{f}_v + \nabla \cdot \boldsymbol{\sigma}\big] \ dV \ . \tag{2.10}$$

Analogously to the previous case of mass conservation, by using the localization lemma the differentiable form of the momentum conservation results

$$\frac{\partial \rho \boldsymbol{v}}{\partial t} + \nabla \cdot (\rho \boldsymbol{v}\boldsymbol{v}) = \rho \mathbf{f}_v + \nabla \cdot \boldsymbol{\sigma} \ . \tag{2.11}$$

A simpler form of the previous equation can be obtained by using the mass conservation in Eq. (2.7) obtaining

$$\rho \frac{\partial \boldsymbol{v}}{\partial t} + \rho(\boldsymbol{v} \cdot \nabla)\boldsymbol{v} = \rho \mathbf{f}_v + \nabla \cdot \boldsymbol{\sigma} \ . \tag{2.12}$$

The stress tensor $\boldsymbol{\sigma}$ results symmetric for the balance of the angular momentum and in fluid dynamics it is usually decomposed in two terms

$$\boldsymbol{\sigma} = -p\mathbf{I} + \boldsymbol{\tau}. \tag{2.13}$$

The first term $-p\mathbf{I}$ is the hydrostatic part related to the internal pressure of the fluid element $p$, it is evaluated through the first invariant $I_1$ of the Cauchy stress tensor

$$p = -\frac{I_1}{3} = -\frac{\sigma_x + \sigma_y + \sigma_z}{3} \ , \tag{2.14}$$

and it quantifies the space average of normal stress distribution acting on the fluid particle [63]. The second term $\boldsymbol{\tau}$ is the deviatoric part related to the velocity field of the fluid element and to the tangential stresses acting on it.

Thus, by using the stress tensor decomposition in Eq. (2.13) and by neglecting the volume force contributes, the momentum conservation Eq. (2.9) turns out into

$$\rho\frac{\partial \boldsymbol{v}}{\partial t} + \rho(\boldsymbol{v}\cdot\nabla)\boldsymbol{v} = -\nabla p + \nabla\cdot\boldsymbol{\tau}\ . \tag{2.15}$$

## 2.3 Constitutive models

To solve the momentum balance Eq. (2.15) a constitutive relationship between the stress tensor $\boldsymbol{\sigma}$, in particular its deviatoric part $\boldsymbol{\tau}$, and the velocity field $\boldsymbol{v}$ is needed. In fluid dynamics, the constitutive laws are also referred as rheological models, and a first general classification is between viscous inelastic and viscoelastic fluids. The former after the load removal do not show a deformation or a memory effect and remain still. Frequent inelastic effects present in bio-inks are the shear thinning (pseudoplastic fluid), shear thickening (dilatant fluid) and yield stress (Bingham fluid) for example [73]. While the latter present memory effects with a time dependent behaviour, and after the load removal show a deformation for a specific relaxation time. In this work the bio-ink will be approximated as a viscous inelastic fluid.

**Generalized Newtonian fluids.** The reference inelastic models are the generalized Newtonian fluids which are an extension of Newtonian fluids [74]. Assuming a homogeneous and isotropic fluid, these models present a constitutive relationship for the deviatoric stress tensor

$$\boldsymbol{\tau} = 2\mu(\dot{\gamma})\mathbf{E} - \frac{2}{3}\mu(\dot{\gamma})\,(\nabla\cdot\boldsymbol{v})\,\mathbf{I}\ , \tag{2.16}$$

where $\mathbf{I}$ is the identity matrix, $\mathbf{E}$ is the strain rate tensor defined as the symmetric part of the velocity gradient

$$\mathbf{E} = Sym(\nabla\boldsymbol{v}) = \frac{\nabla\boldsymbol{v} + (\nabla\boldsymbol{v})^T}{2}\ . \tag{2.17}$$

$\mu(\dot{\gamma})$ is the fluid viscosity which is non-constant in general and it is in function of the strain rate tensor magnitude $\dot{\gamma}$ defined as

$$\dot{\gamma} = \sqrt{\frac{1}{2}\left|\left|2\mathbf{E}\right|\right|^2} = \sqrt{2\,\mathrm{Tr}(\mathbf{E}\mathbf{E}^T)} = \sqrt{2J_2}\ , \tag{2.18}$$

where $J_2$ is the main second invariant of the strain rate tensor. In a classic Couette flow in $x$ direction with a velocity vector $\boldsymbol{v} = [v_x\ 0\ 0]^T$ and $v_x = \alpha y$, with $\alpha$ a constant, the Eq. (2.18) reduces to the basic definition of shear rate $\dot{\gamma} = |\partial v_x/\partial y| = |\alpha|$.

By assuming a fluid with constant density and using the Eq. (2.8), the constitutive relationship Eq. (2.16) for Generalized Newtonian fluids simplifies into

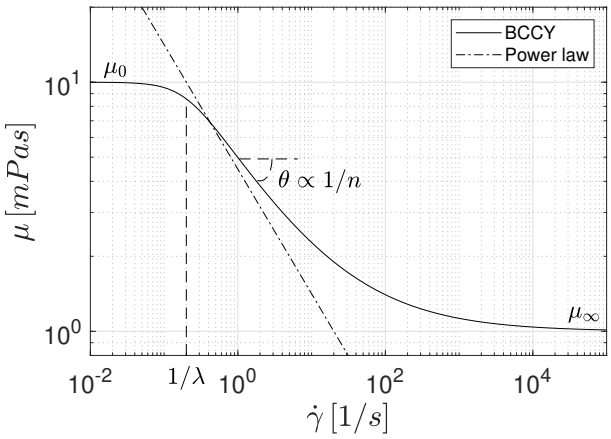


**Figure 2.1:** Rheological model examples. BCCY model: $\mu_0 = 10\ mPas$, $\mu_\infty = 1\ mPas$, $\lambda = 5\ s$, $n = 0.5$, $a = 2$; Power law model: $K = \mu_0 \lambda^{n-1} = 4.47\ mPas^{0.5}$, $n = 0.5$.

$$\boldsymbol{\tau} = 2\mu(\dot{\gamma})\mathbf{E}. \tag{2.19}$$

The modelling of inelastic effects for non-Newtonian fluids is obtained through the definition of specific rheological models correlating the strain rate tensor magnitude to the corresponding viscosity value $\mu = \mu(\dot{\gamma})$.

From the experimental viewpoint, the relationship between viscosity $\mu$ and shear rate $\dot{\gamma}$ for a viscous inelastic fluid can be obtained by means of rotational shear test through a rheometer. By using conversion factors, the viscosity and shear rate values can be derived from the measured torque and the applied rotational speed. Thus, imposing different rotational speeds, relationship between $\mu$ and $\dot{\gamma}$ is obtained from Eq. (2.19) as $\mu(\dot{\gamma}) = \tau(\dot{\gamma})/\dot{\gamma}$, where $\tau$ is the deviatoric stress tensor magnitude defined as $\tau = \sqrt{\frac{1}{2}\,||2\boldsymbol{\tau}||^2}$.

**Power law model.** The simplest inelastic rheological model is the two-parameters power law model [75, 76]

$$\mu = K\dot{\gamma}^{n-1}\ , \tag{2.20}$$

where $K$ is the consistency index (with units of $Pas^n$) and $n$ is the dimensionless power law exponent describing the slope of the viscosity curve as shown in Fig. 2.1. Depending on the value of $n$, the fluid shows a shear-thinning/pseudo-plastic behavior (for $0 < n < 1$), a classical Newtonian behaviour with constant viscosity (for $n = 1$), or a shear-thickening/dilatant response (for $n > 1$). Limitations of this model are the singularity at zero shear rate and to do not well describe the viscosity at high shear rates when compared with experimental data [16].

**Bird-Cross-Carreau-Yasuda model.** A more accurate relationship is the five-parameters Bird-Cross-Carreau-Yasuda model (BCCY) [16]

$$\mu = \mu_\infty + \frac{\mu_0 - \mu_\infty}{\left[1 + (\lambda\dot{\gamma})^a\right]^{\frac{1-n}{a}}} , \tag{2.21}$$

where $\mu_0$ and $\mu_\infty$ are the zero-shear rate and infinity-shear rate viscosity ($Pas$) respectively, $\lambda$ is the relaxation time constant ($s$), $a$ a dimensionless parameter and $n$ is the power law index. The BCCY model is usually known in literature simply as the Carreau-Yasuda model; but as analysed by Gallagher *et al.*[16] it was first reported in the reference textbook of Bird *et al.*[74] and thus it is a combination of the Cross, Carreau and Yasuda models.

As reported in Fig. 2.1, a fluid governed by a BCCY viscosity model behaves as a Newtonian fluid with a constant plateau viscosity $\mu_0$ at low shear rates ($\dot{\gamma} << 1/\lambda$), as a power law fluid at intermediate shear rates ($\dot{\gamma} > 1/\lambda$) with a $K \simeq \mu_0\lambda^{n-1}$ [74], and again as a Newtonian fluid but with viscosity $\mu_\infty$ for high shear rates; the parameters $n$ and $a$ regulate the transition between the power law region and the two viscosity plateau. Considering $a = 2$ and a null infinite-shear rate viscosity (i.e. $\mu_\infty = 0\ Pa\ s$) Eq. (2.21) turns into the simpler three-parameters Carreau equation [77]

$$\mu = \frac{\mu_0}{\left[1 + (\lambda\dot{\gamma})^2\right]^{\frac{1-n}{2}}} . \tag{2.22}$$

### 2.3.1 Shear rate based model

Despite the BCCY model is among the most effective ones in describing the shear thinning behaviour and it has been applied in a wide range of applications (such as blood flow modelling [78], plastic manufacturing [79], lubrificants production [80] and food processing [81]), it requires an ad hoc optimization procedure for the parameters calibration, since it suffers from an intrinsic problem of parameters identifiability as reported by Gallagher *et al.*[16]. In particular, to small variations of the cost function value of the model calibration procedure may correspond significant differences of tuned parameters and thus unreliable flow solutions [16].

Moreover, even considering simple geometries such as flat channel or a cylindrical pipe, the analytical solutions of the flow rate-pressure drop relationship and velocity profiles are possible only for the power law [73] and Ellis models [82], and not for BCCY-like models.

To overcome the indeterminacy problem of rheological parameters and to derive a reliable and an approximated analytical solution for cylindrical and slightly tapered nozzle flows, leading to the evaluation of the main flow problem variables (as presented in Sections 3.2 and 3.3), an alternative rheological model has been developed.

The model is based on an extension of the BBCY model in Eq. (2.21) which can be rewritten in its equivalent form

$$\mu\left(\dot{\gamma}\right) = \left(\mu_0 - \mu_\infty\right)\left\{\frac{1 + \left[\delta^{\frac{a}{1-n}} + \left(\frac{\dot{\gamma}}{\dot{\gamma}_\infty}\right)^a\right]^{\frac{(1-n)}{a}}}{\left[1 + \left(\frac{\dot{\gamma}}{\dot{\gamma}_0}\right)^a\right]^{\frac{(1-n)}{a}}}\right\}, \tag{2.23}$$

where $\delta = \mu_\infty/(\mu_0 - \mu_\infty)$, $\dot{\gamma}_0 = 1/\lambda$ and $\dot{\gamma}_\infty = \dot{\gamma}_0/(\delta^{\frac{1}{1-n}})$. With this form it is possible to estimate the corresponding shear rate value after which the second Newtonian plateau $\mu_\infty$ is approached. Even if this rewritten form of the BCCY model allows an estimation of the infinity-shear rate $\dot{\gamma}_\infty$ value, necessary for the flow solution presented in Section 3.2, it still presents the inferring problem of the model's parameters reported by Gallagher *et al.*[16] and the requirement of an ad hoc optimization procedure of parameter values.

Hence, in order to have a sound estimation of the $\dot{\gamma}_\infty$ value directly derived from the experimental data and to limit the indeterminacy problem of parameters, the main idea is to replace $\mu_\infty$ parameter of the BCCY model by inserting a second time constant $\lambda_\infty$ $(s)$

$$\mu\left(\dot{\gamma}\right) = \mu_0\left[\frac{1 + \left(\lambda_\infty\dot{\gamma}\right)^a}{1 + \left(\lambda_0\dot{\gamma}\right)^a}\right]^{\frac{(1-n)}{a}}. \tag{2.24}$$

In this way, as $\lambda_0$ determines the beginning of the power law region in the BCCY model ($\lambda_0 = \lambda$), $\lambda_\infty$ models the power law region's ending. In this manner, the two characteristic shear rate values $\dot{\gamma}_0 = 1/\lambda_0$ and $\dot{\gamma}_\infty = 1/\lambda_\infty$ are highlighted and the corresponding infinity-shear rate viscosity results $\mu_\infty = \mu_0\left(\dot{\gamma}_0/\dot{\gamma}_\infty\right)^{1-n}$. For this reason, the model in Eq. (2.24) is referred to as the Shear Rate-Based model (SRB) and besides allowing a direct evaluation of the $\dot{\gamma}_\infty$, it reduces the identifiability parameters' problem and allows to derive a reliable and quasi-analytical solution for bio-ink flows as shown in Section 3.4.

It is worth nothing that the SRB model can also describe two other possible rheological behaviours of shear-thinning fluids. The first sub-model, corresponding to the Yasuda model [83], applies to fluids with a viscosity characterized by an initial constant plateau at low shear rates followed by a shear-thinning branch at high shear rates. It is obtained from Eq. (2.24) with a $\lambda_\infty \to 0$ (corresponding to a $\dot{\gamma}_\infty \to \infty$ and a $\mu_\infty \to 0$)

$$\mu\left(\dot{\gamma}\right) = \frac{\mu_0}{\left[1 + \left(\lambda_0\dot{\gamma}\right)^a\right]^{\frac{(1-n)}{a}}}. \tag{2.25}$$

The second sub-model applies to fluids with a viscosity characterized by an initial shear-thinning branch and a final constant plateau. It is obtained from Eq. (2.24) by neglecting the first Newtonian behaviour at $\mu_0$ viscosity, namely by neglecting the $1/\left(\lambda_0\dot{\gamma}\right)^a$ contribute at the denominator, by obtaining a consistency index $K = \mu_0/\lambda_0^{1-n}$ $(Pa \cdot s^n)$

$$\mu\left(\dot{\gamma}\right) = \frac{K}{\dot{\gamma}^{1-n}}\left[1 + \left(\lambda_\infty\dot{\gamma}\right)^a\right]^{\frac{(1-n)}{a}}. \tag{2.26}$$

## 2.4 Navier-Stokes equations

The substitution of the Generalized Newtonian fluids definition in Eq. (2.16) into the momentum balance Eq. (2.15) leads to

$$\rho\frac{\partial \boldsymbol{v}}{\partial t} + \rho(\boldsymbol{v}\cdot\nabla)\boldsymbol{v} = -\nabla p + \nabla\cdot[2\mu(\dot{\gamma})\mathbf{E}] - \frac{2}{3}\nabla\cdot[\mu(\dot{\gamma})\,(\nabla\cdot\boldsymbol{v})\,\mathbf{I}] \ , \tag{2.27}$$

which are known as the Navier-Stoke equations, valid for non-Newtonian inelastic fluids, with non-constant viscosity. By considering incompressible fluids with a solenoidal velocity field $\nabla\cdot\boldsymbol{v} = 0$, such as the bio-inks used in bioprinting, the previous equation simplifies into

$$\rho\frac{\partial \boldsymbol{v}}{\partial t} + \rho(\boldsymbol{v}\cdot\nabla)\boldsymbol{v} = -\nabla p + \nabla\cdot[2\mu(\dot{\gamma})\mathbf{E}] \ . \tag{2.28}$$

By rewriting the viscosity law for a generic inelastic fluid as

$$\mu(\dot{\gamma}) = \mu_{ref} + \Delta\mu(\dot{\gamma}) \ , \tag{2.29}$$

where $\mu_{ref}$ is a reference viscosity constant, the Navier-Stokes equations turns into

$$\rho\frac{\partial \boldsymbol{v}}{\partial t} + \rho(\boldsymbol{v}\cdot\nabla)\boldsymbol{v} = -\nabla p + \mu_{ref}\nabla^2\boldsymbol{v} + \nabla\cdot[2\Delta\mu\mathbf{E}] \ . \tag{2.30}$$

For BCCY-type models a common choice (adopted in what follows) is $\mu_{ref} = \mu_\infty$.

### 2.4.1 Non-dimensional form

Usually, the Navier-Stokes equations are solved in non-dimensional form in order to have a better and more general understanding of the phenomena taking place as a function of non-dimensional numbers (e.g. the Reynolds number), both through analytical or numerical methods. They are obtained by scaling the problem variables by reference values which depend on the specific case. Considering a fluid flowing in a pipe such as for the extrusion bioprinting process, by choosing as reference values a diameter $D$ of the nozzle outlet, an extrusion velocity $V_0$, a pressure $p_0 = \rho V_0^2$ and an infinity-shear rate viscosity $\mu_\infty$ of the bio-ink, the corresponding non-dimensional form of Navier-Stokes Eqs. (2.30) together the mass conservation Eq. (2.8) result

$$\frac{\partial \boldsymbol{v}'}{\partial t'} + (\boldsymbol{v}'\cdot\nabla')\boldsymbol{v}' = -\nabla' p' + \frac{1}{Re_\infty}\nabla'^2\boldsymbol{v}' + \frac{1}{Re_\infty}\nabla'\cdot[2\Delta'\mu'\mathbf{E}'] \ , \tag{2.31}$$

$$\nabla'\cdot\boldsymbol{v}' = 0 \ , \tag{2.32}$$

where $\nabla' = \nabla/D$, $\boldsymbol{v}' = \boldsymbol{v}/V_0$, $t' = tV_0/D$, $p' = p/(\rho V_0^2)$, $\Delta\mu/\mu_\infty$, and $Re_\infty = \rho V_0 D/\mu_\infty$ is the Reynolds number referred to the infinity-shear rate viscosity $\mu_\infty$.

## 2.5 Extrusion bioprinting as particulate flows

As described in Section 2.1, depending on the size parameter $X$ and the density parameter $Y$ of the cells suspended within the bio-ink, the extrusion bioprinting can be modelled either as a homogeneous flow, or as a heterogeneous particulate flow [84, 85]. In general cells have a geometrical shape depending on their own phenotype [44], and thus specific to each printed tissue; but as first study, they can be modelled as spherical capsules [86–88]. The following paragraph briefly describes the interaction phenomena occurring in multi-phase flows made-up of suspended spherical particles flowing in a confined liquid channel studied to better understand the results presented in the Chapter 4.

**Radial equilibrium position.** Considering the case of neutrally buoyant particles flowing in a confined channel (both with a circular or rectangular section) in a low $Re$ number regime, such for the extrusion bioprinting process, if the flow is modelled as a Stokes flow without the convective-inertial terms, theoretically a particle will not cross fluid streamlines since the reversibility properties of the linear Stokes equation [89–91]. But because of presence oft small but not zero inertial terms of the Navier-Stokes equations, a spherical rigid particle flowing in a pipe experiences two kinds of lift force. A shear-induced inertial lift force, also known as tubular pinch, directed towards the nozzle wall and caused by the parabolic laminar Poiseuille flow; and a wall-induced inertial lift force towards the axis caused by the asymmetric waves around the particles near the wall. The balance of the two forces leads the particle to reach a radial equilibrium position away from the nozzle axis [92, 93]. Indeed, the first evidence of the particle radial migration has been reported by the experimental work of Segré and Silberberg [94] for a dilute suspension of neutrally buoyant particles with a particle diameter to nozzle diameter ratio ranging between $D_p/D = 0.07 - 0.1$, where they reported a radial equilibrium position $r_{eq} = 0.6D/2$. Next, Han *et al.*[95] demonstrated that the radial migration appears also for particle suspensions with a volume ratio value up to $\phi = 0.2$. Regarding the theoretical modelling, Saffman developed a solution with a lift force of the particle proportional to its slip velocity relative to the streamlines passing through its centre [90, 96]. Then, other experiments showed that particles lagging the fluid velocity have an equilibrium position shifted towards the axis, contrarily to particles leading the flow with an equilibrium position shifted towards the nozzle wall (see the references in [90]). In addition, Matas *et al.*[90] reported that for particle flows with particle diameter ranging between $D_p/D = 0.02 - 0.12$ , if the fluid velocity and thus the Reynolds number are increased, the radial equilibrium position moves closer to the wall than $0.6D/2$, and that heavier particles present the same equilibrium position. In all these cases, the radial equilibrium position is highly influenced by the particle relative size to the nozzle diameter $D_p/D$, and specifically from the particle Reynolds number defined as $Re_p = Re(D_p/D)^2$.

# Chapter 3

# Quasi-analytical modelling

This chapter presents the quasi-analytical models developed to analyse the bio-ink flow during the extrusion process. They assume the bio-ink as a disperse flow with a quasi-static regime with a negligible influence of the dispersed phase (the cells) on the continuum phase (the hydrogel), and therefore describing the bio-ink as a homogeneous fluid (see Section 2.1). The models presented are derived from the Stokes flow approximation valid at low Reynolds numbers, and describe the bio-ink's rheological behaviour through non-Newtonian inelastic constitutive models. The Section 3.1 introduces the piecewise model (PWM) approximation necessary to derive the quasi-analytical solutions for inelastic fluids flowing in cylindrical and slightly tapered nozzles presented respectively in Sections 3.2 and 3.3. Then, the Section 3.4 presents the obtained results, and the Section 3.5 reports the validation of the developed models.

## 3.1 Piecewise rheological approximation

The rheological SRB model in Eq. (2.24) can be approximated with a piecewise model (PWM) approximation

$$\mu\left(\dot{\gamma}\right) = \begin{cases} \mu_0 & \text{for } \dot{\gamma} \leq \dot{\gamma}_0, \tau \leq \tau_0 \\ K\dot{\gamma}^{n-1} & \text{for } \dot{\gamma}_0 < \dot{\gamma} \leq \dot{\gamma}_\infty, \tau_0 < \tau \leq \tau_\infty \\ \mu_\infty & \text{for } \dot{\gamma} > \dot{\gamma}_\infty, \tau > \tau_\infty \end{cases}, \tag{3.1}$$

where $K = \mu_0 \lambda_0^{n-1} = \mu_\infty \lambda_\infty^{n-1}$ $(Pa \cdot s^n)$ is the consistency index and $\mu_\infty = \mu_0 \left(\dot{\gamma}_0/\dot{\gamma}_\infty\right)^{1-n}$ $(Pa \cdot s)$ is the infinity-shear rate viscosity. From Eq. (3.1) shear

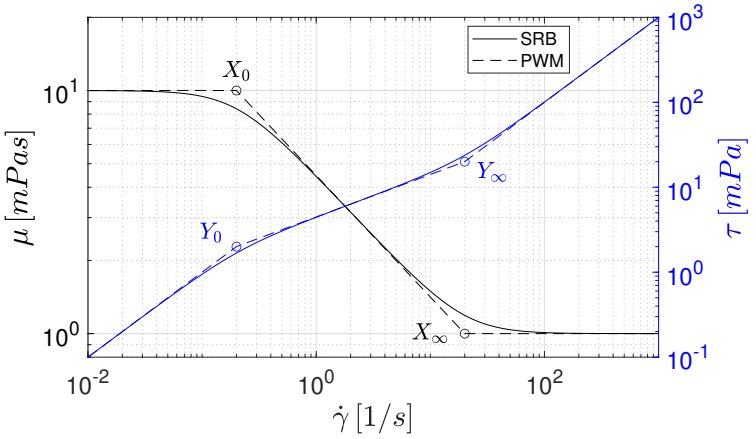


**Figure 3.1:** SRB model: $\mu_0 = 10\ mPas$, $\lambda_0 = 5\ s$, $\lambda_\infty = 0.05\ s$, $n = 0.5$, $a = 2$; PWM approximation: $\mu_0 = 10\ mPas$, $\dot{\gamma}_0 = 0.2\ s^{-1}$, $\dot{\gamma}_\infty = 20\ s^{-1}$, $n = 0.5$, $K = 4.47\ mPas^{0.5}$.

stresses read

$$\tau\left(\dot{\gamma}\right) = \begin{cases} \mu_0\dot{\gamma} & \text{for } \dot{\gamma} \leq \dot{\gamma}_0, \tau \leq \tau_0 \\ K\dot{\gamma}^n & \text{for } \dot{\gamma}_0 < \dot{\gamma} \leq \dot{\gamma}_\infty, \tau_0 < \tau \leq \tau_\infty \\ \mu_\infty\dot{\gamma} & \text{for } \dot{\gamma} > \dot{\gamma}_\infty, \tau > \tau_\infty \end{cases} , \tag{3.2}$$

where $\tau_0 = \mu_0\dot{\gamma}_0\ \ (Pa)$ and $\tau_\infty = \mu_\infty\dot{\gamma}_\infty\ \ (Pa)$ are denoted as the zero-shear rate stress and the infinity-shear stress respectively.

This approximation identifies three main viscosity regions depending on the working shear rates and shear-stress applied to the fluid: an initial constant Newtonian viscosity region characterized by $\mu_0$, an intermediate power-law viscosity region characterized by $K$ and $n$, and a final constant Newtonian viscosity region characterized by $\mu_\infty$. In the $(\mu,\ \dot{\gamma})$ graph, these three regions are represented by three lines intersecting at two points

$$X_0 = \left(\dot{\gamma}_0, \mu_0\right), \qquad X_\infty = \left(\dot{\gamma}_\infty, \mu_\infty\right) , \tag{3.3}$$

and in the $(\tau, \dot{\gamma})$ graph, at two points

$$Y_0 = \left(\dot{\gamma}_0, \tau_0\right), \qquad Y_\infty = \left(\dot{\gamma}_\infty, \tau_\infty\right) , \tag{3.4}$$

as shown in Fig. 3.1.

A similar approximation has been reported also by Müller *et al.*[97] for the shear stress analysis in cylindrical nozzles used in bioprinting.

Furthermore it is noteworthy that the viscosity function $\mu\left(\dot{\gamma}\right)$ can be interpreted as the transfer function between the stress $\tau$ of the fluid and the applied shear rate $\dot{\gamma}$. With the rheological model in Eq. (2.24) it is possible to highlight the characteristic values of the viscosity transfer function: $\mu_0$ assumes the meaning of a static gain and the shear rate values $\dot{\gamma}_0 = 1/\lambda_0\ \ \left(s^{-1}\right)$ and $\dot{\gamma}_\infty = 1/\lambda_\infty\ \ \left(s^{-1}\right)$ behave like a

pole and a zero respectively. It is noteworthy that, the PWM approximation in Eq. (3.1) can be seen as the Bode diagram for viscosity.

The PWM rheological form in Eqs. (3.1)-(3.2) will be used to derive semi-analytical solutions of fluid flow within cylindrical and slightly tapered nozzles, respectively in Sections 3.2 and 3.3.

## 3.2 Viscous-inelastic flows in cylindrical nozzles

By considering a bio-ink flow in a cylindrical nozzle with inner radius $R$ and length $L \gg R$ in a cylindrical coordinate system, and an axial symmetric stationary flow, the velocity solution is $\boldsymbol{v} = [0\ 0\ v_z(r)]^T$. Furthermore, the only non-zero component of the deviatoric stress tensor is $\tau_{zr}$, and the strain-rate tensor magnitude in Eq. (2.18) is equal to the absolute value of the shear rate component $\dot{\gamma} = |\dot{\gamma}_{zr}| = |2E_{zr}| = \left|\frac{\partial v_z}{\partial r}\right|$. Thus, through a force equilibrium in the axial component of a cylindrical control volume of length $L$ and radius $r$, the scalar relationship between $\tau_{zr}$ and $\dot{\gamma}_{zr}$ reads [98, 99]

$$\tau_{zr}(r) = -\frac{\Delta p}{2L} r = \mu(\dot{\gamma})\,\dot{\gamma}_{zr}(r) = \mu(\dot{\gamma})\,\frac{\partial v_z(r)}{\partial r}\ , \tag{3.5}$$

where $\Delta p$ is the pressure drop between the inlet and the outlet of the nozzle.

By inserting the above assumptions in the momentum balance Eq. (2.15) the left-hand side inertial terms are null (Stokes flow equation) and the pressure solution results

$$r) \qquad \frac{\partial p}{\partial r} = 0 \quad \longrightarrow \quad p = f_1(\theta, z) \tag{3.6a}$$

$$\theta) \qquad \frac{\partial p}{\partial \theta} = 0 \quad \longrightarrow \quad p = f_1(r, z) = f_1(\theta, z) = f_1(z) \tag{3.6b}$$

$$z) \qquad \frac{\partial p}{\partial z} = \frac{1}{r}\frac{\partial}{\partial r}\left(r\tau_{zr}(r)\right) = g_1(r) = \frac{\partial f_1(z)}{\partial z} = const = c_1 \tag{3.6c}$$

which implicates a linear variation of the pressure along the axis

$$p(z) = c_1 z + c_0 = -\frac{\Delta p}{L} z + p_{in} \tag{3.7}$$

where $p_{in}$ is the pressure value at the nozzle inlet.

From Eq. (3.5) and by using the PWM approximation in Eq. (3.2), it is possible to determine the two radius values $R_0$ and $R_\infty$ delimiting the three annular sections of the three viscosity regions (see Fig. 3.2(c))

$$R_0 = \frac{2L}{\Delta p}\tau_0\ , \qquad R_\infty = \frac{2L}{\Delta p}\tau_\infty\ . \tag{3.8}$$

Depending on the operating conditions of the extrusion process ($\Delta p$, flow rate $Q$), the needle geometry ($R$, $L$) and the rheological properties of the fluid ($\tau_0$, $\tau_\infty$), according to the PWM approximation three main flow conditions can develop as represented schematically in Fig. 3.2:

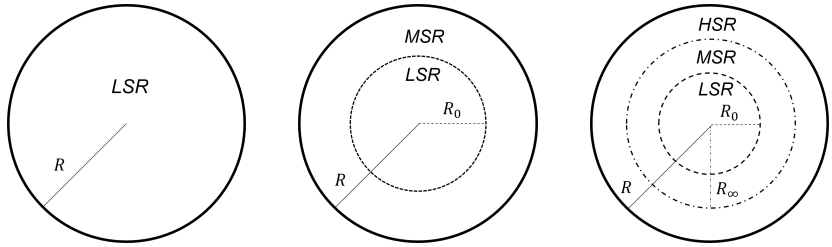


**Figure 3.2:** The three main flow conditions of PWM approximation: (a) Low-shear rate flow, (b) Medium-shear rate flow, (c) High-shear rate flow.

- a low-shear rate (LSR) flow characterized by Newtonian behaviour with a wall shear rate $|\dot{\gamma}_{wall}| \leq \dot{\gamma}_0$ and a wall shear-stress $|\tau_{wall}| = \Delta pR/(2L) \leq \tau_0$ (Fig. 3.2(a);

- a medium-shear rate (MSR) flow characterized by a mixed Newtonian/power-law behaviour with a $\dot{\gamma}_0 < |\dot{\gamma}_{wall}| \leq \dot{\gamma}_\infty$ and a $\tau_0 < |\tau_{wall}| \leq \tau_\infty$ (Fig. 3.2(b);

- and a high-shear rate (HSR) flow characterized by a mixed Newtonian/power-law/Newtonian behaviour with a $|\dot{\gamma}_{wall}| > \dot{\gamma}_\infty$ and a wall shear-stress $|\tau_{wall}| > \tau_\infty$ (Fig. 3.2(c).

For example, for a given geometry and fluid, by increasing the pressure drop $\Delta p$ the $R_0$ and $R_\infty$ values decrease and the flow gradually passes from the condition in Fig. 3.2a to the one in Fig. 3.2c.

By integrating Eq. (3.5) along the radius and imposing the symmetric flow boundary condition (i.e. $\partial v_z/\partial r|_{r=0} = 0$), the no-slip boundary condition at the wall (i.e. $v_z(R) = 0$) with the continuity condition between each viscosity zone (i.e., $v_{z,LSR}(R_0) = v_{z,MSR}(R_0)$ and $v_{z,MSR}(R_\infty) = v_{z,HSR}(R_\infty)$), the expressions of the velocity, shear rates and flow rates can be obtained, reading:

- Low-shear rate (LSR) flow, $|\dot{\gamma}_{wall}| \leq \dot{\gamma}_0,\ |\tau_{wall}| \leq \tau_0$

$$v_{z,LSR}(r) = \frac{\Delta pR^2}{4L\mu_0}\left[1 - \left(\frac{r}{R}\right)^2\right], \qquad \dot{\gamma}_{zr,LSR}(r) = -\frac{\Delta p}{2L\mu_0}r, \tag{3.9a}$$

$$Q = Q_{LSR} = \int_0^R 2\pi r v_{z,LSR} dr = \frac{\Delta p \pi R^4}{8L\mu_0}. \tag{3.9b}$$

- Medium-shear rate (MSR) flow, $\dot{\gamma}_0 < |\dot{\gamma}_{wall}| \leq \dot{\gamma}_\infty,\ \tau_0 < |\tau_{wall}| \leq \tau_\infty$

For $r \leq R_0$,

$$v_{z,LSR}(r) = A_0 - \frac{\Delta p}{4L\mu_0} r^2, \qquad \dot{\gamma}_{zr,LSR}(r) = -\frac{\Delta p}{2L\mu_0} r, \tag{3.10a}$$

$$Q_{LSR} = \int_0^{R_0} 2\pi r v_{z,LSR} dr = \pi R_0^2 A_0 - \frac{\Delta p \pi R_0^4}{8L\mu_0}, \tag{3.10b}$$

$$A_0 = \frac{1}{\alpha}\left(\frac{\Delta p}{2LK}\right)^{\frac{1}{n}} \left(R^\alpha - R_0^\alpha\right) \; + \; \frac{\Delta p R_0^2}{4L\mu_0}; \tag{3.10c}$$

for $r > R_0$,

$$v_{z,MSR}(r) = \left(\frac{\Delta p}{2LK}\right)^{\frac{1}{n}} \frac{R^\alpha - r^\alpha}{\alpha}, \qquad \dot{\gamma}_{zr,MSR}(r) = -\left(\frac{\Delta p}{2LK}\right)^{\frac{1}{n}} r^{1/n}, \tag{3.10d}$$

$$Q_{MSR} = \int_{R_0}^{R} 2\pi r v_{z,MSR} dr = \frac{2\pi}{\alpha}\left(\frac{\Delta p}{2LK}\right)^{\frac{1}{n}} \left[\frac{R^\alpha\left(R^2 - R_0^2\right)}{2} - \frac{R^\beta - R_0^\beta}{\beta}\right], \tag{3.10e}$$

$$Q = Q_{LSR} + Q_{MSR}. \tag{3.10f}$$

- High-shear rate (HSR) flow, $|\dot{\gamma}_{wall}| > \dot{\gamma}_\infty,\ |\tau_{wall}| > \tau_\infty$

  For $r \leq R_0$,

$$v_{z,LSR}(r) = A_0 - \frac{\Delta p}{4L\mu_0} r^2, \qquad \dot{\gamma}_{zr,LSR}(r) = -\frac{\Delta p}{2L\mu_0} r, \tag{3.11a}$$

$$Q_{LSR} = \int_0^{R_0} 2\pi r v_{z,LSR} dr = \pi R_0^2 A_0 - \frac{\Delta p \pi R_0^4}{8L\mu_0}, \tag{3.11b}$$

$$A_0 = \frac{1}{\alpha}\left(\frac{\Delta p}{2LK}\right)^{\frac{1}{n}} \left(R_\infty^\alpha - R_0^\alpha\right) + \frac{\Delta p}{4L}\left(\frac{R_0^2}{\mu_0} + \frac{R^2 - R_\infty^2}{\mu_\infty}\right); \tag{3.11c}$$

for $R_0 < r \leq R_\infty$,

$$v_{z,MSR}(r) = -\frac{1}{\alpha}\left(\frac{\Delta p}{2LK}\right)^{\frac{1}{n}} r^\alpha + A_1, \qquad \dot{\gamma}_{zr,MSR}(r) = -\left(\frac{\Delta p}{2LK}\right)^{\frac{1}{n}} r^{\frac{1}{n}}, \tag{3.11d}$$

$$Q_{MSR} = \int_{R_0}^{R_\infty} 2\pi r v_{z,MSR} dr = A_1 \pi\left(R_\infty^2 - R_0^2\right) - \frac{2\pi}{\alpha\beta}\left(\frac{\Delta p}{2LK}\right)^{\frac{1}{n}} \left(R_\infty^\beta - R_0^\beta\right), \tag{3.11e}$$

$$A_1 = \frac{\Delta p}{4L\mu_\infty}\left(R^2 - R_\infty^2\right) + \frac{1}{\alpha}\left(\frac{\Delta p}{2LK}\right)^{\frac{1}{n}} R_\infty^\alpha; \tag{3.11f}$$

for $r > R_\infty$,

$$v_{z,HSR}(r) = \frac{\Delta p}{4L\mu_\infty}\left(R^2 - r^2\right), \qquad \dot{\gamma}_{zr,HSR}(r) = -\frac{\Delta p}{2L\mu_\infty} r, \tag{3.11g}$$

$$Q_{HSR} = \int_{R_\infty}^{R} 2\pi r v_{z,HSR} dr = \frac{\Delta p \pi}{8L\mu_\infty}\left(R^2 - R_\infty^2\right)^2, \tag{3.11h}$$

$$Q = Q_{LSR} + Q_{MSR} + Q_{HSR}, \tag{3.11i}$$

where $\alpha = (n+1)/n$ and $\beta = (3n+1)/n$.

Regarding the SRB sub-models in Eqs. (2.25, 2.26) both cases can be described by the PWM approximation in Eq. (3.1). In particular, the flow expressions in Eqs. (3.9-3.10) also apply to the sub-model in Eq. (2.25), since it can been seen as the SRB model in Eq. (2.24) with a $\dot{\gamma}_\infty \to \infty$ and therefore with a $\tau_\infty \to \infty$ and a $R_\infty \to \infty$.

Whereas for the sub-model in Eq. (2.26), the analytical expressions of the velocity profiles, shear rate profiles and flow rates are similar to the Eqs. (3.10)-(3.11).

**Damage wall-shear stress value.** In the extrusion bioprinting process, it is desirable to limit the shear stress acting on cells and its maximum value occurring at the nozzle wall (the wall-shear stress, see Eq. (3.5)), since they may cause cell damages [49, 52–56]. The SRB model and PWM approximation allow to design a safety operating condition to limit the wall-shear stress during the extrusion. For example, by taking as reference the infinity-shear stress $\tau_\infty$ of the SRB model, considering a damage shear stress of the cell $\tau_{dam.} = \phi\tau_\infty$ with $\phi \gtrless 1$ corresponding to the the scalar ratio between $\tau_{dam.}$ and $\tau_\infty$, through the PWM approximation a safety operating condition could be to ensure a wall-shear stress lower than the damage shear stress of the cell, reading

$$\tau_{max} = \tau_{wall} = \frac{\Delta p}{2L} R \leq \tau_{dam.} = \phi\tau_\infty = \phi\mu_0\dot{\gamma}_0 \left(\frac{\dot{\gamma}_\infty}{\dot{\gamma}_0}\right)^n . \tag{3.12}$$

Eq. (3.12) establishes a relation between the operating conditions $\Delta p$ (or implicitly $Q$), the needle geometry $L$ and $R$, the rheological properties of the fluid $(\mu_0, \dot{\gamma}_0, n, \dot{\gamma}_\infty)$, and the damage shear stress of the cell $(\phi = \tau_{dam.}/\tau_\infty)$.

The corresponding damage extrusion velocity $\bar{V}_{dam.}$ can be computed from the flow rate Eqs. (3.9b), (3.10f), (3.11i) depending on the value of $\phi$, reading

$$\bar{V}_{dam.} = \frac{Q(\frac{\Delta p}{L}|_{dam.})}{\pi R^2}, \qquad \left.\frac{\Delta p}{L}\right|_{dam.} = \frac{2\phi\mu_0\dot{\gamma}_0}{R}\left(\frac{\dot{\gamma}_\infty}{\dot{\gamma}_0}\right)^n . \tag{3.13}$$

A parametric analysis of the damage extrusion velocity $\bar{V}_{dam.}$ has been carried out in Section 3.4.

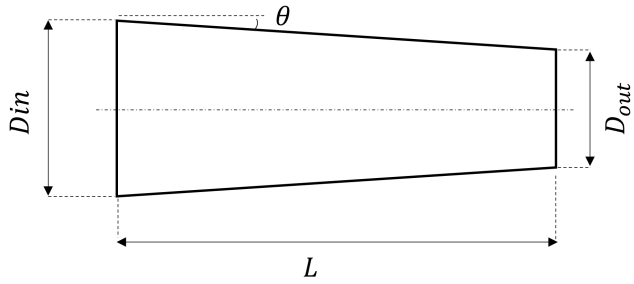


**Figure 3.3:** A tapered nozzle geometry.

## 3.3 Viscous-inelastic flows in slightly tapered nozzles

This section presents the solution of a flow in a slightly tapered nozzle. Initially a Newtonian fluid is addressed then, of a power law fluid is considered. Finally, the flow solution of a non-Newtonian inelastic fluid described by a PWM approximation in Eq. (3.1) is presented.

**Conical flow of a Newtonian fluid.** The first analysis regards the flow of a Newtonian fluid in a slightly tapered channel, for example within a cone with a linear reduction of the radius

$$R(z) = R_{in} - z\tan\theta \simeq R_{in} - \theta z, \tag{3.14}$$

with a length $L$, an inlet and outlet radii $R_{in}$ and $R_{out}$ respectively and a small opening angle $\theta \simeq (R_{in} - R_{out})/L$, as reported in Fig. 3.3. The following demonstration of the Newtonian case is based on that one reported in [74] and derived from the lubrification approximation [100]. The cross section reduction requires a not null flow in the radial direction and an acceleration along the axis. By using a cylindrical coordinate system and assuming an axial symmetric stationary flow, the velocity solution is $\boldsymbol{v} = [v_r(r,z)\ 0\ v_z(r,z)]^T$. The corresponding mass and momentum conservation Eqs. (2.8), (2.30) (considering $\mu_{ref} = \mu$ and $\Delta\mu = 0$) result

$$\frac{1}{r}\frac{\partial}{\partial r}(rv_r) + \frac{\partial v_z}{\partial z} = 0\ , \tag{3.15a}$$

$$r) \qquad \rho\left(v_r\frac{\partial v_r}{\partial r} + v_z\frac{\partial v_r}{\partial z}\right) = \mu\left[\frac{\partial}{\partial r}\left(\frac{1}{r}\frac{\partial}{\partial r}(rv_r)\right) + \frac{\partial^2 v_r}{\partial z^2}\right] - \frac{\partial p}{\partial r}\ , \tag{3.15b}$$

$$z) \qquad \rho\left(v_r\frac{\partial v_z}{\partial r} + v_z\frac{\partial v_z}{\partial z}\right) = \mu\left[\frac{1}{r}\frac{\partial}{\partial r}\left(r\frac{\partial v_z}{\partial r}\right) + \frac{\partial^2 v_z}{\partial z^2}\right] - \frac{\partial p}{\partial z}\ . \tag{3.15c}$$

By performing an order of magnitude analysis, the axial velocity and its axial derivative can be estimated as [74]

$$v_z \sim O\left(\frac{Q}{\pi R_{out}^2}\right) = O\left(V_z\right) \ , \tag{3.16a}$$

$$\frac{\partial v_z}{\partial z} \sim O\left(\frac{1}{L}\left(\frac{Q}{\pi R_{out}^2} - \frac{Q}{\pi R_{in}^2}\right)\right) = O\left(\frac{V_z}{L}\left(1-\chi^2\right)\right) \ , \tag{3.16b}$$

where $Q$ is the flow rate, $V_z$ is the reference axial velocity value, $R_{in}$ and $R_{out}$ the inlet and outlet radius and $\chi = R_{out}/R_{in}$. Then, from the mass conservation Eq. (3.15a) the estimate of the reference radial velocity $V_r$ turns out

$$O\left(V_r/R_{out}\right) + O\left(\frac{V_z}{L}\left(1-\chi^2\right)\right) = 0 \quad \longrightarrow \quad V_r = V_z\frac{R_{out}}{L}\left(1-\chi^2\right) \ . \tag{3.17}$$

Next, for the momentum balance equation, by neglecting the smaller terms such as the second viscous terms in the square brackets, the magnitude order analysis results

$$r) \qquad O\left(\frac{\rho V_z^2 R_{out}}{L^2}\left(1-\chi^2\right)\right) = O\left(\frac{\mu V_z}{R_{out}L}\left(1-\chi^2\right)\right) + O\left(\frac{\partial p}{\partial r}\right) \ , \tag{3.18a}$$

$$z) \qquad O\left(\frac{\rho V_z^2}{L}\left(1-\chi^2\right)\right) = O\left(\frac{\mu V_z}{R_{out}^2}\right) + O\left(\frac{\partial p}{\partial z}\right) \ . \tag{3.18b}$$

Thus, the comparison of the inertial to the viscous terms gives the following relationship

$$\frac{O\left(\text{inertial terms}\right)}{O\left(\text{viscous terms}\right)} = Re\frac{R_{out}}{L}\left(1-\chi^2\right) \ , \tag{3.19}$$

with the Reynolds number defined as $Re = \rho V_z R_{out}/\mu$.

In case of bioprinting flows, the previous equation indicates the inertial terms are negligible than the viscous ones, since the $Re$ numbers are almost always lower than 1 ($Re \ll 1$), due to the high viscosity values and small velocities and diameters. But it is worth nothing that even with non-negligible Reynold numbers, the geometrical factor $R_{out}(1-\chi^2)/L$ ensures the negligibility of the inertial terms. Furthermore, in case of a cylindrical nozzle ($\chi = 1$) it returns that the inertial terms are identically null as in Eqs. (3.6).

Next, the comparison of the pressure gradients terms turns out

$$\frac{O\left(\frac{\partial p}{\partial r}\right)}{O\left(\frac{\partial p}{\partial z}\right)} = \frac{R_{out}}{L}\left(1-\chi^2\right) \ , \tag{3.20}$$

showing that in case of a slightly tapered nozzle also the radial pressure gradient can be neglected.

Thus, by neglecting the smaller terms the momentum balance Eqs. (3.15b)-(3.15c) result

$$r) \qquad \frac{\partial p}{\partial r} \simeq 0 \quad \longrightarrow \quad p(r,z) \simeq p(z) \ , \tag{3.21a}$$

$$z) \qquad \frac{\partial p}{\partial z} \simeq \frac{dp}{dz} \simeq \mu \left[ \frac{1}{r} \frac{\partial}{\partial r} \left( r \frac{\partial v_z}{\partial r} \right) \right] \ , \tag{3.21b}$$

which are the equivalent form of the Eqs. (3.6) of the cylindrical case for a Newtonian fluid.

The integration of the Eq. (3.21b) in an arbitrary axial section of the nozzle with the application of the symmetric flow boundary condition (i.e. $\partial v_z/\partial r|_{r=0} = 0$) and the no-slip boundary condition at the wall (i.e. $v_z(r = R(z), z) = 0$) gives the flow rate equation

$$Q = -\frac{dp}{dz}(z) \frac{\pi R^4(z)}{8\mu}, \tag{3.22}$$

which is equivalent to the Hagen-Poiseuille law for cylindrical flows, but with the substantial difference of a non-constant radius. Therefore, also the pressure gradient varies along the axis in order to satisfy the flow conservation in each section. Thus, given a flow rate value, from the previous equation and by knowing the geometric function describing the cross section variation of the nozzle along the axis in Eq. (3.14), the pressure solution results

$$\begin{aligned} p(z) &= p_{in} - \frac{Q 8\mu}{\pi 3\theta} \left[ \frac{1}{(R_{in} - \theta z)^3} - \frac{1}{R_{in}^3} \right] \\ &= p_{in} - \frac{Q 8\mu}{\pi R_{in}^4} z \left[ 1 + \frac{2\theta z}{R_{in}} + \sum_{m=3}^{\infty} \binom{-3}{m} \frac{(-1)^m}{3} \left( \frac{\theta z}{R_{in}} \right)^{m-1} \right], \end{aligned} \tag{3.23}$$

where in the third member assuming a $|\theta z/R_{in}| < 1$ the Taylor expansion has been applied to highlight the conical contribution with respect to the cylindrical case (with a linear variation of the pressure), which vanishes for a null taper angle $\theta = 0°$.

Next, the velocity, shear rate, shear stress and flow rate solutions turn out

$$v_z(r,z) = -\frac{dp}{dz}(z)\frac{R^2(z)}{4\mu}\left[1-\left(\frac{r}{R(z)}\right)^2\right] = 2\bar{V}(z)\left[1-\left(\frac{r}{R(z)}\right)^2\right], \tag{3.24}$$

$$\dot{\gamma}_{zr}(r,z) \simeq \dot{\gamma}(r,z) = -\frac{4Qr}{\pi R^4(z)} = -\frac{4\bar{V}(z)r}{R^2(z)}, \tag{3.25}$$

$$\tau_{zr}(r,z) \simeq \tau(r,z) = -\frac{4Q\mu r}{\pi R^4(z)} = -\frac{4\bar{V}(z)\mu r}{R^2(z)}, \tag{3.26}$$

$$Q = -\frac{dp}{dz}(z)\frac{\pi R^4(z)}{8\mu} = \frac{\Delta p}{L}\frac{3\pi\left(R_{in}-R_{out}\right)}{8\mu\left(\frac{1}{R_{out}^3}-\frac{1}{R_{in}^3}\right)} = \frac{\Delta p}{L}\frac{\pi R_{in}^4}{8\mu}\left(1-\frac{1+\chi+\chi^2-3\chi^3}{1+\chi+\chi^2}\right), \tag{3.27}$$

where $\bar{V}(z)$ is the mean velocity in the specific axial section.

By summarizing, the conical flow for a Newtonian fluid can be described by the same governing equations of a flow in a cylindrical nozzle. In particular,the axial momentum balance Eq. (3.21c) is equivalent to Eq. (3.6), as long as the conditions in Eqs. (3.19), (3.20) are satisfied. In this case, the radial velocity component and gradient pressure variation can be neglected in relation to the homologous axial counterparts. The axial velocity assumes a parabolic profile linearly proportional to the mean velocity value in each section as in the cylindrical case, and the main difference is in the pressure solution with a non-constant axial pressure gradient along the nozzle axis.

**Conical flow of a power law fluid.** As for the previous case of a Newtonian fluid, by using a cylindrical coordinate system and assuming a stationary flow, the velocity solution sought is $\boldsymbol{v} = [v_r(r,z)\ 0\ v_z(r,z)]^T$. Given the same assumptions on the nozzle geometry with a slight taper angle $\theta$, the magnitude relations in Eqs. (3.16), (3.17) derived from the mass conservation equation are still valid. The corresponding strain rate tensor results

$$\mathbf{E} = \begin{bmatrix} E_{rr} & 0 & E_{zr} \\ & E_{\theta\theta} & 0 \\ \text{sym} & & E_{zz} \end{bmatrix} = \begin{bmatrix} \frac{\partial v_r}{\partial r} & 0 & \frac{1}{2}\left(\frac{\partial v_r}{\partial z}+\frac{\partial v_z}{\partial r}\right) \\ & \frac{v_r}{r} & 0 \\ \text{sym} & & \frac{\partial v_z}{\partial z} \end{bmatrix}, \tag{3.28}$$

with a magnitude order analysis equal to

$$O(\mathbf{E}) = \begin{bmatrix} O\left(\frac{V_z(1-\chi^2)}{L}\right) & 0 & O\left(\frac{V_z}{R_{out}}\right) \\ & O\left(\frac{V_z(1-\chi^2)}{L}\right) & 0 \\ \text{sym} & & O\left(\frac{V_z(1-\chi^2)}{L}\right) \end{bmatrix}. \tag{3.29}$$

By comparing each components, it is possible to note how the greatest term is $E_{zr} \simeq \partial v_z/\partial r$, which allows to approximate the strain rate tensor norm as in the cylindrical case in Eq. (2.18)

$$\dot{\gamma} \simeq \left| \frac{\partial v_z}{\partial r} \right| . \tag{3.30}$$

From the constitutive law, by assuming a non-Newtonian fluid described by the power law model in Eq. (2.20)

$$\mu(\dot{\gamma}) = K\dot{\gamma}^{n-1} , \tag{3.31}$$

the corresponding stress tensor turns out

$$\boldsymbol{\tau} = 2\mu(\dot{\gamma})\mathbf{E} = 2K\dot{\gamma}^{n-1}\mathbf{E} = \begin{bmatrix} \tau_{rr} & 0 & \tau_{zr} \\ & \tau_{\theta\theta} & 0 \\ \text{sym} & & \tau_{zz} \end{bmatrix} , \tag{3.32}$$

with a corresponding magnitude order analysis equal to

$$O(\boldsymbol{\tau}) = \begin{bmatrix} O(\zeta) & 0 & O\left(K\left(\dfrac{V_z}{R_{out}}\right)^n\right) \\ & O(\zeta) & 0 \\ \text{sym} & & O(\zeta) \end{bmatrix} , \tag{3.33}$$

where $\zeta = K\left(\dfrac{V_z}{R_{out}}\right)^n \dfrac{R_{out}(1-\chi^2)}{L}$.

It is worth nothing that how for a null taper angle (i.e. $\theta = 0°,\ \chi = 1$), the diagonal components of the strain rate and stress tensors vanish as in the case of a flow in a cylindrical nozzle.

Then, the momentum balance Eqs. (2.15) expressed in term of the stress tensor components result

$$r) \qquad \rho\left(v_r\frac{\partial v_r}{\partial r} + v_z\frac{\partial v_r}{\partial z}\right) = \left[\frac{1}{r}\frac{\partial}{\partial r}(r\tau_{rr}) + \frac{\partial \tau_{zr}}{\partial z} - \frac{\partial \tau_{\theta\theta}}{\partial r}\right] - \frac{\partial p}{\partial r} , \tag{3.34a}$$

$$z) \qquad \rho\left(v_r\frac{\partial v_z}{\partial r} + v_z\frac{\partial v_z}{\partial z}\right) = \left[\frac{1}{r}\frac{\partial}{\partial r}(r\tau_{zr}) + \frac{\partial \tau_{zz}}{\partial z}\right] - \frac{\partial p}{\partial z} , \tag{3.34b}$$

with a magnitude order analysis corresponding to

$$r) \qquad O\left(\frac{\rho V_z^2 R_{out}}{L^2}\left(1-\chi^2\right)\right) = O\left(K\left(\frac{V_z}{R_{out}}\right)^n \frac{\left(1-\chi^2\right)}{L}\right) + O\left(\frac{\partial p}{\partial r}\right) , \tag{3.35a}$$

$$z) \qquad O\left(\frac{\rho V_z^2}{L}\left(1-\chi^2\right)\right) = O\left(\frac{K}{R_{out}}\left(\frac{V_z}{R_{out}}\right)^n\right) + O\left(\frac{\partial p}{\partial z}\right) . \tag{3.35b}$$

The comparison of the inertial to the viscous terms gives the following relationship

$$\frac{O\left(\text{inertial terms}\right)}{O\left(\text{viscous terms}\right)} = Re_{(K,n)}\frac{R_{out}}{L}\left(1-\chi^2\right) \ , \tag{3.36}$$

where $Re_{(K,n)}$ is the Reynolds number specified for a power law fluid as reported in [101]

$$Re_{(K,n)} = \frac{\rho V_z^{2-n} R_{out}^n}{K}. \tag{3.37}$$

While the comparison of the pressure gradients terms gives the same previous relation in Eq. (3.20)

$$\frac{O\left(\dfrac{\partial p}{\partial r}\right)}{O\left(\dfrac{\partial p}{\partial z}\right)} = \frac{R_{out}}{L}\left(1-\chi^2\right) \ . \tag{3.38}$$

Thus, also for a power law fluid when the Reynolds numbers and the geometrical factor $R_{out}(1-\chi^2)/L$ are small, as in the in case of bioprinting flows, it is possible to neglect the inertial terms and the radial pressure gradient in the momentum balance equations, as in the previous paragraph for Newtonian flows in slightly tapered nozzles.

Therefore, the momentum balance Eqs. (3.34) turn out

$$r) \qquad \frac{\partial p}{\partial r} \simeq 0 \quad \longrightarrow \quad p(r,z) \simeq p(z) \ , \tag{3.39a}$$

$$z) \qquad \frac{\partial p}{\partial z} \simeq \frac{dp}{dz} \simeq \frac{1}{r}\frac{\partial\left(r\tau_{zr}\right)}{\partial r} \ . \tag{3.39b}$$

The integration of the Eq. (3.39b) in an arbitrary axial section of the nozzle with the application of the symmetric flow boundary condition (i.e. $\partial v_z/\partial r|_{r=0} = 0$) and the no-slip boundary condition at the wall (i.e. $v_z(r = R(z), z) = 0$) gives the flow rate equation

$$Q = \left(-\frac{dp}{dz}(z)\frac{1}{2K}\right)^{\frac{1}{n}}\frac{\pi R^{\beta}(z)}{\beta}, \tag{3.40}$$

where $\beta = (3n+1)/n$.

Given a flow rate value and by knowing the geometric function describing the cross section variation of the nozzle along the axis in Eq. (3.14), from the previous equation the pressure solution results

$$\begin{aligned} p(z) &= p_{in} - \left(\frac{Q\beta}{\pi}\right)^n \frac{2K}{3n\theta}\left[\frac{1}{(R_{in}-\theta z)^{3n}} - \frac{1}{R_{in}^{3n}}\right] \\ &= p_{in} - \left(\frac{Q\beta}{\pi}\right)^n \frac{2K}{R_{in}^{3n+1}} z\left[1 + \frac{(3n+1)\theta z}{2R_{in}} + \sum_{m=3}^{\infty}\binom{-3n}{m}\frac{(-1)^m}{3n}\left(\frac{\theta z}{R_{in}}\right)^{m-1}\right], \end{aligned} \tag{3.41}$$

where in the third member assuming a $|\theta z/R_{in}| < 1$ the Taylor expansion has been applied to highlight the conical contribution with respect to the cylindrical case (with a linear variation of the pressure), which vanishes for a null taper angle $\theta = 0°$.

Then, the velocity, shear rate, shear stress and flow rate solutions turn out

$$v_z(r,z) = \left(-\frac{dp}{dz}(z)\frac{1}{2K}\right)^{\frac{1}{n}} \frac{R(z)^\alpha}{\alpha}\left[1-\left(\frac{r}{R(z)}\right)^\alpha\right] = \frac{\beta}{\alpha}\bar{V}(z)\left[1-\left(\frac{r}{R(z)}\right)^\alpha\right], \tag{3.42}$$

$$\dot{\gamma}_{zr}(r,z) \simeq \dot{\gamma}(r,z) = -\frac{\beta Q}{\pi}\left(\frac{r}{R^{3n+1}(z)}\right)^{\frac{1}{n}} = -\beta\bar{V}(z)\left(\frac{r}{R^{n+1}(z)}\right)^{\frac{1}{n}}, \tag{3.43}$$

$$\tau_{zr}(r,z) \simeq \tau(r,z) = -\left(\frac{\beta Q}{\pi}\right)^n \frac{Kr}{R^{3n+1}(z)} = -\left(\beta\bar{V}(z)\right)^n \frac{Kr}{R^{n+1}(z)}, \tag{3.44}$$

$$\begin{aligned} Q &= \left(-\frac{dp}{dz}(z)\frac{1}{2K}\right)^{\frac{1}{n}} \frac{\pi}{\beta}R^\beta(z) = \left(\frac{\Delta p\, 3n}{2LK}\right)^{\frac{1}{n}} \frac{\pi}{\beta}\left(\frac{R_{in}-R_{out}}{\frac{1}{R_{out}^{3n}}-\frac{1}{R_{in}^{3n}}}\right)^{\frac{1}{n}} \\ &= \left(\frac{\Delta p}{2LK}\right)^{\frac{1}{n}} \frac{\pi R_{in}^\beta}{\beta}\left(1-\frac{1-\chi^{3n}-3n(1-\chi)\chi^{3n}}{1-\chi^{3n}}\right), \end{aligned} \tag{3.45}$$

where $\alpha = (n+1)/n$, $\beta = (3n+1)/n$ and $\bar{V}(z)$ is the mean velocity in the specific axial section. It is interesting to note how the shear rate expression in Eq. (3.43) evaluated at the nozzle wall (i.e. for $r = R(z)$) recurs in the simplest case of the wall shear rate for a cylindrical nozzle as reported in [102].

**Conical flow of an inelastic fluid: general relationships.** By taking into account a Generalized Newtonian inelastic fluid flowing in a slightly tapered nozzle and with a shear-thinning viscosity described by a rheological law $\mu = \mu(\dot{\gamma})$, its constitutive relationship can be approximated through the SRB model in Eq. (2.24), and in particular through the PWM approximation in Eq. (3.1), which is a combination of a Newtonian and a power law model.

Thus, the flow analyses in the previous paragraphs, considering the same geometric assumptions, are still valid. In particular, from the integration of the axial momentum balance Eq. (3.39b) here reported

$$\frac{dp}{dz} = \frac{1}{r}\frac{\partial\left(r\tau_{zr}\right)}{\partial r} = \frac{1}{r}\frac{\partial}{\partial r}\left(r\mu\frac{\partial v_z}{\partial r}\right) \tag{3.46}$$

the shear stress distribution turns out

$$\tau_{zr}(r,z) = \frac{dp}{dz}(z)\frac{r}{2}\,, \tag{3.47}$$

which is equivalent to the cylindrical flow case, with the substantial difference of a non-constant axial pressure gradient along the nozzle axis. Integrating the Eq.

(3.46) along the radius $R(z)$ of a generic cross section and applying the symmetric flow boundary condition (i.e. $\partial v_z/\partial r|_{r=0} = 0$) and the no-slip boundary condition at the wall (i.e. $v_z(r = R(z), z) = 0$) the general velocity solution results

$$v_z(r,z) = -\frac{dp}{dz}\left[\int_0^{R(z)} \frac{\psi d\psi}{2\mu[\dot{\gamma}(\psi)]} - \int_0^{r} \frac{\psi d\psi}{2\mu[\dot{\gamma}(\psi)]}\right] , \tag{3.48}$$

with a flow rate corresponding to

$$Q = \int_0^{R(z)} v_z 2\pi r dr = -\frac{dp}{dz}\pi \int_0^{R(z)} \left[\int_0^{R(z)} \frac{\psi d\psi}{2\mu[\dot{\gamma}(\psi)]} - \int_0^{r} \frac{\psi d\psi}{2\mu[\dot{\gamma}(\psi)]}\right] r dr , \tag{3.49}$$

wherein the dependence of the viscosity on the shear rate $\mu = \mu(\dot{\gamma})$ has been highlighted.

It is interesting nothing that the previous Eq. (3.48) for Generalized Newtonian fluids is analogous to the scalar Generalized Ohm's law

$$j = \sigma E , \tag{3.50}$$

where $j$ is the current density, $\sigma$ the electric conductivity and $E$ the electric field. In particular proceeding by comparison between the two physical systems, the axial pressure gradient $F = -dp/dz$ and the pressure drop $\Delta p$ correspond to $E$ and the voltage $\Delta V$ respectively

$$\Delta p = \int_0^L F dz = \int_0^L -\frac{dp}{dz} dz \quad \leftrightarrow \quad |\Delta V| = \int_0^L E dx = \int_0^L -\frac{dV}{dx} dx , \tag{3.51}$$

and the velocity corresponds to the current density

$$v_z = \sigma_{hyd} F = \sigma_{hyd}\left(-\frac{dp}{dz}\right) \quad \leftrightarrow \quad j = \sigma E \tag{3.52}$$

where $\sigma_{hyd}$ is the hydraulic conductivity

$$\sigma_{hyd} = \int_0^{R(z)} \frac{\psi d\psi}{2\mu[\dot{\gamma}(\psi)]} - \int_0^{r} \frac{\psi d\psi}{2\mu[\dot{\gamma}(\psi)]} , \tag{3.53}$$

which depends on the fluid viscosity, the nozzle geometry and also on the operating conditions, such as the flow rate, since it is in function on the shear rate.

Furthermore, by integrating the Eq. (3.47) the axial pressure gradient turns out

$$\frac{dp}{dz}(z) = \frac{4}{R^2(z)} \int_0^{R(z)} \tau_{zr}(r,z) dr , \tag{3.54}$$

which shows how the axial pressure gradient value in each section of the nozzle is determined by the distribution of the shear stress along the section.

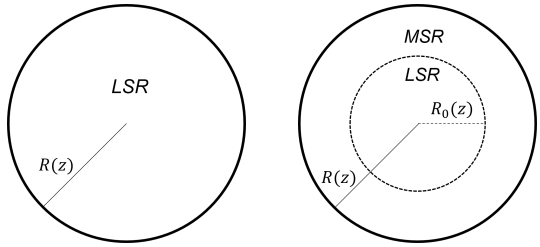


**Figure 3.4:** The two main flow conditions of PWM approximation in Eqs. (3.57) and (3.58) for a Carreau fluid flowing within a conical nozzle: (a) Low-shear rate flow, (b) Medium-shear rate flow.

**Conical flow of a Carreau fluid.** Considering an inelastic fluid flowing in a slightly tapered nozzle, for example within a cone with a linear reduction of the radius as in Eq. (3.14)

$$R(z) = R_{in} - z\tan\theta \simeq R_{in} - \theta z, \tag{3.55}$$

and fitted by by the SRB model with a null $\lambda_\infty = 0\,s$ and an $a = 2$, namely described by the Carreau model [77] in Eq. (2.22)

$$\mu\left(\dot{\gamma}\right) = \frac{\mu_0}{\left[1 + \left(\lambda_0\dot{\gamma}\right)^2\right]^{\frac{(1-n)}{2}}}\ , \tag{3.56}$$

in order to find a semi-analytical solution of the flow problem based on the conical flow solutions of the previous paragraphs and on the cylindrical flow solutions with low-shear rates of Eqs. (3.9a), (3.9b), and medium-shear rates of Eqs. (3.10a)-(3.10f), it is possible to approximate its constitutive relationship through the PWM approximation in Eqs. (3.1)-(3.2)

$$\mu\left(\dot{\gamma}\right) = \begin{cases} \mu_0 & \text{for } \dot{\gamma} \le \dot{\gamma}_0, \tau \le \tau_0 \\ K\dot{\gamma}^{n-1} & \text{for } \dot{\gamma} > \dot{\gamma}_0, \tau > \tau_0 \end{cases}\ , \tag{3.57}$$

$$\tau\left(\dot{\gamma}\right) = \begin{cases} \mu_0\dot{\gamma} & \text{for } \dot{\gamma} \le \dot{\gamma}_0, \tau \le \tau_0 \\ K\dot{\gamma}^{n} & \text{for } \dot{\gamma} > \dot{\gamma}_0, \tau > \tau_0 \end{cases}\ . \tag{3.58}$$

As for the previous case of the cylindrical nozzle, from the Eq. (3.47) and by using the PWM approximation, it is possible to determine the radius value $R_0(z)$ delimiting the two annular sections of the two viscosity regions (see Fig. 3.4(b)) in each axial section

$$R_0(z) = \frac{2\tau_o}{\left|\frac{dp}{dz}(z)\right|}\ , \tag{3.59}$$

which compared to the cylindrical nozzle case, it is non-constant and it is a function of the axial coordinate $z$, since the axial pressure gradient is no longer constant and it increases along the conical nozzle axis.

Depending on the operating conditions of the extrusion process ($\Delta p$, flow rate $Q$), the needle geometry ($R_{in}$, $R_{out}$, $L$, $\theta$), the rheological properties of the fluid ($\tau_0$), and in addition to the cylindrical flow case also on the axial coordinate $z$, according to the PWM approximation two main flow conditions can develop as represented schematically in Fig. 3.4:

- a low-shear rate (LSR) flow characterized by a Newtonian behaviour with a $|\dot{\gamma}_{wall}(z)| \leq \dot{\gamma}_0$ and a $|\tau_{wall}(z)| = |dp/dz|\, R(z)/2 \leq \tau_0$ (Fig. 3.4(a));
- and a medium-shear rate (MSR) flow characterized by a mixed Newtonian/power-law behaviour with a $|\dot{\gamma}_{wall}(z)| > \dot{\gamma}_0$ and a $|\tau_{wall}(z)| > \tau_0$ (Fig. 3.4(b)).

By integrating the Eq. (3.46) along the radius $R(z)$ of a generic axial section of the nozzle $z$ and imposing the no-slip boundary condition at the wall (i.e. $v_z\,(R(z)) = 0$) with the continuity condition between the two viscosity zones (i.e., $v_{z,LSR}\,(R_0(z)) = v_{z,MSR}\,(R_0(z))$, the expressions of the velocity, shear-rates and flow rates read:

- Low-shear rate (LSR) flow, $|\dot{\gamma}_{wall}(z)| \leq \dot{\gamma}_0,\ |\tau_{wall}(z)| \leq \tau_0$

$$v_{z,LSR}\,(r,z) = -\frac{dp}{dz}(z)\frac{R^2(z)}{4\mu_0}\left[1-\left(\frac{r}{R(z)}\right)^2\right], \tag{3.60a}$$

$$\dot{\gamma}_{zr,LSR}\,(r,z) = \frac{dp}{dz}(z)\frac{r}{2\mu_0}, \tag{3.60b}$$

$$Q = Q_{LSR} = \int_0^{R(z)} r v_{z,LSR} dr = -\frac{dp}{dz}(z)\frac{\pi R^4(z)}{8\mu_0}. \tag{3.60c}$$

- Medium-shear rate (MSR) flow,$|\dot{\gamma}_{wall}(z)| > \dot{\gamma}_0,\ |\tau_{wall}(z)| > \tau_0$

  For $r \leq R_0(z)$,

$$v_{z,LSR}\,(r,z) = A_0(z) + \frac{dp}{dz}(z)\frac{r^2}{4\mu_0}, \qquad \dot{\gamma}_{zr,LSR}\,(r,z) = -\frac{dp}{dz}(z)\frac{r}{2\mu_0}, \tag{3.61a}$$

$$Q_{LSR}(z) = \int_0^{R_0(z)} r v_{z,LSR} dr = \pi R_0^2(z) A_0(z) + \frac{dp}{dz}(z)\frac{\pi R_0^4(z)}{8\mu_0}, \tag{3.61b}$$

$$A_0(z) = \frac{1}{\alpha}\left(-\frac{dp}{dz}(z)\frac{1}{2K}\right)^{\frac{1}{n}}\left(R^\alpha(z) - R_0^\alpha(z)\right) - \frac{dp}{dz}(z)\frac{R_0^2(z)}{4\mu_0}; \tag{3.61c}$$

for $r > R_0(z)$,

$$v_{z,MSR}(r,z) = \left(-\frac{dp}{dz}(z)\frac{1}{2K}\right)^{\frac{1}{n}} \frac{R^{\alpha}(z) - r^{\alpha}}{\alpha}, \tag{3.61d}$$

$$\dot{\gamma}_{zr,MSR}(r,z) = -\left(-\frac{dp}{dz}(z)\frac{1}{2K}\right)^{\frac{1}{n}} r^{1/n}, \tag{3.61e}$$

$$Q_{MSR}(z) = \int_{R_0(z)}^{R(z)} r v_{z,MSR} dr = \tag{3.61f}$$

$$\frac{2\pi}{\alpha}\left(-\frac{dp}{dz}(z)\frac{1}{2K}\right)^{\frac{1}{n}} \left[\frac{R^{\alpha}(z)\left(R^2(z) - R_0^2(z)\right)}{2} - \frac{R^{\beta}(z) - R_0^{\beta}(z)}{\beta}\right], \tag{3.61g}$$

$$Q = Q_{LSR}(z) + Q_{MSR}(z), \tag{3.61h}$$

where $\alpha = (n+1)/n$ and $\beta = (3n+1)/n$. Eqs.((3.60)-(3.61) are equivalent to the corresponding Eqs. (3.9-(3.10) for the cylindrical flow, with the difference to present a dependence from the axial coordinate $z$, since in this case the axial pressure gradient is not longer constant along the nozzle axis.

Furthermore, compared to the conical flow cases of a Newtonian and a power law fluid of the previous paragraphs, given a nozzle geometry and a flow rate $Q$, it is not possible to evaluate a priori the axial pressure gradient from Eqs. (3.22),(3.40). Thus, to compute the axial pressure gradient of a Carreau fluid approximated by the PWM approximation in Eqs. (3.57), (3.58) and flowing in a conical nozzle with a flow rate $Q$, and to evaluate the pressure drop applied to the nozzle, an iterative semi-analytical procedure is necessary.

**Iterative procedure.** Taking into account as example an inelastic fluid described through the PWM approximation in Eqs. (3.57), (3.58), given a flow rate $Q$, the flow regime (LSR or MSR) in each axial section $z$ of the nozzle is determined by the wall-shear rate $|\dot{\gamma}_{wall}(z)|$ and the wall-shear stress $|\tau_{wall}(z)|$ values whether they are smaller or larger than the values of the $Y_0 = (\dot{\gamma}_0, \tau_0)$ point (respectively).

Then, by considering the Eq. (3.54)

$$\frac{dp}{dz}(z) = \frac{4}{R^2(z)} \int_0^{R(z)} \tau_{zr}(r,z) dr \ , \tag{3.62}$$

and looking to the stress plot in Fig. 3.5 it is possible to write

$$\left|\frac{dp}{dz}(z)\right|_{\text{PWM}} \leq \left\{ \left|\frac{dp}{dz}(z)\right|_{\text{Newtonian}}, \left|\frac{dp}{dz}(z)\right|_{\text{power law}} \right\} \ , \tag{3.63}$$

since in each axial section whatever the operating wall-shear stress $\tau_{wall}(z) = \tau_{max}(z)$, the shear stress distribution $\tau_{zr}(r,z)$ along the cross section of the PWM approximation is lower or at most equal to the corresponding sub-cases of the Newtonian and power law fluid.

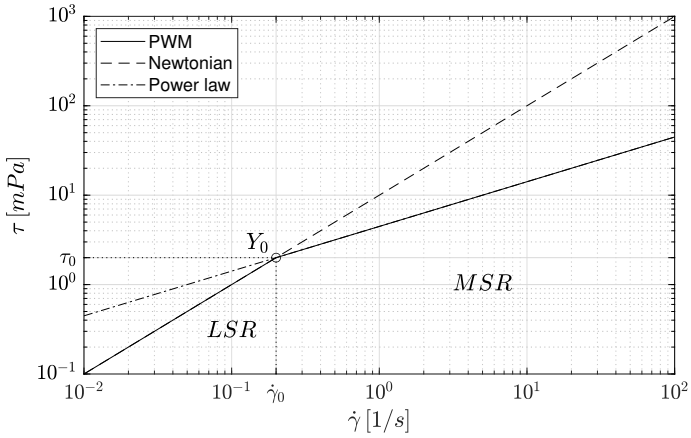


**Figure 3.5:** PWM approximation example: $\mu_0 = 10\ mPas$, $\dot{\gamma}_0 = 0.2\ s^{-1}$, $n = 0.5$, $K = 4.47\ mPas^{0.5}$. The corresponding sub-models: Newtonian model with $\mu = \mu_0$ and power law model with $K$ and $n$. $Y_0 = (\dot{\gamma}_0, \tau_0)$ delimiting the LSR and MSR regions ($\tau_0 = 2\ mPa$).

Thus, once evaluated the axial pressure gradients of the corresponding Newtonian and power law sub-cases of the PWM approximation from the Eqs. (3.22),(3.40)

$$\left.\frac{dp}{dz}(z)\right|_{\text{Newtonian}}, \qquad \left.\frac{dp}{dz}(z)\right|_{\text{power law}}, \tag{3.64}$$

a possible iterative procedure to compute the axial pressure gradient of the PWM approximation based on the conservation of the flow rate $Q$ in each axial section is reported in the Algorithm 1, wherein

$$\left|\frac{dp}{dz}(z)\right|_{\text{PWM},0} = min\left\{\left|\frac{dp}{dz}(z)\right|_{\text{Newtonian}}, \left|\frac{dp}{dz}(z)\right|_{\text{power law}}\right\} \tag{3.65}$$

is the first guess value of the iterative root-finding procedure

$$Q_{LSR}\left[\frac{dp}{dz}(z)\right] + Q_{MSR}\left[\frac{dp}{dz}(z)\right] - Q = 0\ . \tag{3.66}$$

**Algorithm 1:** Algorithm to compute the axial pressure gradient of the PWM approximation in Eqs. (3.57),(3.58).

The nozzle axis $z$ is divided in $n$ intervals such that $\Delta z = z_{i+1} - z_i$, with $i = 1, 2, ..., n+1$, $z_1 = z_{in}$ and $z_{n+1} = z_{out}$.

**At the inlet:** $z_i = z_1 = z_{in}$

$\left|\frac{dp}{dz}(z_{in})\right|_{\text{PWM}} = \left|\frac{dp}{dz}(z_{in})\right|_{\text{Newtonian}}$;

**if** $\left|\frac{dp}{dz}(z_{in})\right|_{PWM} > \frac{2\tau_0}{R_{in}}$ **then**

$\left|\frac{dp}{dz}(z_{in})\right|_{\text{PWM}} \quad : \quad Q_{LSR}(z_{in}) + Q_{MSR}(z_{in}) - Q = 0$

with $\left|\frac{dp}{dz}(z_{in})\right|_0 = min\left\{\left|\frac{dp}{dz}(z_{in})\right|_{\text{Newtonian}}, \left|\frac{dp}{dz}(z_{in})\right|_{\text{power law}}\right\}$

**end**

**Along the axis:** $z_{in} < z_i \leq z_{out}$

**if** $\left|\frac{dp}{dz}(z_{i-1})\right|_{PWM} > \frac{2\tau_0}{R(z_{i-1})}$ **then**

$\left|\frac{dp}{dz}(z_i)\right|_{\text{PWM}} \quad : \quad Q_{LSR}(z_i) + Q_{MSR}(z_i) - Q = 0$

with $\left|\frac{dp}{dz}(z_i)\right|_0 = min\left\{\left|\frac{dp}{dz}(z_i)\right|_{\text{Newtonian}}, \left|\frac{dp}{dz}(z_i)\right|_{\text{power law}}\right\}$

**else**

**if** $\left|\frac{dp}{dz}(z_{i-1})\right|_{PWM} \leq \frac{2\tau_0}{R(z_{i-1})}$ **then**

$\left|\frac{dp}{dz}(z_i)\right|_{\text{PWM}} = \left|\frac{dp}{dz}(z_i)\right|_{\text{Newtonian}}$

**if** $\left|\frac{dp}{dz}(z_i)\right|_{PWM} > \frac{2\tau_0}{R(z_i)}$ **then**

$\left|\frac{dp}{dz}(z_i)\right|_{\text{PWM}} \quad : \quad Q_{LSR}(z_i) + Q_{MSR}(z_i) - Q = 0$

with $\left|\frac{dp}{dz}(z_i)\right|_0 = min\left\{\left|\frac{dp}{dz}(z_i)\right|_{\text{Newtonian}}, \left|\frac{dp}{dz}(z_i)\right|_{\text{power law}}\right\}$

**end**

**end**

**end**

## 3.4 Results

### 3.4.1 Identifiability properties of the SRB model

**Direct extrapolation from experimental data.** To demonstrate the capability of the SRB model in Eq. (2.24) to reduce the identifiability problem of the BCCY model in Eq. (2.21), a calibration of viscosity data for a cell-laden hydrogel [103] has been performed by extrapolating values of model parameters directly from experimental data (fixing $a = 2$), and comparing the fitting capabilities of the SRB and BCCY models. Specifically, referring to data in Fig. 3.6 the direct

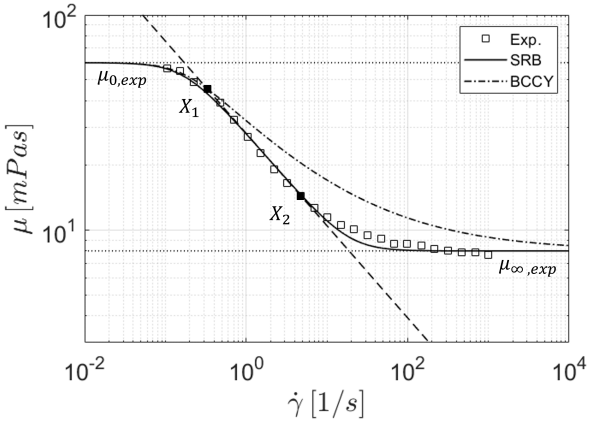


**Figure 3.6:** Fitting capability comparison between SRB and BCCY models, with first guess parameters derived experimentally. Experimental data are taken from Colosi *et al.*[103].

calibration procedure consists in the following steps:

1. read the limit values $\mu_{0,exp}$ and $\mu_{\infty,exp}$ as the values close to the first and last measuring points respectively (dotted lines in Fig. 3.6);
2. identify two suitable data points $X_1(\dot{\gamma}_1, \mu_1)$ and $X_2(\dot{\gamma}_2, \mu_2)$ for the start and the end of the power law region (in this case the 4th and the 11th has been chosen), and trace the power-law line between them (dashed line in Fig. 3.6);
3. derive $K_{exp}$ and $n_{exp}$ values from $X_1$ and $X_2$

$$K_{L,exp} = \frac{\mu_{L,1}\dot{\gamma}_{L,2} - \mu_{L,2}\dot{\gamma}_{L,1}}{\dot{\gamma}_{L,2} - \dot{\gamma}_{L,1}}, \qquad n_{exp} = 1 + \frac{\mu_{L,2} - \mu_{L,1}}{\dot{\gamma}_{L,2} - \dot{\gamma}_{L,1}}\ , \tag{3.67}$$

   where the footnote $f_L$ denotes $f_L = \log_{10} f$ (e.g. $\mu_{L,1} = \log_{10}\mu_1$);
4. derive $\dot{\gamma}_{0,exp}$ and $\dot{\gamma}_{\infty,exp}$ from the intersections of the two dotted lines with the dashed line, namely

$$\dot{\gamma}_{0,exp} = \left(\frac{\mu_{0,exp}}{K_{exp}}\right)^{1/(n_{exp}-1)}, \qquad \dot{\gamma}_{\infty,exp} = \left(\frac{\mu_{\infty,exp}}{K_{exp}}\right)^{1/(n_{exp}-1)}\ . \tag{3.68}$$

The derived parameters from the viscosity data are reported in Table 3.1. As reported in Fig. 3.6, the SRB model shows good fitting capability already with experimentally derived parameters. Whereas the BCCY model exhibits only a good fit near the first viscosity data, but then it does not catch data in the power-law and in the infinity-shear rate viscosity regions. Accordingly, the BCCY model intrinsically requires an ad hoc optimization step for model parameters, and their final values may have not a reliable physical interpretation [16].

**Table 3.1:** Experimentally derived parameters for SRB and BCCY models from viscosity data in Fig. 3.6.

| $\mu_{0,exp}$ | $\dot{\gamma}_{0,exp}$ | $K_{exp}$ | $n_{exp}$ | $\dot{\gamma}_{\infty,exp}$ | $\mu_{\infty,exp}$ |
|---|---|---|---|---|---|
| 60 $mPas$ | 0.172 $s^{-1}$ | 28.171 $mPas^n$ | 0.571 | 18.822 $s^{-1}$ | 8 $mPas$ |

**Fitting capabilities based on optimization procedures.** Another test of the fitting capabilities of the SRB model can be performed by investigating whether, after the SRB and BCCY model parameters have been calibrated through the solution of an optimization problem, they can be used directly for the PWM approximation, which is necessary for the quasi-analytical flow solutions presented in Sections 3.2 and 3.3. Given the wide ranges of viscosities, model calibration is performed via minimization of the lognormal mean absolute percentage errors (LMAPE)

$$\text{LMAPE} = \frac{1}{N}\sum_{i=1}^{N}\left|\frac{\log f_i}{\log a_i} - 1\right| \tag{3.69}$$

between the $N$ experimental data $a_i$ of the hydrogel reported in Colosi *et al.*[103] and model values $f_i$. Accordingly, the coefficient of determination has been evaluated by means of LMAPE

$$R^2_{LMAPE} = 1 - \frac{\sum_{i=1}^{N}\left|\frac{\log f_i}{\log a_i} - 1\right|}{\sum_{i=1}^{N}\left|\frac{\bar{y}_L - \log a_i}{\log a_i}\right|}, \tag{3.70}$$

with $\bar{y}_L = \sum_i^N \log a_i/N$.

**Table 3.2:** Primary (black) and derived (red) fitting values of the SRB, PWM and BCCY models; $\mu_x[mPas]$, $\dot{\gamma}_x$ $[s^{-1}]$, $n$ $[-]$, $a$ $[-]$, $LMAPE$ $[-]$, $R^2$ $[\%]$.

| Model | $\mu_0$ | $\dot{\gamma}_0$ | $n$ | $\mu_\infty$ | $\dot{\gamma}_\infty$ | $a$ | LMAPE | $R^2_{LMAPE}$ |
|---|---|---|---|---|---|---|---|---|
| SRB | 60.0 | 0.174 | 0.573 | 8.14 | 18.819 | 2 | 0.0155 | 93.1 |
| BCCY | 60.1 | 0.266 | 0.289 | 7.70 | 14.848 | 2 | 0.0034 | 98.5 |

The fitting values of primary and derived model parameters are reported in Table 3.2, together with the LMAPE value at optimum, as well as the coefficient of determination $R^2_{LMAPE}$. Even if the individual LMAPE errors are slightly higher than the BCCY model, the coefficient of determination $R^2_{LMAPE}$ shows very good fitting capabilities for the SRB model. However, if the optimal values of the BCCY model are used in the PWM approximation, a bad fitting is obtained (see Fig. 3.7), and that would result in a large error in the evaluation of the approximated

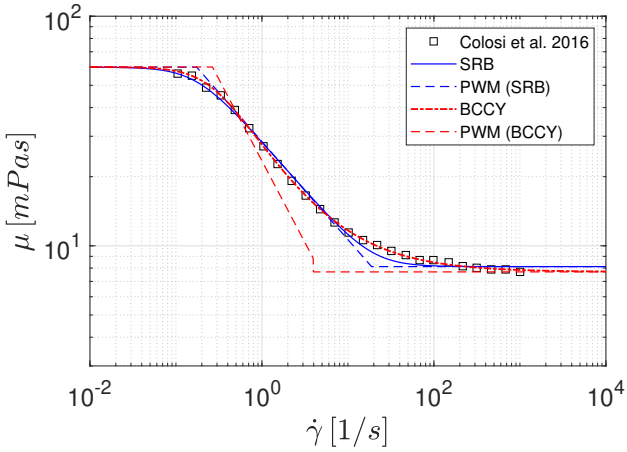


**Figure 3.7:** Comparison between the PWM model with SRB parameters (Table 3.2) (PWM (SRB)) and the PWM model with BCCY parameters (Table 3.2) (PWM (BCCY)).

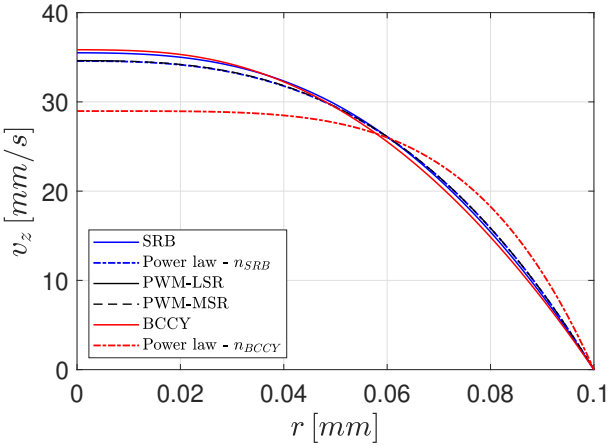


**Figure 3.8:** Comparison between the velocity profile solutions of the SRB, BCCY and PWM models for the power law flow analysed. The model parameter values are reported in Table 3.3.

analytical solutions presented in Sections 3.2 and 3.3. On the other hand, the PWM fitting is accurate by employing the optimal values obtained for the SRB model, confirming that the SRB approach solves the identifiability issue of BCCY.

**Power law velocity profiles.** One may ask if these identifiability issues of the BCCY model may or not be relevant in terms of velocity profiles and thus of bio-ink flow solutions. In particular, taken as reference a nozzle with a radius $R = 100\,\mu m$ and an extrusion velocity $\bar{V} = 20\,mm/s$, by using the PWM approximation, the

**Table 3.3:** Primary (black) and derived (red) parameter values of the SRB and BCCY model used for the flow analysis in Fig. 3.8; $\mu_x[mPas]$, $\lambda$ $[s]$, $\dot{\gamma}_x$ $[s^{-1}]$, $n$ $[-]$, , $a$ $[-]$.

| Model | $\mu_0$ | $\lambda$ | $\dot{\gamma}_0$ | $n$ | $\dot{\gamma}_\infty$ | $\mu_\infty$ | $a$ |
|---|---|---|---|---|---|---|---|
| SRB | 60.0 | $9.58 \cdot 10^{-2}$ | 10.4 | 0.573 | 1128 | 8.14 | 2 |
| BCCY | 60.1 | $6.27 \cdot 10^{-2}$ | 16.0 | 0.289 | 891 | 7.70 | 2 |

parameter sets of the BCCY and SRB model in Table 3.2 has been varied in order to have a power law flow in the nozzle. This procedure led to the parameter set reported in Table 3.3. The PWM approximation parameters have been chosen equal to those of the SRB model. As indicated by the PWM velocity solution in Fig. 3.8, the Newtonian low-shear rate region (LSR) extends only to a tiny region below the 0.75 % of the nozzle radius $R$; while the power law medium-shear rate region (MSR) covers all the domain. Therefore, the axial velocity solutions of the SRB and BCCY models should almost coincide with those of the corresponding power law velocity profiles reading

$$v_{z,\,PL}(r) = \frac{3n+1}{n+1} V_0 \left[ 1 - \left( \frac{r}{R} \right)^{\frac{n+1}{n}} \right] , \tag{3.71}$$

with $r$ as radial coordinate of the nozzle. Figure 3.8 shows that the power law velocity profile with $n = n_{SRB} = 0.573$ in Eq. (3.71) approximates well the exact numerical SRB and BCCY solutions, while employing $n = n_{BCCY} = 0.289$ leads to a significant error. This outcome further proves identifiability capacity of the SRB model to capture the physical interpretation of the power law index $n$, and the inferring problem of the the BCCY model on that parameter, which consequently affects the reliability and accuracy of the quasi-analytical solutions presented in Sections 3.2 and 3.3.

### 3.4.2 Flow dynamics in a cylindrical nozzle

**Rheological data & Reference operating conditions.** The PWM approximation in Eqs. (3.1)-(3.2) with the experimentally derived parameters reported in Table 3.1 and the fluid dynamic expressions in Eqs. (3.9)-(3.11) have been applied to an extrusion bioprinting process. The gelatin methacroyl-alginate (GelMA) based cell-laden hydrogel presented by Colosi *et al.*[103] has been taken as reference fluid. Regarding the geometry and the operating conditions, common extrusion-based bioprinting values have been chosen [49, 104] by considering a cylindrical needle with a $R = 420$ $\mu m$ inner radius and an extrusion velocity $\bar{V}$ ranging between $0 - 12$ $mm/s$.

**Flow analysis.** The extrusion velocity $\bar{V} = Q/(\pi R^2)$ of the bioprinting process calculated from Eqs. (3.9b), (3.10f), (3.11i) is shown in Fig. 3.9 (left axis) as function of the pressure drop per unit length $\Delta p/L$ applied to the nozzle. Moreover, Fig. 3.9 (right axis) shows the $R_0$ and $R_\infty$ values in Eq. (3.8) corresponding to the applied $\Delta p/L$.

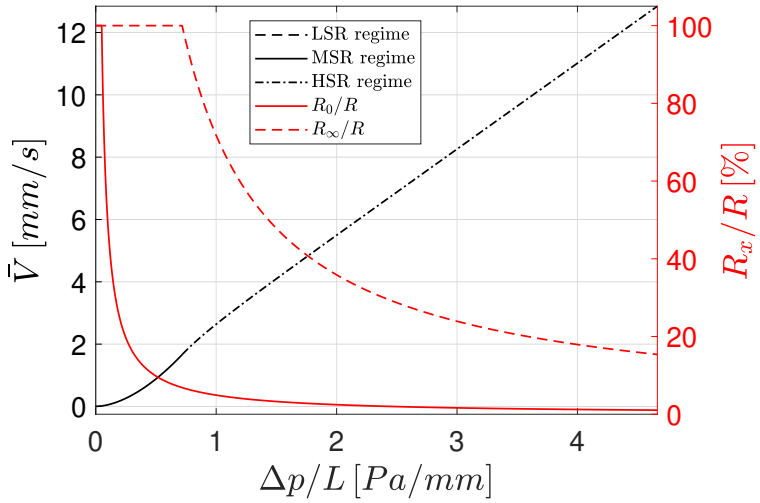


**Figure 3.9:** Extrusion velocity in function of the applied pressure drop per unit length (black, left axis); corresponding $R_0$ and $R_\infty$ values (red, right axis) (see Eq. (3.8)).

It is possible to note how the flow immediately exits from the LSR condition at very low pressure drop values. Indeed, $R_0$ in Eq. (3.8) quickly drops down and the LSR regime for the $\Delta p/L - \bar{V}$ relationship is barely visible. This behaviour is due to the low value for $|\dot{\gamma}_0|$ and the inner radius values at hand, which determine $|\dot{\gamma}_{wall}| > |\dot{\gamma}_0|$ at very low values of $\Delta p/L$, causing the viscosity to leave the LSR region. Then, the flow is characterized by a MSR regime up to an extrusion velocity of about 2 $mm/s$, and enters in the HSR regime. For instance, for an extrusion velocity of 12 $mm/s$, the power-law zone radius results $R_\infty \simeq 0.2R$. By investigating the slope of the extrusion velocity curve, it is interesting to see the linear relationship between $\bar{V}$ and $\Delta p/L$ in the HSR flow condition referring to the Newtonian relation $\Delta P/L = 8\mu_\infty \bar{V}/R^2$, and how the shear-thinning properties of the bio-inks in the MSR flow condition allow to increase extrusion velocity slope compared to the initial Newtonian $\mu_0$ zone.

**Velocity profiles.** The velocity profiles in Eqs. (3.9)-(3.11) have been computed in Fig. 3.10 for each of three flow conditions LSR, MSR and HSR. In particular, three points have been selected in Fig. 3.9: the last point of the LSR regime with a pressure drop per unit length $\Delta p/L = 4.91 \cdot 10^{-2}\ Pa/mm$ corresponding to an analytical extrusion velocity $\bar{V}_1 = 1.81 \cdot 10^{-2}\ mm/s$ and $R_0 = R$; a second point in the MSR regime with a $\Delta p/L = 1.97 \cdot 10^{-1}\ Pa/mm$ corresponding to a $\bar{V}_2 = 1.73 \cdot 10^{-1}\ mm/s$ and $R_0 = 0.25R$; and a third point in the HSR regime with a $\Delta p/L = 2.39\ Pa/mm$ corresponding to a $\bar{V}_3 = 6.57\ mm/s$ and $R_\infty = 0.30R$.

The flow starts with a Newtonian profile (Fig. 3.10a) with an axial velocity equal to $2\bar{V}_1$, then assumes a flat outline with an axial velocity smaller than $2\bar{V}_2$ typical of the shear-thinning fluid (Fig. 3.10b), and a dominant Newtonian profile

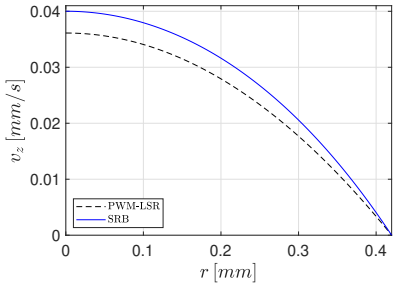


**(a)** $\Delta p/L = 4.91 \cdot 10^{-2}\ Pa/mm$

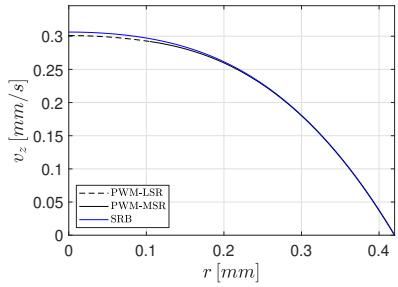


**(b)** $\Delta p/L = 1.97 \cdot 10^{-1}\ Pa/mm$

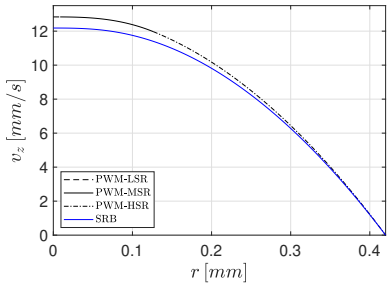


**(c)** $\Delta p/L = 2.39\ Pa/mm$

**Figure 3.10:** Velocity profiles for the three main flow conditions: (a) LSR, (b) MSR and (c) HSR.

with a power-law bulk flow in the latter case (Fig. 3.10c).

**Table 3.4:** Percentage errors of the PWM solution for the three main flow conditions LSR, MSR and HSR analysed in Fig. 3.10.

| | LSR (Fig. 3.10a) | MSR (Fig. 3.10b) | HSR (Fig. 3.10c) |
|---|---|---|---|
| $e_{\bar{V}_\%}[\%]$ | 1.98 | 0.10 | 0.59 |
| $e_{V_{axial,\%}}[\%]$ | 9.73 | 1.73 | 5.37 |

All the profiles have been compared with the numerical solutions obtained by solving Eq. (3.5) for the SRB model (i.e. the non-approximated version of PWM) with the same $\Delta p/L$, by analysing the extrusion velocity percentage error $e_{\bar{V}_\%}$ and the axial velocity percentage error $e_{V_{axial,\%}}$ between the analytical (PWM) and numerical (SRB) solutions

$$e_{\bar{V}_\%} = \frac{\frac{1}{R^2}\int_0^R 2r\,|v_{z,PWM}(r) - v_{z,SRB}(r)\,|\,dr}{\bar{V}_{SRB}}, \quad e_{V_{axial,\%}} = \frac{|v_{z,PWM}(0) - v_{z,SRB}(0)\,|}{v_{z,SRB}(0)}\,. \tag{3.72}$$

The obtained errors are reported in Table 3.4. Even if the maximum error of PWM solution on the axial velocity for the LSR case is about 10 %, the maximum

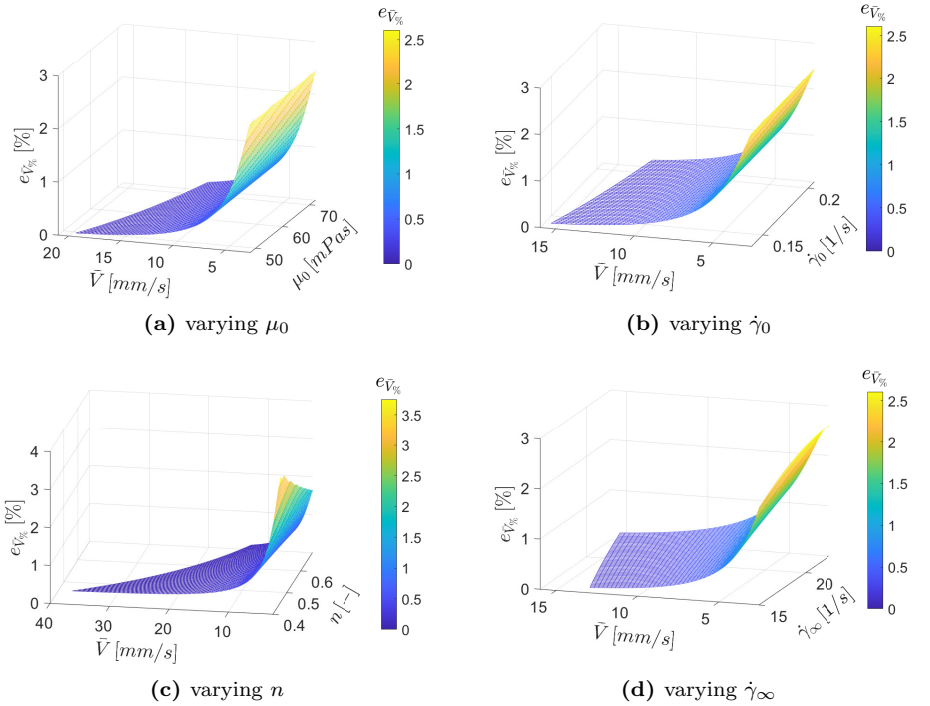


**(a)** varying $\mu_0$ **(b)** varying $\dot{\gamma}_0$

**(c)** varying $n$ **(d)** varying $\dot{\gamma}_\infty$

**Figure 3.11:** Parametric analysis of the extrusion velocity percentage error (Eq. (3.72)) by varying one by one the parameter values in Table 3.1 considered as nominal values. (a) varying $\mu_0$, (b) varying $\dot{\gamma}_0$, (c) varying $n$, and (d) varying $\dot{\gamma}_\infty$.

extrusion velocity error is less than 2%, since the axial velocity values have a lower weight on the extrusion velocity computation than the velocity values near the wall, resulting in a good agreement between the PWM and SRB solutions. For the application at hand, the errore decreases in the HSR regime and is minimum in the MSR one.

Next, another validation of the analytical solution (PWM approximation) has been performed through the parametric campaign shown in Fig. 3.11, wherein the analytical extrusion velocity $\bar{V}$ and the extrusion velocity percentage error $e_{\bar{V}_\%}$ in Eq. (3.72) have been computed. Each rheological parameter $(\mu_0, \dot{\gamma}_0, n, \dot{\gamma}_\infty)$ have been varied in a range of $\pm\,20\,\%$ from its nominal value while keeping the others fixed with extrusion velocities ranging between $0 - 40\,mm/s$.

The maximum extrusion velocity error is about 2.5%, except in the parametric analysis of the power-law index $n$ which shows an error about 3.5%. For each analysis, the maximum error is reached in the region of the extrusion velocity close to $2\,mm/s$, corresponding to the final value of the MSR regime (see Fig. 3.9); then, the errors decrease as the extrusion velocity increases and moving the flow condition to the HSR regime. Furthermore, it is interesting to note in Fig.3.11c how the error decreases as the the power-law index increases, since the fluid tends to the Newtonian behaviour.

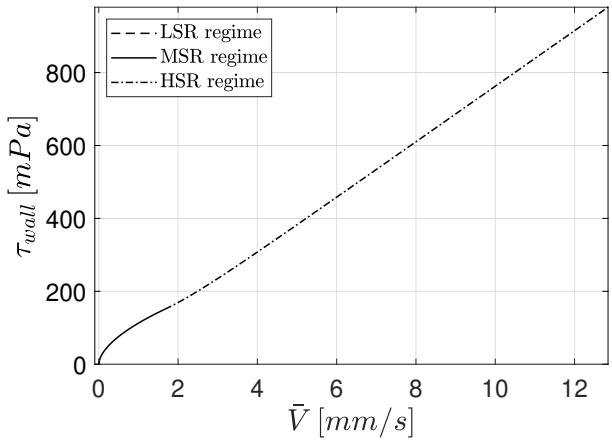


**Figure 3.12:** Wall shear-stress as a function of the extrusion velocity for different flow conditions (Eqs. (3.9)-(3.11)). The LSR solution is negligible since the fluid quickly leaves the LSR regime in Fig. 3.9 for the application at hand.

**Wall-shear stress.** As described in Section 3.2, in extrusion bioprinting, it is desirable to limit shear stress acting on cells and thus its maximum value occurring at the nozzle wall, namely the wall-shear stress (see Eq. (3.5)), which has been plotted in Fig. 3.12 as a function of extrusion velocity. Due to the low GelMA viscosity values, the maximum shear-stress value corresponding to 12 $mm/s$ extrusion velocity is limited to a very low 900 $mPa$ value. Analogously to the afore-introduced considerations, a linear relationship in the HSR regime is observed, like for a fully Newtonian flow $\bar{V} = \tau_{wall}R/(4\mu)$, as well as a reduction in the wall shear-stress slope because of the GelMA shear-thinning properties.

Next, two parametric analyses has been carried out in Fig. 3.13 for the damage extrusion velocity $\bar{V}_{dam.}$ in Eq. (3.13), by imposing a $\tau_{wall} \leq \tau_{dam.} = \tau_\infty = 151\,mPa$ in Fig. 3.13 (a-b), and a $\tau_{wall} \leq \tau_{dam.} = \phi\tau_\infty = 1\,Pa$ in Fig. 3.13 (c-d). Then, the parameters have been varied in pairs in a range of $\pm\,75\%$ from their nominal values in Table 3.1, while keeping the others fixed. It is possible to note how the zero-shear rate viscosity $\mu_0$ and the zero-shear rate $\dot{\gamma}_0$ have a negligible influence on the damage extrusion velocity $\bar{V}_{dam.}$ which remains constant at about $1.66\,mm/s$ and $13.1\,mm/s$ for the two damage shear stress values respectively. This outcome arises since the flow leaves the LSR regime at very low extrusion velocities. On the other hand, for the lower damage shear stress, variations in the power-law index $n$ and the infinity-shear rate $\dot{\gamma}_\infty$ determine greater variations of the $\bar{V}_{dam.}$. While for the higher damage shear stress value, only the $\dot{\gamma}_\infty$ parameters influences the damage extrusion velocity, since in this case the flow is almost entirely Newtonian.

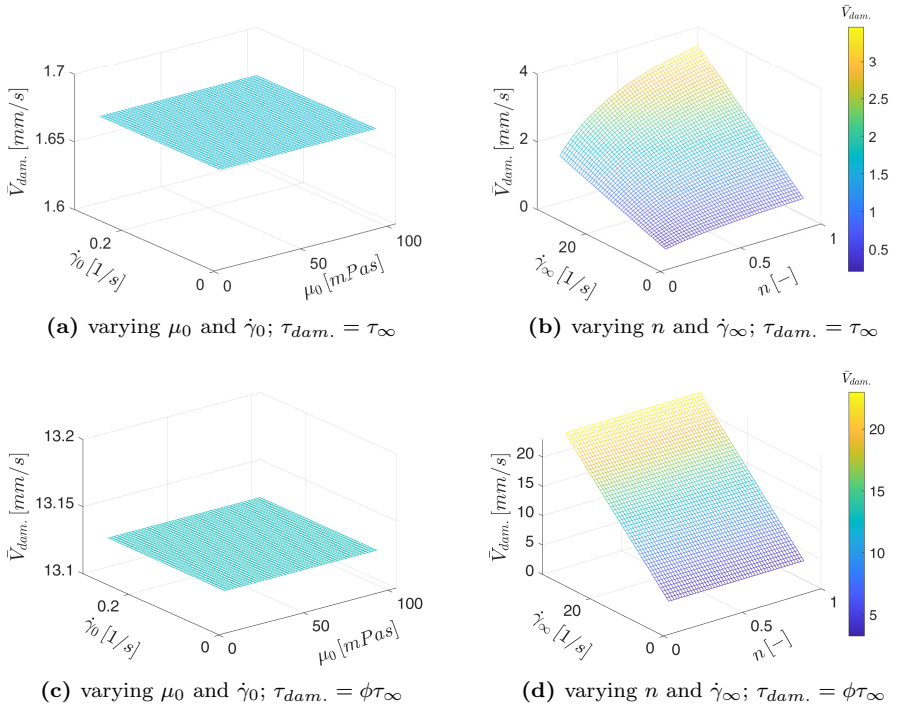


**(a)** varying $\mu_0$ and $\dot{\gamma}_0$; $\tau_{dam.} = \tau_\infty$

**(b)** varying $n$ and $\dot{\gamma}_\infty$; $\tau_{dam.} = \tau_\infty$

**(c)** varying $\mu_0$ and $\dot{\gamma}_0$; $\tau_{dam.} = \phi\tau_\infty$

**(d)** varying $n$ and $\dot{\gamma}_\infty$; $\tau_{dam.} = \phi\tau_\infty$

**Figure 3.13:** Parametric analyses of the damage extrusion velocity (Eq. (3.13)) by varying the parameter values in Table 3.1 and assuming as damage shear stress $\tau_{dam.}$: (a-b) $\tau_\infty = 151\,mPa$; (c-d) $\phi\tau_\infty = 1\,Pa$.

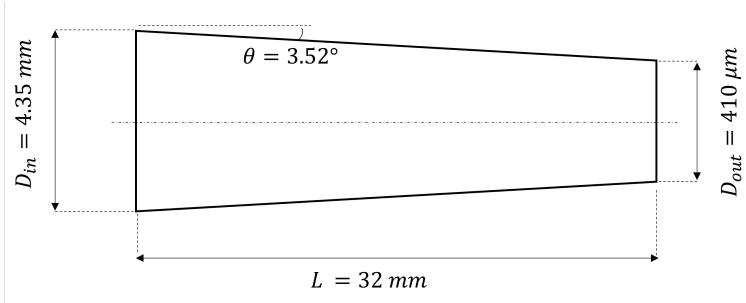


**Figure 3.14:** Geometry of the nozzle used in the experimental setup.

## 3.5 Reproduction of an experimental setup and validation

The quasi-analytical solution for a non-Newtonian inelastic fluid flowing in a tapered nozzle and described in Section 3.3 has been employed to analyse experimental data on the bioprinting process provided by LaBS at Politecnico of Milan, Belgio *et al.*[105]. In particular, they used an extrusion bioprinter with a conical nozzle

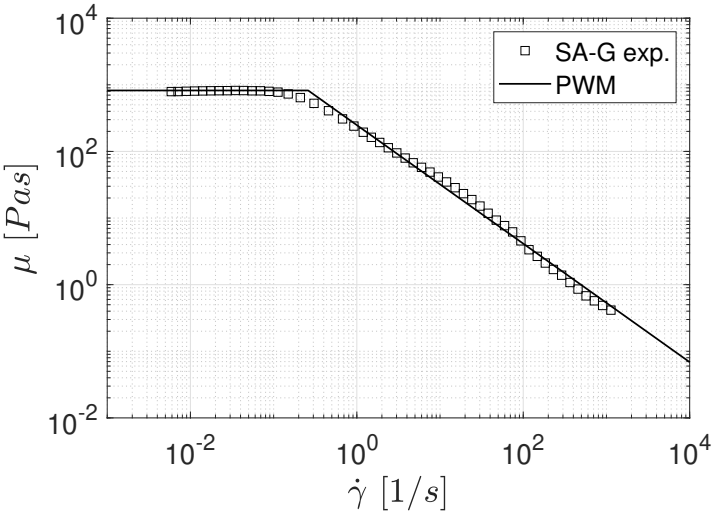


**Figure 3.15:** Viscosity data of the SA-G fluid [105] and the corresponding fitting obtained through the PWM approximation in Eq. (3.57).

geometry shown in Fig. 3.14, by setting as printing parameters an outlet diameter $D_{out} = 410\,\mu m$, an extrusion velocity referred at the outlet $\bar{V}_{out} = 10\,mm/s$ with a corresponding dispensing pressure applied to the nozzle $\Delta p_{exp} \simeq 25\,kPa$ (the pressure drop between the cartridge and the nozzle can be neglected since the cartridge has a greater diameter of $9.5\,mm$). A mixture of sodium alginate gelatin bio-ink is used. This hydrogel presents a high cytocompatibility [106, 107], a low sol-gel transition temperature around $20°C$, a cross-linking capability in $CaCl$ bath. Cell density varies between $1 - 5 \cdot 10^6\,cells/ml$. Regarding the rheological properties

**Table 3.5:** Fitting values of the PWM model; $\mu_0$, $\dot{\gamma}_0$ , $\tau_0$, $n$, $K$.

| $\mu_0$ | $\dot{\gamma}_0$ | $\tau_0$ | $n$ | $K$ |
|---|---|---|---|---|
| 822.7 $Pas$ | 0.260 $s^{-1}$ | 213.9 $Pa$ | 0.111 | 248.2 $Pas^n$ |

of the bio-ink, the viscosity measures of the SA-G fluid has been reported in Fig. 3.15 together the fitting obtained through the PWM approximation in Eq. (3.57). It shows a high viscosity at low shear rates which supports the scaffold structure to not collapse after the printing, and a high shear-thinning behaviour reducing the hydraulic resistance during the extrusion (see Eq. (3.53)). The fitting values of the PWM approximation parameters are reported in Table 3.5. In addition, it has been investigated whether or not the presence of the cells in the fluid can influence the rheological properties of the bio-ink, and the results showed that there were no statistical differences between the two cases accordingly to the Kruscal-Wallis test.

**Flow dynamics.** As described in Section 3.3, there are analytical solutions for a conical nozzle flow only for a Newtonian or a power law fluid, while the SA-G

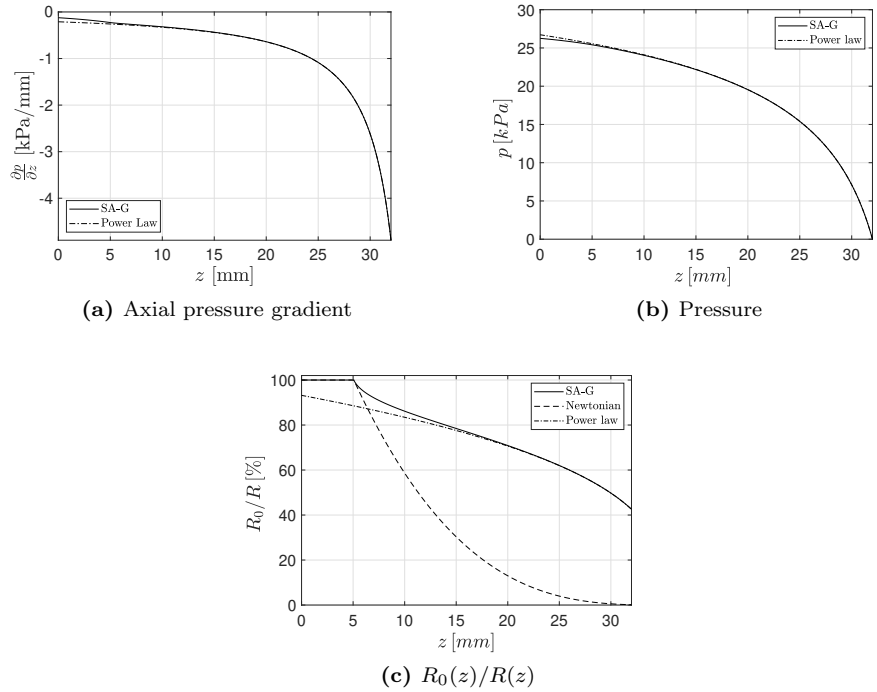


**(a)** Axial pressure gradient

**(b)** Pressure

**(c)** $R_0(z)/R(z)$

**Figure 3.16:** Axial pressure gradient (a), pressure (b) and percentage radius $R_0(z)/R(z)$ (in Eq. (3.59)) delimiting the Newtonian annular section as a function of the nozzle axial coordinate.

exhibits an intermediate behaviour. Thus, in order to evaluate the axial pressure gradient value along the nozzle axis it has been implemented the procedure presented in Algorithm 1, by setting a flow rate $Q = 1.32\,mm^3/s$ corresponding to the extrusion velocity at the outlet imposed experimentally. As one can note in Fig. 3.16(a), due to the radius reduction along the axis, the axial pressure gradient presents very small values at the inlet region, with a fast increase at the outlet, accordingly to the radius-pressure gradient relationship in the flow rate Eqs. (3.22), (3.40). Furthermore, it shows an almost overlapped solution to the power law flow case. Regarding the pressure drop applied to the nozzle, first preliminary estimates considering the SA-G flowing in cylindrical nozzles with a radius $R = R_{in} = 2.175\,mm$ and $R = R_{out} = 205\,\mu m$, and the same length $L = 32\,mm$ of the conical nozzle, turned out in $\Delta p|_{R_{in}} = 11.4\,kPa$ and $\Delta p|_{R_{out}} = 156\,kPa$ respectively (see Eqs. (3.10)), with very different values from the experimental one $\Delta p_{exp} \simeq 25\,kPa$. Even the estimate assuming a conical nozzle and a Newtonian fluid with viscosity $\mu = \mu_0$ has resulted through the Eq. (3.23) to a much larger wrong value of $\Delta p = 1736\,kPa$. Therefore, a one dimensional finite difference scheme with a second order accuracy has been applied to the axial pressure gradient solution of the SA-G fluid to derive the pressure solution field in Fig. 3.16(b). It is noteworthy that it presents a pressure drop estimation $\Delta p = 26.6\,kPa$ close to the experimental $\Delta p_{exp} \simeq 25\,kPa$, with a value grater than the 6.4%. Figure

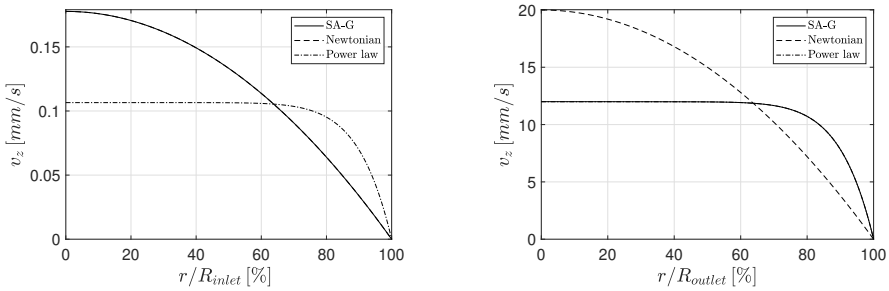


**(a)** Inlet **(b)** Outlet

**Figure 3.17:** Axial velocity at the inlet (a) and outlet (b) section as a function of the radial coordinate referred to the radius of the corresponding section.

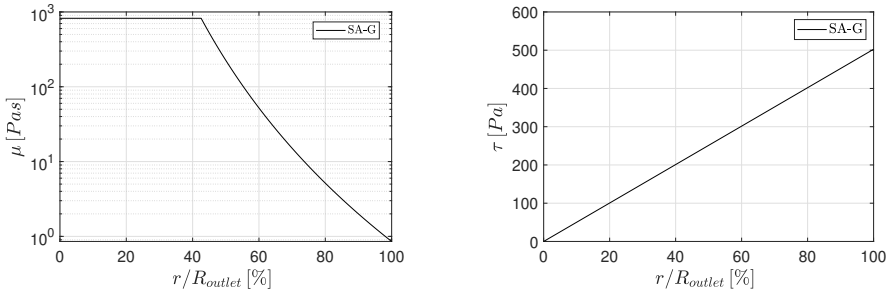


**(a)** Viscosity **(b)** Shear stress

**Figure 3.18:** Viscosity (a) and shear stress (b) values at the outlet section as a function of the percentage radial coordinate.

3.16(c) shows the percentage radius $R_0(z)/R(z)$ value in Eq. (3.59) delimiting the Newtonian and power law annular sections of the two PWM approximation's viscosity regions. Due to the high $\tau_0$ value of the SA-G, the flow has a full Newtonian behaviour up to $z = 5\,mm$, then it has an intermediate trend accordingly to the relation in Eq. (3.63), until it reaches a solution equal to the power law case at $z = 15\,mm$, showing at the outlet a Newtonian annular section with a percentage radius of 42 %.

The velocity profiles as a function of the percentage radial distance at the inlet and outlet section have been reported in Fig. 3.17. According to results in Fig. 3.16, the flow presents a Newtonian parabolic profile at the inlet, and a flat-plug flow like profile at the outlet typical of power law fluids with a high shear-thinning index, with a maximum value below the double of the mean velocity $2\bar{V}_{out} = 20\,mm/s$.

Finally, the viscosity and shear stress values at the outlet section have been plotted in Fig. 3.18. The flow presents a Newtonian viscosity $\mu = \mu_0 = 822.7\,Pas$ up to $r/R_{out} = 42\%$, with a remarkable rapid decrease below $1\,Pas$ at the nozzle wall. The shear stress shows a linear distribution along the radius in accordance

with Eq. (3.47), with a maximum value at the wall $\tau_{wall,out} = 502\,Pa$. Such value may cause a cell damage as in literature a shear stress above $1 - 10\,Pa$ has been reported [108]. But the experimental tests performed one day after printing shown a cell viability above 98 %. A possible explanation could be that during extrusion the cells generally position away from the nozzle wall and closer to the axis at lower stress values. In order to investigate this outcome, the Chapter 4 presents a fluid-structure interaction (FSI) approach adopted to analyse more in detail the phenomena occurring between the fluid and cells of the bio-ink.

## 3.6 Limitations

The quasi-analytical framework presented in this chapter provides quasi-analytical solutions for bio-inks flowing in cylindrical and slightly tapered nozzles. In particular, the bio-ink is considered as a homogeneous fluid with an inelastic rheological behaviour described through the PWM approximation in Eq. (3.1). Despite the developed model presents accurate solutions as proved in Sections 3.4.2 and 3.5, in general bioprinting nozzles can present more complex geometries. Even remaining in the case of micro-channels with 2D axial symmetry, a numerical computational fluid dynamics approach is required. Indeed, nozzles with a non-small taper angle (see the hypothesis in Eq. (3.14)), or with sharp and local flow section reductions, present non-negligible radial components in the mass and momentum conservation Eqs. (2.8), (2.28), and cannot be treated in terms of pressure and velocity solutions through an analytical method [109]. Furthermore, in addition to the cell damage caused by shear stresses analysed in this approach, also the extensional stresses arising from flow section variations could reduce the cell viability [49], and they should be taken into account for a more accurate evaluation. Moreover, as described in Section 2.1, when addressing higher cell densities and larger cell dimensions, the homogeneous flow hypothesis begins to no longer be valid, and the bio-ink should be treated as a heterogeneous flow to adequately analyse the mutual influence between the two phases. Therefore, the next Chapter 4 presents the numerical model developed to accurately analyse the phenomena taking place during the extrusion between the cells and the hydrogel within the bio-ink.

# Chapter 4

# Numerical modelling of fluid-structure interaction

This chapter presents the numerical model developed to describe the bio-ink as a heterogeneous flow (see Section 2.1). It analyses the Fluid-Structure Interaction (FSI) occurring between the two bio-ink phases corresponding to the polymeric fluid and the biological cells. This model allows a more detailed description of the phenomena taking place during the bioprinting process, at the expense of a higher computational cost. The Section 4.1 introduces the FSI modelling applied to the extrusion bioprinting case and the contact model used to describe the interaction between the cells within the bio-ink and the nozzle wall. Then, the Section 4.2 describes the fluid solver used which is based on an immersed boundary technique. The Section 4.3 presents the structural solver implemented, and the Section 4.4 illustrates the numerical modelling of the mechanical coupling between the two phases. Finally, the Section 4.6 shows the results of the simulations performed.

## 4.1 General rationale in bioprinting modelling

The fluid-structure interaction (FSI) is the mutual exchange of forces between a solid structure and a surrounding fluid taking place at the interface surface between the two media. In bioprinting, the presence of cells within the bio-ink locally modifies the velocity and pressure of the fluid phase during the extrusion as shown in Section 4.6. The velocity and pressure fields in turn determine the stress and strain of cells because of the mechanical coupling at the interface. Then, the new

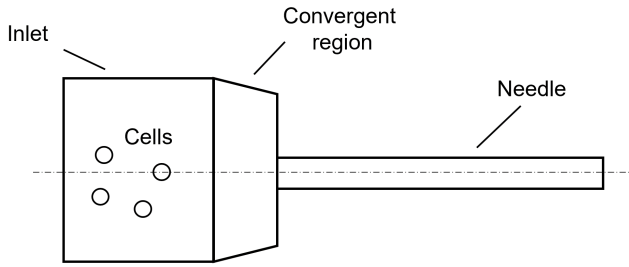


**Figure 4.1:** A standard nozzle geometry used in extrusion bioprinting [49, 62].

deformed configuration of cells affects the fluid solution in a two-way feedback. The FSI effects are more relevant especially when the cell dimensions are no longer negligible compared to those of the nozzle, and the cell density is comparable to that of the fluid due to the added-mass effect. Depending on the cell type and on the nozzle chosen for the printing, these aspects could be relevant in bioprinting flows.

In particular, by taking into account a standard nozzle geometry used in bioprinting and shown in Fig. 4.1, these aspects could be significant in the convergent region and in the needle part of the nozzle, wherein the cell dimensions could be comparable to the nozzle ones.

In general, FSI phenomena present an inherently nonlinear and time dependent nature, which allows the development of analytical and semi-analytical models only with simplified assumptions and elementary geometries [110]. On the other hand, in the last decades great advances have been done in the FSI numerical modelling research, which enables nowadays a reliable and accurate simulation of complex 3D FSI phenomena [111–116].

The main challenges in computational modelling of FSI problems are: the problem formulation, taking place at the continuous level and depending on the assumptions made it affects the whole numerical solution; the numerical discretization of the fluid and structure domains, which must take into account and adapt to the displacements of the moving solid domain; and the fluid-structure coupling, imposed through the coupling conditions which ensure the equality of kinematics and stress of material points lying on the interface surface between the two media [111]. Therefore, a FSI framework must solve in parallel the set of partial differential equations and boundary conditions associated to the fluid and structure fields, and it must guarantee the two domains to not overlap at their interface, which represents the space region wherein the information exchange takes place between the Eulerian description of the fluid and the Lagrangian description of the structure.

There are two major classes of FSI numerical models: *strongly-coupled* (also referred as *monolithic*) and *loosely-coupled* (also referred as *partitioned*) approaches [111, 112]. The strongly coupled procedures handle the fluid and structure equations and the mesh moving with the same mathematical framework and solve simultaneously their dynamics in the same time step. The coupling conditions at the interface are implicitly imposed in the solving algorithm and in general they

provide a more robust and accurate solution. However, they require more computational resources since the algebraic blocks of the two physical systems are coupled together resulting in a bigger final left-hand side matrix. Furthermore, the monolithic algorithm are usually specific for each FSI problem at hand, requiring a specific code developing for each case. On the other side, the loosely coupled procedures solve the fluid, structure and the mesh moving sequentially. Commonly they start from the computation of the fluid solution with the current configuration of the structure; then through the coupling conditions, they transfer to the structure the fluid dynamics loads at the interface to calculate the new solid deformation; and as a last step, they update the mesh of two domains. Since in this case the two physical systems are solved separately, it is possible to adopt existing fluid and structure solver already validated and used in literature for many complex fluid or structural problems [112].

Another classification of FSI solvers is based on the treatment of domain meshes [112, 117]. In the *body-fitted mesh* (also referred as *conforming mesh*) algorithms the interface surface nodes are a part of the solution and they fit the fluid mesh to the current configuration of the structure mesh. Therefore, due to the structure motion they require a re-mesh of the fluid domain after each time step integration [118, 119]. Conversely, the *non-body-fitted mesh* (also referred as *non-conforming mesh*) algorithms consider the interface location and coupling conditions as a constraint to impose to the solution through an interpolation procedure, thus not requiring an update of the fluid mesh [120, 121].

The suitability of the procedure adopted to solve the FSI problem in terms of solution stability, convergence and accuracy is strictly connected to the physical properties of the two domains. In case of cells extrusion in bioprinting flows the two media have a very different characteristic dynamics velocities. Indeed, a typical extrusion speed for the fluid is $V_0 = 20\,mm/s$ [49, 51, 68] and by taking as reference for the structure a cell density $\rho_{cell} = 1.1\,g/ml$ [70–72] and, assuming a linear elastic behaviour, a Young's modulus $E = 5\,kPa$ [122–126] the corresponding characteristic velocity for the structure turns out $V_s = \sqrt{E/\rho_{cell}}$. Thus, the reduce velocity number $V_{reduced}$ representing the ratio between the two characteristic velocities results [110]

$$V_{reduced} = \frac{V_0}{V_s} = \frac{V_0}{\sqrt{\dfrac{E}{\rho_{cell}}}} = 9.38 \cdot 10^{-3} \ll 1 \ , \tag{4.1}$$

indicating a structure with a much faster dynamics than the fluid. The corresponding reduced time $t_{reduced}$ between the two characteristic times turns out

$$t_{reduced} = \frac{t_F}{t_S} = \frac{D/V_0}{D_{cell}/V_s} = \frac{D}{D_{cell} V_{reduced}} = 711 \gg 1 \ , \tag{4.2}$$

where it has been considered as reference a nozzle diameter $D = 200\ \mu m$ [49, 51, 68] and a cell diameter $D_{cell} = 30\ \mu m$ [45, 127].

Therefore, since the cell presents a much quicker characteristic time than the fluid, in order to adequately capture the stress and strain of the structure during the extrusion, a loosely-coupled FSI procedure with a sub-iterative scheme for the structural solver has been implemented. Furthermore, considering the typical

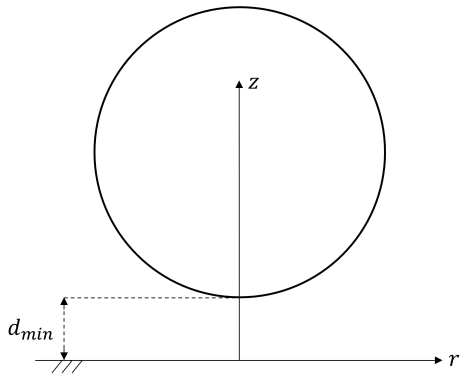


**Figure 4.2:** Schematic representation of a sphere approaching to a wall for the lubrification model reported in [130, 131].

cell density values of bio-inks with an order of magnitude of $10^6$ $cells/ml$ [68], in order to avoid the numerical issue of fluid grid re-meshing and to apply the coupling conditions at the interface between the two phases, a non-body-fitted mesh approach based on an immersed boundary method [128] with a moving-least-squares (MLS) reconstruction technique has been adopted [117, 129], as reported in detail in the next Section 4.4.

**Contact modelling.** As described in Section 2.5, the cells within the bio-ink can be modelled as suspended spherical particles immersed in a confined flow. When a sphere approaches to the nozzle wall or to another sphere, the presence of the interstitial fluid between the two bodies influences their dynamics. In particular, the squeezing out of the fluid from the gap generates a pressure increment which tends to push two bodies away from each other [132, 133]. The magnitude of the repulsive forces generated during the approaching of the bodies is strongly influenced by the density of intermediate fluid and of bodies. For example, in gas-fluidized beds of heavy particles experiments a real contact between particles has been observed [133] and could be modelled through the elastic/inelastic collisions models based on the impulse theorem [134]. On the other hand, when the fluid is a liquid with a density comparable to that of the colliding bodies, the particles actually do not touch themselves, approaching arbitrarily closely with a velocity great enough [133]. The latter case is that of bioprinting flows wherein the cells have a density around $\rho_{cell} = 1.1\ \rho$ of the water-based fluid [70–72]. An explanation of the not-contact between the colliding bodies can be given through the paradox based on the evaluation of the external force on a sphere approaching to a wall in the creeping flow approximation [131, 132, 135, 136], which provides an infinity pressure build-up as the gap tends to zero and could cause the liquid film rupture, and also undermine the continuum hypothesis.

In the present work, the contact dynamics between the cells and the nozzle wall and the cells themselves is described through a proximity model. It assumes during the approach between bodies the pressure forces are large enough to prevent their physical contact. It is based on the lubrification model derived from the

Stokes equation and represented schematically in Fig. 4.2 reported in [130, 131]. Specifically, considering a sphere with radius $R_s$ approaching a wall with a velocity $V_s$ and immersed in a Newtonian fluid with viscosity $\mu$, the repulsive pressure acting on the sphere surface in non-dimensional form reads

$$p'_{rep} = \frac{3}{\epsilon'^2 \left(1 + \eta'^2\right)^2} \ , \tag{4.3}$$

where $p'_{rep} = p_{rep}/(\mu V_s/R_s)$, $\epsilon' = d_{min}/R_s$ and $\eta' = r/\left(R_s\sqrt{2\epsilon'}\right)$.

## 4.2 Immersed boundary method

To solve numerically the continuity Eq. (2.8) and the momentum Eq. (2.30) it has been used a non-dimensional flow solver based on a direct-forcing immersed boundary (IB) method [117, 128] in Cartesian coordinates. Their corresponding non-dimensional forms in Eqs. (2.31), (2.32) and here reported result

$$\frac{\partial \boldsymbol{v}'}{\partial t'} + (\boldsymbol{v}' \cdot \nabla')\boldsymbol{v}' = -\nabla' p' + \frac{1}{Re_\infty}\nabla'^2 \boldsymbol{v}' + \frac{1}{Re_\infty}\nabla' \cdot [2\Delta' \mu'(\dot{\gamma}')\mathbf{E}'] + \mathbf{f}'_{IB} \ , \tag{4.4}$$

$$\nabla' \cdot \boldsymbol{v}' = 0 \ , \tag{4.5}$$

with reference values a nozzle diameter $D$, an extrusion velocity $V_0$, a time $t_f = D/V_0$, a fluid density $\rho$, a pressure $p_0 = \rho V_0^2$, an infinity-shear rate viscosity $\mu_\infty$ of the bio-ink, $Re_\infty = \rho V_0 D/\mu_\infty$ and with $\mathbf{f}'_{IB}$ representing the IB forcing term. The flow solver is based on the fractional-step method [137–139] and on a centred finite differences scheme [117, 128]. Thus, the semi-discretized momentum equation turns out

$$\frac{\hat{\boldsymbol{v}}' - \boldsymbol{v}'^n}{\Delta t} = -\nabla' p'^n + \frac{3}{2}H'^n - \frac{1}{2}H'^{n-1} + \frac{1}{2Re_\infty}\nabla'^2(\hat{\boldsymbol{v}}' + \boldsymbol{v}'^n) + G'^n_{NN} \ , \tag{4.6}$$

where it has been applied an explicit Euler scheme for the pressure term and for the the non-linear non-Newtonian term $G'^n_{NN} = \nabla' \cdot (2\Delta' \mu'^n \mathbf{E}'^n)/Re_\infty$, an implicit Crank-Nicolson scheme for the viscous term and an explicit Adams-Bashforth 2-steps scheme for the non-linear convective terms $H'$. The apex $n$ indicates the reference time step, $\hat{\boldsymbol{v}}'$ is an intermediate solution and $\Delta t'$ is the fluid simulation time step. The previous equation can be rewritten in delta form as [117, 128]

$$\left(1 - \frac{\Delta t' \nabla'^2}{2Re_\infty}\right)\Delta\hat{\boldsymbol{v}}' = \left(-\nabla' p'^n + G'^n_{NN} + \frac{3}{2}H'^n - \frac{1}{2}H'^{n-1}\right)\Delta t' + \frac{\Delta t' \nabla'^2 \boldsymbol{v}'^n}{Re_\infty} \ , \tag{4.7}$$

with $\Delta\hat{\boldsymbol{v}}' = \hat{\boldsymbol{v}}' - \boldsymbol{v}'^n$ and due to the implicit treatment of the viscous term at the left-hand side it would require the computationally expensive inversion of a large sparse matrix. Thus, it is possible to use a factorization technique [137–139] which reduces the computation cost by solving three simple tri-diagonal matrices

and yielding the intermediate solution $\hat{\boldsymbol{v}}'$. Then, the direct IB forcing term $\mathbf{f}'_{IB}$ is applied to impose the no-slip velocity boundary condition

$$\boldsymbol{v}'^{*} = \hat{\boldsymbol{v}}' + \mathbf{f}'_{IB}\Delta t' = \hat{\boldsymbol{v}}' + \left(\mathbf{f}'_{IB,nozzle} + \mathbf{f}'_{IB,cells}\right)\Delta t' \ . \tag{4.8}$$

The forcing term $\mathbf{f}'_{IB,nozzle}$ models the no-slip boundary condition between the fluid and the nozzle wall and it reads [128]

$$\mathbf{f}'_{IB,nozzle} = -\mathbf{RHS}'^{n-1/2} + \frac{\bar{\boldsymbol{v}}'^{bc} - \hat{\boldsymbol{v}}'}{\Delta t'} \ , \tag{4.9}$$

where $\mathbf{RHS}^{n-1/2}$ are the discretized terms of the right-hand side in Eq. (4.6), and $\bar{\boldsymbol{v}}'^{bc}$ is the linear approximation of the desired boundary condition to impose on the nozzle wall, namely $\boldsymbol{v}'^{bc} = \mathbf{0}$, and applied to the Eulerian node closest to the immersed boundary [128]. The $\mathbf{f}'_{IB,cells}$ forcing term models the no-slip condition between the fluid and the cells and it is based on the moving-least-squares (MLS) reconstruction technique described in detail in the next Section 4.4.

Once $\boldsymbol{v}'^{*}$ is known, in order to get a divergence-free velocity, namely satisfying the continuity Eq. (4.5), the solution is updated as

$$\boldsymbol{v}'^{n+1} = \boldsymbol{v}'^{*} - \Delta t' \nabla' \Phi' \ , \tag{4.10}$$

where $\Phi'$ is a scalar quantity satisfying the elliptical equation

$$\nabla'^{2}\Phi' = \frac{\nabla' \cdot \boldsymbol{v}'^{*}}{\Delta t'} \ , \tag{4.11}$$

solved by using the fast-Fourier-transforms (FFTs) on the radial directions of the nozzle to decrease the computational cost [117]. Next, the pressure solution results

$$p'^{n+1} = p'^{n} + \Phi' - \frac{\Delta t'}{2Re_{\infty}}\nabla'^{2}\Phi' \ . \tag{4.12}$$

**Viscous numerical instability.** The explicit time discretization of the non-linear non-Newtonian viscous term $G'^{n}_{NN} = \nabla' \cdot \left(2\Delta' \mu'^{n} \mathbf{E}'^{n}\right)/Re_{\infty}$ in Eq. (4.6) even if it avoids the more complex treatment through an implicit Newton-Rhapson method, it implies unfortunately a more severe limitation on the time step than the $CFL$ condition [109, 138]. By taking as example the non-dimensional 3D parabolic Burger's equation

$$\frac{D\psi'}{Dt'} = \frac{1}{Re}\nabla'^{2}\psi' \ , \tag{4.13}$$

where $\psi'$ is a generic scalar variable (e.g. one of the three velocity components), after the explicit discretization of the Laplacian viscous term, a standard stability analysis [109] leads to the following limitation of the time step

$$\frac{\Delta t'}{\Delta s'^{2} Re} < \frac{1}{2d} = \frac{1}{6} \quad \rightarrow \quad \Delta t' < \frac{\Delta s'^{2} Re}{6} \ , \tag{4.14}$$

wherein $d = 3$ indicates the space dimensions of the differential problem, and $\Delta s' = \sqrt[3]{\Delta x' \Delta y' \Delta z'}$ is measure of the local Eulerian grid size.

In case of the Eq. (4.6), the $G'^{n}_{NN}$ term can be written as

$$G'^{n}_{NN} = \frac{1}{Re_\infty}\nabla' \cdot (2\Delta'\mu'^{n}\mathbf{E}'^{n}) = \frac{\Delta'\mu'^{n}}{Re_\infty}\nabla'^{2}\boldsymbol{v}'^{n} + \frac{2\mathbf{E}'^{n}}{Re_\infty}\nabla' (\Delta'\mu'^{n}) \ , \tag{4.15}$$

by resulting in a time step limitation corresponding to

$$\Delta t' < \frac{\Delta s'^{2} Re_\infty}{6\Delta'\mu'^{n}} \ . \tag{4.16}$$

Since the Reynolds numbers are usually very small in bioprinting and the cells have a small dimension compared to the nozzle ones, this condition strongly limits the simulation time step. In addition, the rheological properties of bio-inks may also present a large $\Delta\mu$, further limiting the time step. Fortunately, this is not a global condition, since the $\Delta\mu' \gg 1$ usually only near the nozzle axis where the shear rates are lower, by permitting a larger global time step since for $\Delta\mu' \to 0$ the $G'^{n}_{NN} \to 0$.

## 4.3 Structural modelling of the cell

Due to the intrinsic complexity and multi-scale nature of the cell, its theoretical mechanical modelling is still a research challenge [140]. For anucleate cells, as for red blood cells, a lot of mechanical models are present in literature [141–145], theoretical frameworks including the mechanical contributions of all three main parts of the cell (nucleus, cytoplasm and bi-layer membrane) are still lacking [146].

The measure of cellular mechanical properties is not standardised and the experimental values are specific to the measure technique adopted. The experimental measure methods usually used are single-cell techniques, such as the atomic force microscopy (AFM) [122–125], the micropipette aspiration [46, 147], the compression between two plates [46, 148] the optical tweezer [149], the magnetic twisting cytometry [148] and the microfluidic real-time deformability cytometry [150]. In particular, the AFM is one of the most technique used [123] owing to its great spatial resolution providing very local stiffness values. It involves the application of a spherical or conical nano-indenter over the cell surface, and by comparing the force applied and the corresponding deformation it extracts the cell stiffness. On the other hand, its main drawback is the "bottom-effect" artefact arising from the substrate stiffness which influences the measured value [122, 123]. The cell stiffness measurements performed through the AFM technique usually derive from the fitting of the theoretical model of the axisymmetric bending of the annular thick plate [151] which is a mechanical continuum model. Thus, given the small dimensions of the cell is reasonable to question whether or not the continuum media assumption still applies [46]. By focusing on the plasma membrane, it can be modelled as a continuum media only along the two dimensions describing the surface, since in the third dimension of the thickness it presents a discontinuous structure. Indeed, in order to apply the continuum hypothesis it is necessary that the space scale are large enough to include a sufficient number of molecules such that the molecular fluctuations are small enough. By taking for the membrane molecules a reference mean area of 100 Å[46], since the fluctuations is inversely proportional to the square root of the number of molecules included in the considered range, in order to have

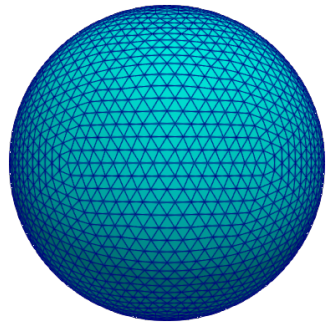

**Figure 4.3:** Discretization of the cell surface.

a fluctuation lower than 1% the continuum scale has to be greater than 0.1 $\mu m$. Therefore, given a cell usually has a mean diameter of $\bar{D} = 5 - 20$ $\mu m$, depending on the numerical discretization adopted the problem scale is intermediate between the continuum and mesoscopic level.

In first analysis, assuming a linear elastic behaviour of the cell for small strains, the representative value of the whole cell stiffness ranges between $E = 0.1 - 100\ kPa$ [122–126]. In particular in a qualitative way, the plasma membrane due to its small thickness presents a small compression stiffness and a negligible bending strength [46]. Its mechanical resistance derives from the underlying spectrin mesh which transfers the mechanical loads to the cytoskeleton which adapts dynamically to the external stimuli. The cytoplasm shows an incompressible behaviour since the water based cytosol occupies about the 70% of the cell volume, and the nucleus presents a higher mechanical strength than the other cell units with a nuclear stiffness higher of 1.4 to 10 times than the cytoplasm [124, 152, 153].

Furthermore, the mechanical cell properties depend not only on the cellular type, but also on the physiological/pathological state of the cell. For example malaria red blood cells present higher stiffness values than the healthy counterparts [154], whereas tumor cells show lower stiffness values which increment their deformability and migration potential raising the metastatic risk [154–156].

In addition to the complexity of the mechanical modelling of the cell, another issue arises from the fluid dynamics modelling of the non-Newtonian polymer in order to evaluate the hydrodynamics loads acting on the cell surface during the extrusion. So, one can see how the FSI modelling of bioprinting is an open research challenge. Indeed, so far only a few models are present in the literature which takes into account the FSI effects during the extrusion bioprinting process [18, 19, 157].

Thus, in order to reduce the complexity of the problem and to limit the issue of the continuum assumption validity mentioned before [46, 117], it has been decided to implement a coarse-graining method [144] which models the whole cell as a discretized 2D surface with null thickness, whose vertices are associated to the mean mechanical properties.

In particular, the surface is discretized through triangular elements as shown in Fig. 4.3 and forming a mechanical spring network based on the interaction potential

approach [117, 158] which derives from the minimum energy concept associating elastic potentials to the network elements [158].

**In-plane stretching stiffness.** Each edge $e$ of the mesh is considered as an elastic spring, and during the cell deformation caused by the external fluid loads, it exhibits an in-plane reaction force. The elastic potential $W_{s,e}$ of the edge associated to the stretching results [117, 158]

$$W_{s,e} = \frac{1}{2} k_s (l_e - l_{0,e})^2 \ , \tag{4.17}$$

where $l_e$ and $l_{e,0}$ are the current and the initial length of the edge respectively, and $k_s$ is the stretching spring constant corresponding to [159]

$$k_s = \frac{Eh \sum_j A_{j,e}}{l_e^2} \ , \tag{4.18}$$

where $E$ and $h$ are the Young's modulus and the thickness of the elastic membrane, and $A_{j,e}$ are the triangle areas sharing the same edge. By differentiating the stretching potential with respect to the position vector $\mathbf{r}_i$ of the two vertices of the edge, the internal stretching force $\mathbf{f}_{s,i}$ turns out

$$\mathbf{f}_{s,int} = -\frac{\partial W_{s,e}}{\partial \mathbf{r}_i} = -\nabla_{\mathbf{r}_i} W_{s,e} \ , \quad i = 1, 2 \ . \tag{4.19}$$

**Out-of-plane bending stiffness.** The elastic spring network can also model the bending stiffness owned by the cytoskeleton and nucleus of the cell. Each pair of triangles sharing the same edge are associated to a bending spring connecting the triangle centroids activated by the variation of the angle $\theta$ between the two triangle normals $\mathbf{n}_1$ and $\mathbf{n}_2$. The bending potential results [117, 141, 144, 160]

$$W_{b,e} = k_b \left[1 - \cos(\theta - \theta_0)\right] \ , \tag{4.20}$$

where $\theta_0$ is the free-stress angle between $\mathbf{n}_1$ and $\mathbf{n}_2$. The bending spring constant $k_b$ is based on the bending model reported in [145, 161] and due to the triangular discretization turns out [144]

$$k_b = D \frac{2}{\sqrt{3}} \ , \qquad D = \frac{Eh^3}{12(1 - \nu^2)} \ , \tag{4.21}$$

where $D$ and $\nu$ are to the flexural rigidity [162] and the Poisson coefficient of the elastic surface respectively. By differentiating the bending potential with respect to the position vector $\mathbf{r}_i$ of the four vertices composing the two adjacent triangles, the internal bending force results

$$\mathbf{f}_{b,int} = -\frac{\partial W_{b,e}}{\partial \mathbf{r}_i} = -\nabla_{\mathbf{r}_i} W_{b,e} \ , \quad i = 1, \ldots, 4 \ . \tag{4.22}$$

Regarding the thickness value $h$ of the stretching spring constant $k_s$ in Eq. (4.18) and the bending spring constant $k_b$ in Eq. (4.21), it is important to note that since the structural model adopted reduces the whole mechanical properties of the cell on the surface, its value it is not related to the plasma membrane (which is

around 10 $nm$), but it has to be calibrated in order to represent the mean whole mechanical stiffness of the cell obtained from experimental measures, as reported in next chapter of results.

**Volume conservation constraint.** Since the presence of the water based cytosol in the cytoplasm, the cell behaves like an incompressible material [141, 144, 146, 152]. Thus, a possible volume potential associated to the volume variation of the cell may be written as [158]

$$W_v = \frac{1}{2} k_v \left( \frac{V - V_0}{V_0} \right) V_0 \ , \tag{4.23}$$

where $V$ and $V_0$ are the current and the initial cell volume respectively, and $k_v$ is the volume conservation constant. The corresponding internal volume force results

$$\mathbf{f}_{v,int} = -\frac{\partial W_v}{\partial \mathbf{r}_i} = -\nabla_{\mathbf{r}_i} W_{v,l} \ , \quad i = 1, 2, 3 \ . \tag{4.24}$$

where $\mathbf{r}_i$ is the position vector of the three base vertices of each tetrahedron composing the cell. By tuning the $k_v$ constant with a value large enough, it is possible to guarantee the cell volume conservation during the simulation.

**Area conservation constraint.** The cell membrane may presents also a surface area conservation due to near-incompressibility property of the phospholipid bilayer [46, 163]. Even if this property is in doubt in literature since the exo- and endocytosis membrane processes [164, 165]. A possible area potential may be written as [158]

$$W_a = \frac{1}{2} k_a \left( \frac{A - A_0}{A_0} \right) A_0 \ , \tag{4.25}$$

where $A$ and $A_0$ are the current and the initial surface area of the cell respectively, and $k_a$ is the area conservation constant. The corresponding internal area force results

$$\mathbf{f}_{a,int} = -\frac{\partial W_a}{\partial \mathbf{r}_i} = -\nabla_{\mathbf{r}_i} W_{a,l} \ , \quad i = 1, 2, 3 \ . \tag{4.26}$$

where $\mathbf{r}_i$ is the position vector of the three base vertices of each tetrahedron composing the cell. By tuning the $k_a$ constant with a value large enough it is possible to guarantee the cell area conservation during the simulation.

## 4.4 Loose coupling of fluid-structure interaction

As described in the introduction paragraph, since the faster dynamics of cell structure and to avoid the re-meshing issue of the CFD grid due to cell displacements and high cell density values of the bio-ink, a loosely-coupled FSI algorithm has been implemented with a sub-iterative structural solver and based on the immersed boundary (IB) method.

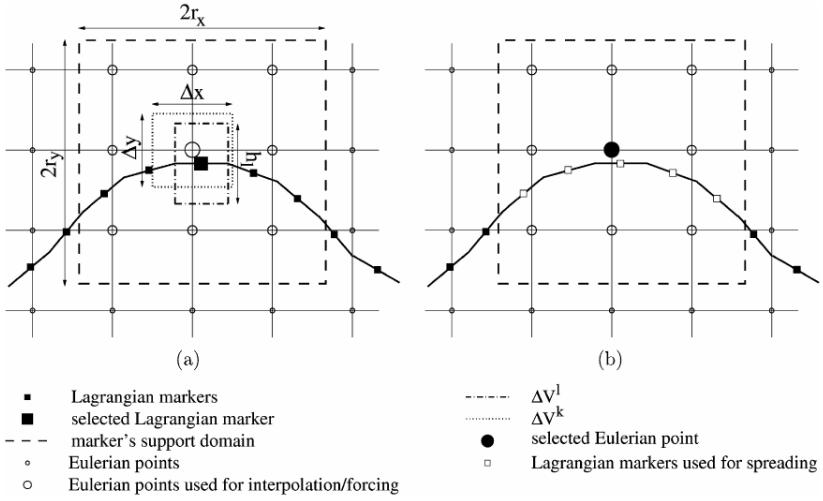


**Figure 4.4:** The schematic domain of the MLS technique [117].

In particular, the numerical treatment of the cell surface immersed in the fluid is based on a direct-forcing IB method with a moving-least-squares (MLS) reconstruction technique [117, 129] used to apply the coupling no-slip velocity boundary condition between the two media. The MLS reconstruction mitigates the possible numerical instabilities deriving from spurious hydrodynamics oscillations caused by the motion and deformation of the structure in the fluid [117, 129, 166, 167].

**The moving-least-squares (MLS) reconstruction technique.** Once the intermediate velocity solution $\hat{\boldsymbol{v}}$ has been computed from the Eq. (4.7), the IB direct-forcing is applied to impose the no-slip boundary condition between the fluid and the walls of the nozzle and cells getting so the updated solution $\boldsymbol{v}^*$

$$\boldsymbol{v}^* = \hat{\boldsymbol{v}} + (\mathbf{f}_{IB,nozzle} + \mathbf{f}_{IB,cells})\,\Delta t \ , \tag{4.27}$$

where $\mathbf{f}_{IB,nozzle}$ is the IB force in Eq. (4.9), $\mathbf{f}_{IB,cells}$ is the IB force based on the MLS reconstruction technique and $\Delta t$ is the simulation time step of the fluid.

In particular, the cell surface is discretized through a triangular mesh and to each triangle centroid is associated a Lagrangian marker as schematically shown in Fig. 4.4 [117]. The no-slip boundary condition between the cell surface and the fluid is applied on the Eulerian location corresponding to the Lagrangian marker position through the $\mathbf{F}_{IB,cells}$ IB force and then is transferred back to the neighbouring Eulerian nodes of the fluid grid through $\mathbf{f}_{IB,cells}$. To compute the $\mathbf{f}_{IB,cells}$ force, the first step is to individuate the closest fluid node to the triangle marker and to associate it a CFD cubic support domain with a range in the three space direction $r_i = 1.5\Delta x_i$, with $\Delta x_i$ corresponding to the CFD grid steps which involves $N_e = 27$ fluid nodes in the 3D space. Then, the projection of the intermediate fluid solution $\hat{\mathbf{V}}$ at each Lagrangian marker is approximated by component as [117]

$$\hat{V}_i(\mathbf{x}) = \mathbf{p}^T(\mathbf{x})\mathbf{a}(\mathbf{x}) \ , \tag{4.28}$$

where $\mathbf{p}^T(\mathbf{x}) = [1\ x\ y\ z]$ is the linear basis function vector approximating the solution, and $\mathbf{x}$ is the position vector of the marker. $\mathbf{a}(\mathbf{x})$ is the vector of coefficients resulting from the minimization of the L2-norm $J$ defined as

$$J = \sum_{k=1}^{N_e} W(\mathbf{x} - \mathbf{x}^k) \left[\mathbf{p}^T(\mathbf{x}^k)\mathbf{a}(\mathbf{x}) - \hat{v}_i^k\right]^2 \ , \tag{4.29}$$

where the suffix $k$ indicates the variable is evaluated at Eulerian point $k$ constituting the CFD support domain with $N_e$ nodes, and $W(\mathbf{x} - \mathbf{x}^k)$ is an exponential weight function defined as

$$W(\mathbf{x} - \mathbf{x}^k) = \begin{cases} e^{-(r_k/\varepsilon)^2} & r_k \leq 1 \\ 0 & r_k = 0 \end{cases} \ , \tag{4.30}$$

where $\varepsilon = 0.3$ and $r_k = |\mathbf{x} - \mathbf{x}^k|/r_i$.

The minimization leads to solving the linear system

$$\mathbf{A}(\mathbf{x})\mathbf{a}(\mathbf{x}) = \mathbf{B}(\mathbf{x})\hat{\boldsymbol{v}}^k \tag{4.31}$$

with the matrices $\mathbf{A}$ and $\mathbf{B}$ depend on the weight function $W(\mathbf{x} - \mathbf{x}^k)$ [117]. Thus, the intermediate fluid solution $\hat{\mathbf{V}}$ at the Lagrangian marker can be rewritten as

$$\hat{V}_i(\mathbf{x}) = \boldsymbol{\phi}^T\hat{\boldsymbol{v}}_i = \sum_{k=1}^{N_e} = \phi_k^l(\mathbf{x})\hat{v}_i^k \ , \tag{4.32}$$

where $\boldsymbol{\phi}^T = \mathbf{p}^T(\mathbf{x})\mathbf{A}^{-1}(\mathbf{x})\mathbf{B}(\mathbf{x})$ is the transfer operator between the intermediate fluid solution $\hat{v}_i$ and its projection $\hat{V}_i^k$ at the Lagrangian marker $l$ position containing the shape functions values $\phi_k^l$. Once $\hat{V}_i$ is known, it is possible to apply the first coupling condition of the no-slip velocity between the two media

$$\boldsymbol{v}(t)_f = \boldsymbol{v}_s(t) \ , \quad \text{on} \quad \Gamma_{int.}(t) \tag{4.33}$$

where $\boldsymbol{v}_f$ and $\boldsymbol{v}_s$ are the velocities of the fluid and solid material points lying on the interface surface $\Gamma_i(t)$.

In particular, the application of the direct IB force $F_{i,IB,cells}$ to the position in the fluid grid corresponding to each Lagrangian marker location

$$F_{i,IB,cells} = \frac{V_i^{bc} - \hat{V}_i}{\Delta t} \ , \tag{4.34}$$

ensures the no-slip velocity between the fluid and cells, where $V_i^{bc}$ is the $i$-th component of the desired boundary condition to be imposed, namely the velocity of the Lagrangian marker of the previous time step. Then, the IB force $F_{i,IB,cells}$ is transferred back to the associated Eulerian nodes $k$ resulting by component as

$$f_{i,IB,cells}^k = \sum_{l=1}^{N_l} c_l \phi_k^l F_{i,IB,cells}^l \ , \tag{4.35}$$

where $l$ and $N_l$ indicating the Lagrangian markers associated with the $k$ Eulerian node, i.e. whose Lagrangian points having the $k$ Eulerian node in the own

support fluid domain. The $c_l$ scaling coefficients are determined by imposing the conservation of the volumetric IB force during the transfer

$$\sum_{k=1}^{N_{e,tot}} f_i^k \Delta V^k = \sum_{l=1}^{N_{l,tot}} F_i^l \Delta V^l \ , \tag{4.36}$$

where $N_{e,tot}$ are the total Eulerian nodes involved in the IB forcing, $\Delta V^k = \prod_{i=1}^{3} \Delta x_i^k$ the corresponding Eulerian grid volume, $N_{l,tot}$ the total Lagrangian markers of the immersed body, $\Delta V^l = A^l h^l$ the volume associated to each marker with $A^l$ the triangle area and $h^l = \sum_{k=1}^{N_e} \phi_k^l (\sum_{i=1}^{3} \Delta x_i^k)/3$ the average mesh size at the marker location. An important note about the MLS technique is that in order to have an accurate and stable solution it requires a Lagrangian spacing of the immersed cell about 0.7 the Eulerian one [117].

**Evaluation of hydrodynamics forces on the cell surface.** After the application of the first coupling condition of the no-slip velocity between the cell and the fluid is through the Eq. (4.34), it is possible to apply the second coupling condition of stress equivalence on the interface surface

$$\boldsymbol{\sigma}_f(t) \cdot \mathbf{n}_f(t) + \boldsymbol{\sigma}_s(t) \cdot \mathbf{n}_s(t) = \mathbf{0} \ , \quad \text{on} \quad \Gamma_{int.}(t) \tag{4.37}$$

where $\boldsymbol{\sigma}_f$ and $\boldsymbol{\sigma}_s$, and $\mathbf{n}_f$ and $\mathbf{n}_s$, are the stress tensors and the outward normals of the fluid and solid material points respectively lying on the interface surface $\Gamma_{int.}(t)$. In particular, by nothing that $\mathbf{n}_f = -\mathbf{n}_s$ on $\Gamma_{int.}$ the coupling condition turns out in ensuring $\boldsymbol{\sigma}_f = \boldsymbol{\sigma}_s$ on the cell surface.

Thus, the external hydrodynamic viscous and pressure forces acting on the cell surface are evaluated on the Lagrangian marker location, resulting

$$\mathbf{f}_{ext}^l = \left( \boldsymbol{\tau}^l \cdot \mathbf{n}^l - p^l \mathbf{n}^l \right) A^l \ , \tag{4.38}$$

where $\boldsymbol{\tau}^l$ and $p^l$ are the deviatoric stress tensor and the internal pressure of the fluid and $\mathbf{n}^l$ is the marker normal. Their values are computed through the use of a probe normal to the marker at a distance $h^l$ from the triangle surface [117] and by adopting the MLS reconstruction technique. Therefore, by projecting the momentum balance Eq. (2.15) along $\mathbf{n}^l$, the pressure $p^l$ turns out [129, 168]

$$p^l = p^e - \frac{\partial p}{\partial n} h^l = p^e + h^l \frac{D\boldsymbol{v}}{Dt} \cdot \mathbf{n}^l \ , \tag{4.39}$$

where $p^e$ is the pressure evaluated at the probe point. The deviatoric tensor $\boldsymbol{\tau}^l$ is assumed equal to the $\boldsymbol{\tau}^e$ evaluated at the probe location, namely assuming a linear variation of the velocity near the cell surface, coherently to the MLS technique adopted. Then, the external forces of each triangle are transferred to the three composing vertices dividing them by three.

**The proximity model between cell-to-wall and cell-to-cell.** Regarding the modelling of the collision dynamics between the cells and the nozzle wall and the cells themselves, the discretized Eq. (4.6) of motion theoretically takes into account the repulsive pressure and viscous forces during the approaching phase, since it is

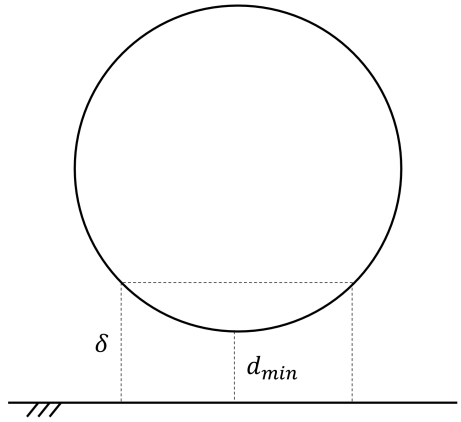


**Figure 4.5:** Schematic representation of a cell approaching to the nozzle wall.

resolved through a direct numerical simulation. But due to the discretization of the problem a contact model, or more properly a proximity model is needed. Indeed, when the gap $d$ between the two bodies decreases below the $2\Delta$ value, with $\Delta$ corresponding to the local average space grid step, the MLS reconstruction technique starts to interfere and to increase the solution error, since it involves a support domain in the three space directions of 27 Eulerian nodes [117, 132]. Therefore, assuming that the lubrification forces are large enough during the collision, and with the aim to prevent the numerical overlap during the simulation between the cells and the nozzle and the cells themselves, a proximity model based on that one described in Section 4.1 has been implemented. More specifically, it activates when the gap $d$ goes below a threshold value $\delta$ and provides a repulsive pressure distribution based on the model in Eq. (4.3) for a spherical particle approaching a wall in a creeping flow reported in [130, 131], namely based on the lubrification approximation [169].

In particular, when a vertex of the cell approaches a distance $d$ equal to or lower than $d \leq \delta = 3\Delta$ to the other body (the nozzle wall or another cell) as shown in Fig. 4.5 (usually depending on the case $\delta$ may vary from $\Delta$ to $3\Delta$ [133, 167]), a linear repulsive pressure distribution is activated on the portion of the cell surface in proximity, and which ranges between a null value, corresponding to a vertex distance $d = \delta$ from the other body, and a maximum value $p_{rep,max}$, corresponding to the minimum vertex distance from the other body. Considering the case of a cell-to-wall collision, the $p_{rep,max}$ results [130, 131]

$$p_{rep,max} = \frac{3\mu V_{cell,\perp} D_{cell}}{2d_{min}^2} \ , \tag{4.40}$$

where $\mu$ is the fluid viscosity, $V_{cell,\perp}$ and $D_{cell}$ are the transversal component of the velocity to the wall and the diameter of the cell respectively, and $d_{min}$ is the minimum distance of the cell vertex closest to the wall. Since the FSI solver used computes the Navier-Stokes equations in non-dimensional form with reference variables a diameter $D$ of the nozzle outlet, an extrusion velocity $V_0$, a pressure

$p_0 = \rho V_0^2$ and an infinity-shear rate viscosity $\mu_\infty$ of the bio-ink, the corresponding non-dimensional $p'_{rep,max}$ results

$$p'_{rep,max} = \frac{3}{Re_\infty} V'_{cell,\perp} \frac{D'_{cell}}{2} \frac{1}{(d'_{min})^2} \ , \tag{4.41}$$

with $Re_\infty = \rho V_0 D/\mu_\infty$. Thus, the linear distribution of the repulsive pressure over the cell vertices in proximity to the other body implemented turns out

$$p'_{rep}(d') = p'_{rep,max} \frac{\delta' - d'}{\delta' - d'_{min}} \ . \tag{4.42}$$

In the cell-to-cell approaching case, the scheme implemented for the repulsive pressure is analogous to the cell-to-wall case, but with the corresponding maximum pressure value divided of a factor 4 and corresponding to [169]

$$p'_{rep,max,cell2cell} = \frac{3}{4Re_\infty} V'_{cell2cell,\perp} \frac{D'_{cell}}{2} \frac{1}{\left(d'_{min,cell2cell}\right)^2} \ , \tag{4.43}$$

where in this case $d'_{min,cell2cell}$ is the minimum relative distance between the two cells and $V'_{cell2cell,\perp}$ is the non-dimensional component of the cell-to-cell relative velocity transversal to the unit vector connecting the two cell barycentres $\mathbf{r}'_{cell2cell}$, namely

$$V'_{cell2cell,\perp} = |(\boldsymbol{v}'_{cell,1} - \boldsymbol{v}'_{cell,2}) \cdot \mathbf{r}'_{cell2cell}| \ . \tag{4.44}$$

The linear distribution of the repulsive pressure over the cell vertices in proximity to the other cell results

$$p'_{rep,cell2cell}(d'_{cell2cell}) = p'_{rep,max,cell2cell} \frac{\delta' - d'_{cell2cell}}{\delta' - d'_{min,cell2cell}} \ , \tag{4.45}$$

where $d'_{cell2cell}$ is the relative distance between the vertex of a cell and the surface of the other cell.

Next, since the repulsive pressure scales as $1/Re_\infty$ and the Reynolds number are small in bioprinting, it may happen that its value could increase excessively causing the divergence of the numerical solution. Therefore it has been setted a limit value to the maximum repulsive pressure evaluated through the Eq. (4.41) by considering a $d'_{min} = \Delta/D$.

Then, the corresponding repulsive force acting on the cell vertex has been modelled as a force directed towards the cell centre which reads

$$\mathbf{f}'_{rep} = -\frac{\mathbf{r}'_i - \mathbf{r}'_B}{|\mathbf{r}'_i - \mathbf{r}'_B|} p'_{rep} A'_i \ , \tag{4.46}$$

where $\mathbf{r}'_i$ and $\mathbf{r}'_B$ are the position vectors of the vertex and of the cell barycentre respectively, and $A'_i$ is the area associated to each vertex which corresponds to the sum of the triangle areas sharing the same vertex divided by three.

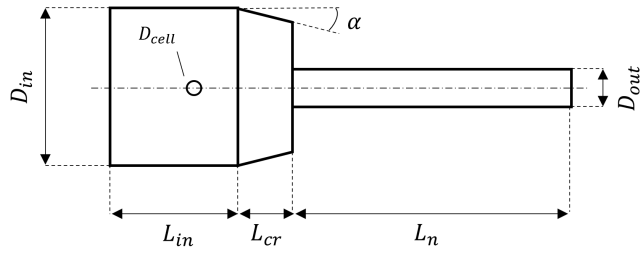


**Figure 4.6:** Geometry of the FSI simulations [49, 62].

**Time integration algorithm.** Once the sum of the external forces $\mathbf{f}_{ext,i}$ in Eqs. (4.38), the internal forces $\mathbf{f}_{int,i}$ in Eqs. (4.19),(4.22),(4.24),(4.26) and the repulsive forces $\mathbf{f}_{rep,i}$ in Eqs. (4.42), (4.45) have been evaluated for each vertex composing the cell surface, the structural dynamics of the cell motion and deformation have been computed through an explicit Adam-Bashforth 2-steps method with a second order accuracy [109], resulting

$$\ddot{\mathbf{r}}_i^n = \left(\mathbf{f}_{ext,i}^n + \mathbf{f}_{int,i}^n + \mathbf{f}_{rep,i}^n\right)/m_i \ , \tag{4.47a}$$

$$\dot{\mathbf{r}}_i^{n+1} = \dot{\mathbf{r}}_i^n + \left(\frac{3}{2}\ddot{\mathbf{r}}_i^n - \frac{1}{2}\ddot{\mathbf{r}}_i^{n-1}\right)\Delta t_s \ , \tag{4.47b}$$

$$\mathbf{r}_i^{n+1} = \mathbf{r}_i^n + \left(\frac{3}{2}\dot{\mathbf{r}}_i^n - \frac{1}{2}\dot{\mathbf{r}}_i^{n-1}\right)\Delta t_s \ , \tag{4.47c}$$

where the apex $n$ indicates the time step reference, $\ddot{\mathbf{r}}_i$, $\dot{\mathbf{r}}_i$ and $\mathbf{r}_i$ are the acceleration, velocity and position vector of each vertex respectively, $m_i = m_{cell}/N_v$ is the mass of each vertex derived from the division of the cell mass $m_{cell}$ by the $N_n$ vertices composing the cell surface, and $\Delta t_s = \Delta t_f/N_{sub}$ is the sub-iterative time step of the structure composed of $N_{sub}$ sub-iterations with respect to the fluid time step $\Delta t$.

## 4.5 Simulation parameters & boundary conditions

**Table 4.1:** Geometry parameters of the nozzle.

| $D_{out}$ | $D_{in}$ | $D_{cell}$ | $L_{in}$ | $L_{cr}$ | $L_n$ | $\alpha$ |
|---|---|---|---|---|---|---|
| $100 - 330\,\mu m$ | $800\,\mu m$ | $30\,\mu m$ | $552\,\mu m$ | $138\,\mu m$ | $1.3 - 3.0\,mm$ | $36°$ |

**Geometry.** The simulations have been carried out on a standard nozzle geometry used in extrusion bioprinting [49, 62] reported in Fig. 4.6 and with dimensions given

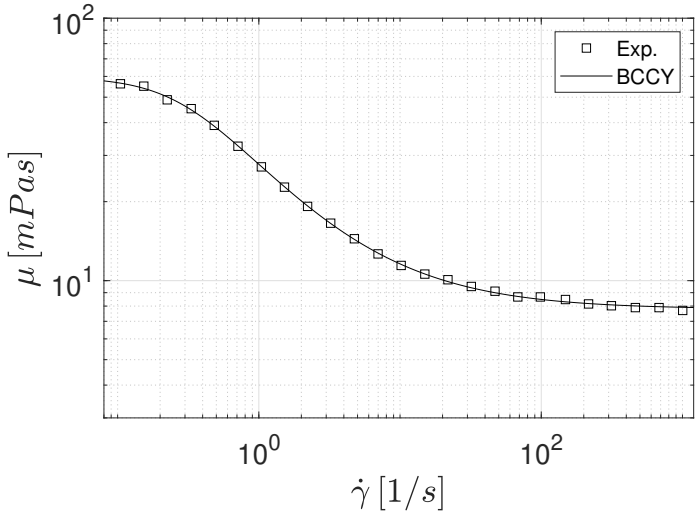


**Figure 4.7:** Experimental data of the hydrogel simulated from Colosi *et al.*[103] and the corresponding fitting obtained through the BCCY model in Eq. (2.21).

in Table 4.1. The nozzle is mainly composed by three parts: an entrance region with an inlet diameter $D_{in} = 800\,\mu m$, a convergent region characterized by a conical angle $\alpha = 36°$, and a sharp cross section reduction from the cartridge connection to needle, the latter is characterized by a straight cylindrical shape and an outlet diameter ranging between $D_{out} = 100 - 330\,\mu m$, determining the resolution of the bioprinting process. Due to the computational cost, the needle length $L_n$ has been varied depending on the memory availability. The cells have been modelled as spheres with a diameter $D_{cell} = 30\mu m$ [45, 127]. The uniform structured CFD mesh has been varied from 181x181x380 to 181x181x704 nodes accordingly to the $L_n$ value, and the cell mesh has been designed with almost equilateral triangles adopting a Lagrangian marker spacing about 0.7 the Eulerian grid size [117] (see Section 4.4).

**Table 4.2:** Rheological parameters of the BCCY model used to fit viscosity data in Fig. 4.7.

| $\mu_0$ | $\mu_\infty$ | $\lambda$ | $n$ | $a$ | $R^2$ |
|---|---|---|---|---|---|
| $59.8\,mPas$ | $7.8\,mPas$ | $3.42\,s$ | 0.259 | 1.76 | 99.8 % |

**Fluid parameters.** The fluid properties have been derived from viscosity data of a low-viscosity hydrogel of gelatin methacryloyl (GelMA) present in literature [103] and reported in Fig. (4.7). They have been fitted with the BCCY model in Eq. (2.21) through the minimization of the mean absolute percentage error (MAPE) [170]. The best-fitting values are reported in Table 4.2 with the coefficient

of determination $R^2$ [170]. It has been assumed as reference a hydrogel density $\rho = 10^3\ kg/m^3$, that for an outlet diameter $D = 100\,\mu m$ and an extrusion velocity $V_0 = 20\,mm/s$ results in Reynolds number ranging between

$$Re_\infty = \frac{\rho V_0 D}{\mu_\infty} = 2.56 \cdot 10^{-1} \qquad \text{and} \qquad Re_0 = \frac{\rho V_0 D}{\mu_0} = 3.34 \cdot 10^{-2}\ . \tag{4.48}$$

Since the low Reynolds numbers the non-dimensional fluid time step has been increased at the limit of the viscous numerical instability (see Section 4.2) corresponding to $\Delta t' = \Delta t D/V_0 = 10^{-4}$.

**Structure parameters.** For the cell it has been chosen a Young's modulus $E = 5\,kPa$ corresponding to an intermediate value of those reported in literature ranging between $0.1\,kPa - 100\,kPa$ [122–126], and with a near incompressible behaviour with a Poisson coefficient $\nu = 0.48$. The volume conservation constant has been setted as $k_v = 1000$ by performing numerical tests and measuring the volume percentage variation.

The thickness value $h$ included in the stretching and bending spring constants $k_s$ and $k_b$ (see Section (4.3)) has been chosen by performing a calibration procedure based on simulations of a single cell immersed in a Newtonian Couette shear flow, which compares the net strain of the cell $\Delta\epsilon$ corresponding to different capillarity numbers $Ca$ defined as

$$\Delta\epsilon = \frac{d_{max} - D_{cell}}{D_{cell}}, \qquad Ca = \frac{\mu\dot{\gamma}}{G}, \tag{4.49}$$

where $d_{max}$ is the maximum elongation between two vertices, $\mu$ is the viscosity of the Newtonian fluid, $\dot{\gamma}$ is the constant shear rate between the bottom and top planes of the Couette flow and $G = E/[2(1+\nu)])$ is the elastic shear modulus of the cell.

**Table 4.3:** Net cell strains $\Delta\epsilon$ corresponding to different $Ca$ numbers reported in [157].

| $Ca$ | $\Delta\epsilon$ |
|---|---|
| 0.1 | 13.8 % |
| 0.2 | 27.7 % |
| 0.3 | 40.9 % |

The data of the net strain-capillarity number relationship have been extrapolated from the comparison between the model developed by Müller *et al.*[157] and the analytical 3D calculations carried out by Gao *et al.*[171] in the linear elastic range (see Fig. 8b in [157]) and are reported in Table 4.3.

In particular, the same simulation setup of Müller *et al.*have been replicated in the non-dimensional framework of the finite difference solver employed as shown in Fig. 4.8, by ensuring the dimensional similarity between the two numerical frameworks through the imposition of the same $Re$ and $Ca$ numbers.

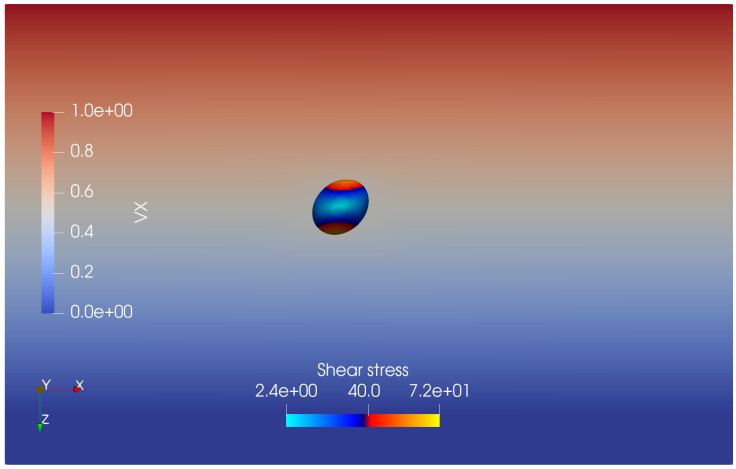


**Figure 4.8:** Simulation of a single cell in a Couette shear flow performed to calibrate the thickness $h$ value. The tangential velocity $v_x$ and cell shear stress are in non-dimensional form.

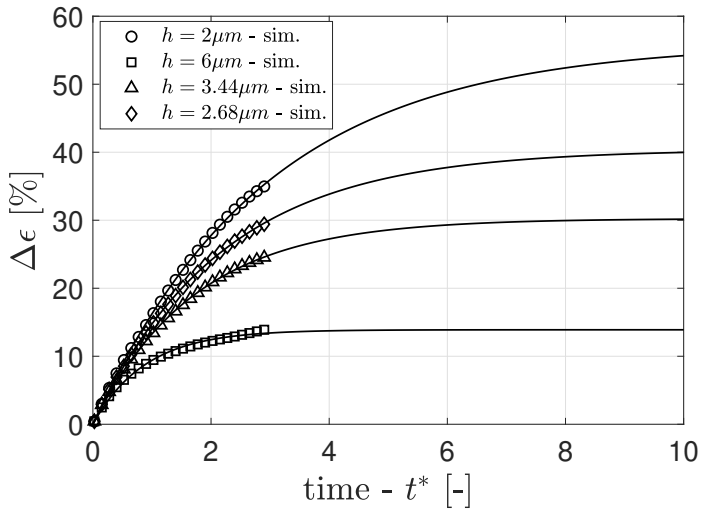


**Figure 4.9:** Exponential fitting of the net strain $\Delta\epsilon$ in function of the thickness $h$ for $Ca = 0.3$.

Thus, once the fluid and the cell elastic parameters have been setted, given a $Ca$ number the $h$ value has been calibrated in order to reproduce the same net strain value $\Delta\epsilon$ listed in Table 4.3. To limit the computational cost, the simulation results of the net strain value in function of the non-dimensional time have been fitted through the exponential equation

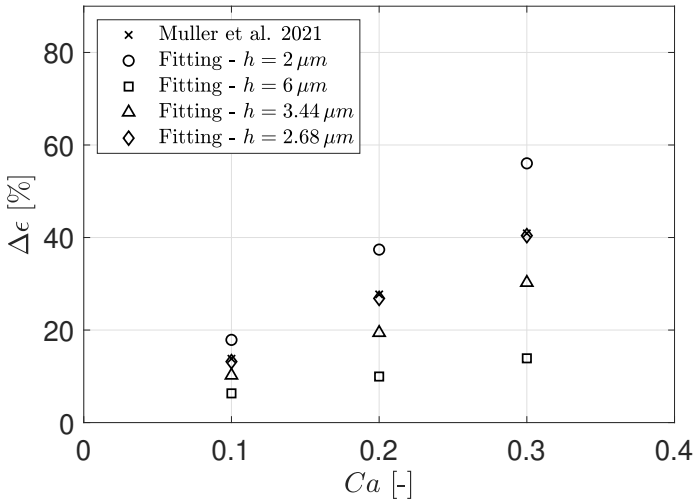


**Figure 4.10:** Calibration procedure of the thickness value $h$ in function of $Ca$ compared with the results reported in [157]

.

$$\Delta\epsilon\,(t) = \Delta\epsilon\,(1 - e^{-t/\tau}), \tag{4.50}$$

where $\tau$ is the characteristic time constant of the cell deformation. The fitting is reported in Fig. 4.9.

Results of the calibration procedure are shown in Fig. 4.10, leading to the choice of the optimal thickness value $h = 2.68\,\mu m$. Regarding the cell density of the bio-ink, it has been immersed 163 cells in the inlet and in the convergent region of the nozzle, resulting in cell density equal to $0.663 \cdot 10^6\,cells/ml$.

**Table 4.4:** Structural parameters of cells.

| $E$ | $\nu$ | $h$ | $k_v$ | $n_{cells}$ | bio-ink cell density |
|---|---|---|---|---|---|
| $5000\,Pa$ | 0.48 | $2.68\,\mu m$ | 1000 | 163 | $0.663 \cdot 10^6\,cells/ml$ |

The structure parameters are summarized in Table 4.4, and the structure time step has been setted as $5 \cdot 10^7$ in order to have 200 sub-iterations of the structural solver for each fluid time step.

**Boundary conditions.** For the differential problem of the fluid, it has been applied an axial velocity profile $\boldsymbol{v} = [0\ 0\ v_z]^T$ at the inlet for a power law fluid in order to guarantee the desired velocity extrusion at the needle outlet and corresponding to

$$v_z(r) = V_0 \left(\frac{R_{out}}{R_{in}}\right)^2 \left(\frac{3n+1}{n+1}\right) \left[1 - \left(\frac{r}{R_{in}}\right)^{\frac{n+1}{n}}\right], \tag{4.51}$$

where $V_0$ is the extrusion velocity, $R_{in}$ and $R_{out}$ the inlet and outlet radius respectively and $n$ is the power law index. At the outlet a convective velocity condition is imposed

$$\frac{\partial \boldsymbol{v}}{\partial t} + V_0 \left(\nabla \boldsymbol{v} \cdot \mathbf{n}\right) = \mathbf{0} \ , \tag{4.52}$$

where $\mathbf{n}$ is the normal vector at the outlet. Along the radial directions $x$ and $y$, a periodic boundary condition is applied such to use the fast-Fourier-transform (FFT) and a no-slip boundary condition at the nozzle wall through the IB method (see Section 4.2). For the structure, a no-slip boundary condition between the cells and the fluid is applied through the MLS reconstruction technique (see Section 4.4). A null value of the pressure in the axial position at the outlet is also enforced.

Regarding the initial condition at the time $t_0$, a null initial condition for the velocity and pressure of the fluid, and for the velocity and acceleration of the structure are applied. The initial positions of the cells have been setted with an uniform distribution in the inlet and convergent region of the nozzle, by modelling a perfectly mixed bio-ink.

## 4.6 Results

The following section presents the results of the FSI simulations carried out to analyse the interaction phenomena occurring between the polymeric fluid and cells within the bio-ink during the extrusion. First, the Section 4.6.1 investigates the flow dynamics of the fluid without cells, and then the dynamics and kinematics of a single flowing cell. In particular, it analyses the mean and the maximum shear stresses acting on the cell surface defined as

$$\tau^{mean}_{shear,cell} = \frac{1}{S}\int_S \left|(\boldsymbol{\sigma}\cdot\mathbf{n})\cdot\mathbf{t}\right| dS \ , \qquad \tau^{max}_{shear,cell} = \max_S(\left|(\boldsymbol{\sigma}\cdot\mathbf{n})\cdot\mathbf{t}\right|) \ , \tag{4.53}$$

where $\boldsymbol{\sigma} = -p\mathbf{I} + \boldsymbol{\tau}$ is the stress tensor of the fluid evaluated on the cell surface $S$ through the MLS technique, and $\mathbf{n}$ and $\mathbf{t}$ are the normal and tangential unit vectors of each triangular areola composing the cell mesh. Moreover, the FSI solution is compared with the classic estimate of shear stresses computed by using the Eq. (3.5) [49] and reading

$$\tau^{classic}_{cell} = \frac{\Delta p}{2L} r_{cell,id} = \frac{\Delta p}{2L} 0.6 R_{out} \ , \tag{4.54}$$

where the pressure drop $\Delta p/L$ is evaluated from the fluid simulation. It assumes a homogeneous fluid and an ideal radial equilibrium position $r_{cell,id} = 0.6\, R_{out}$ based on the particle transport analysis in Stokes flows (see Section 2.5).

Then, the Section 4.6.2 statistically analyses the load history of a cell population corresponding to bio-ink densities typically used in extrusion bioprinting. In particular, it also evaluates the powers of the external pressure and viscous forces of the fluid acting on the cell surface and reading

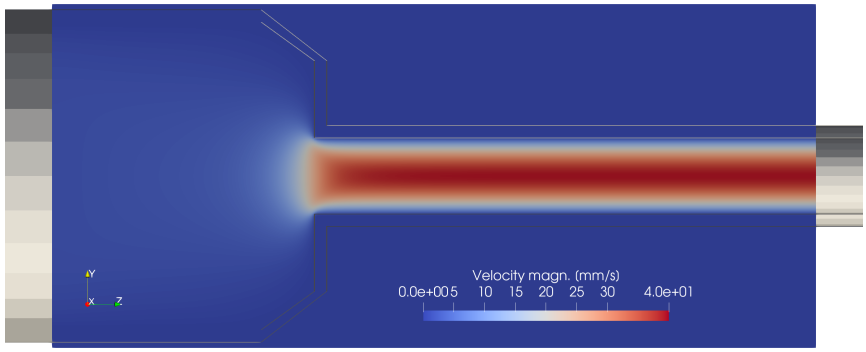


**Figure 4.11:** Velocity magnitude of the fluid.

$$P_{press,cell} = \int_S -p\mathbf{n} \cdot \dot{\mathbf{r}} dS \qquad P_{visc,cell} = \int_S (\boldsymbol{\tau} \cdot \mathbf{n}) \cdot \dot{\mathbf{r}} dS \ , \tag{4.55a}$$

$$P_{tot,cell} = P_{press,cell} - P_{visc,cell} \tag{4.55b}$$

where $\dot{\mathbf{r}}$ is the velocity vector of the cell surface point and $P_{tot,cell}$ the total external power.

Finally, the Section 4.6.3 presents the results of the parametric analyses performed by varying the outlet diameter and the flow conditions, with respect to those of the previous section taken as reference case.

### 4.6.1 Single cell extrusion

In order to better understand the phenomena taking place during the extrusion, the case of single cell extrusion has been considered. The initial position of the cell is close to the nozzle axis at the beginning of the convergent region, with a nozzle outlet diameter $D_{out} = 200\,\mu m$.

**Fluid dynamics of the bio-ink.** Starting from the fluid results, Fig. 4.11 shows that due to the cross section reduction $D_{out}/D_{in} = 4$ between the inlet and the outlet of the nozzle, the fluid velocity magnitude increases in the needle part, by reaching a maximum value $V_{max} = 2V_0 = 40\,mm/s$. This outcome indicates a parabolic velocity profile and thus the reaching of the second Newtonian plateau at viscosity $\mu_\infty$ of the fluid rheological characteristic shown in Fig. 4.7. Indeed, by looking to the viscosity field and deviatoric stress tensor magnitude field shown in Fig. 4.12 one notes as at the inlet zone due to the lower shear rates there is a viscosity zone around $20\,mPas$ in the power law region of the BCCY model with negligible deviatoric stress values; next, in the convergent region there is a viscosity

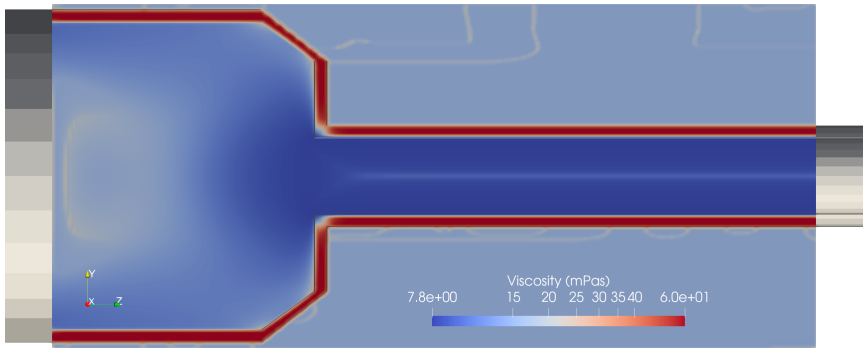


**(a)** Viscosity field of the fluid.

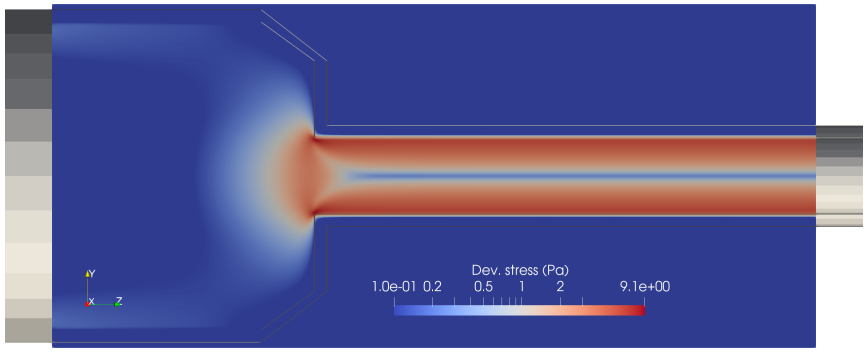


**(b)** Stress field of fluid.

**Figure 4.12:** Viscosity (a) and deviatoric stress (b) fields of the fluid in logarithmic scale.

decrement and a stress increment with peak values nearby the sharp corners, and then, a linear deviatoric stress distribution in the needle zone accordingly to the Eq. (3.5)

$$\tau \simeq \tau_{zr}(r) = -\frac{\Delta p}{2L} r \ . \tag{4.56}$$

**Cell dynamics.** Analysing the cell dynamics during the extrusion, Fig. 4.13 reports the axial velocity of the cell and its percentage radial position referred to the nozzle outlet radius $R_{out}$. To ease results interpretation, the axial coordinates

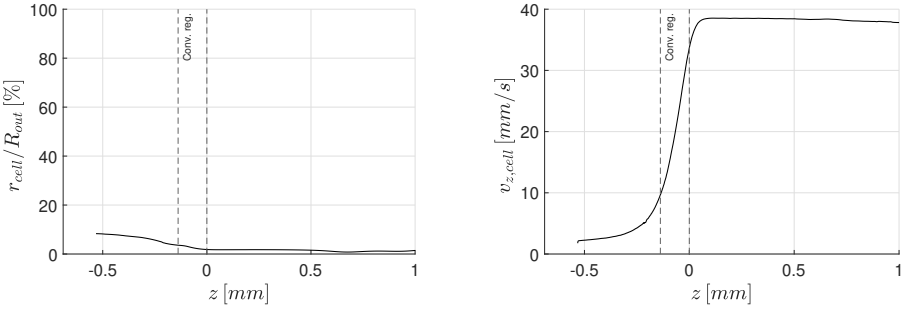


**(a)** Radial cell position. **(b)** Axial cell velocity.

**Figure 4.13:** Percentage radial position $r_{cell}$ and (a) axial velocity $v_{z,cell}$ (b) of the cell as a function of the nozzle axial coordinate $z$.

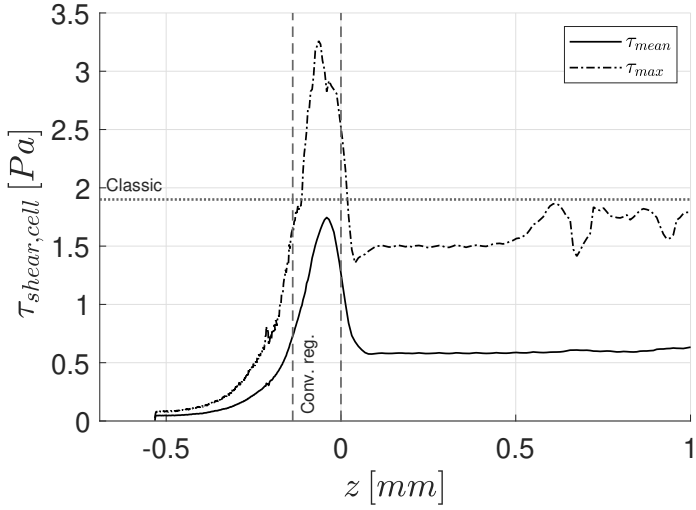


**Figure 4.14:** Mean and maximum shear stress of the cell.

have been centred at the end of the convergent region, as highlighted through the two vertical dashed lines. The cell starts with a null velocity and then accelerates rapidly in the convergent region to reach a quasi-stationary value of $38\,mm/s$ around the maximum fluid velocity $V_{max} = 40\,mm/s$ along the axis reported in Fig. 4.11. During the extrusion, the cell remains close to the axis region under the 1% of the outlet radius (Fig. 4.13(a)), but it presents a lower velocity value since its inertia.

Moving to the stress experienced by the cell, Fig. 4.14 shows the mean and the maximum shear stress defined in Eq. (4.53). The cell presents a peak mean shear stress in the convergent region and then a quasi-stationary value about $0.59\,Pa$. The maximum shear stress shows significantly higher values, increasing by $(\tau^{max}_{shear,cell} - \tau^{mean}_{shear,cell})/\tau^{mean}_{shear,cell} \simeq +159\%$. Moreover, the classic estimate

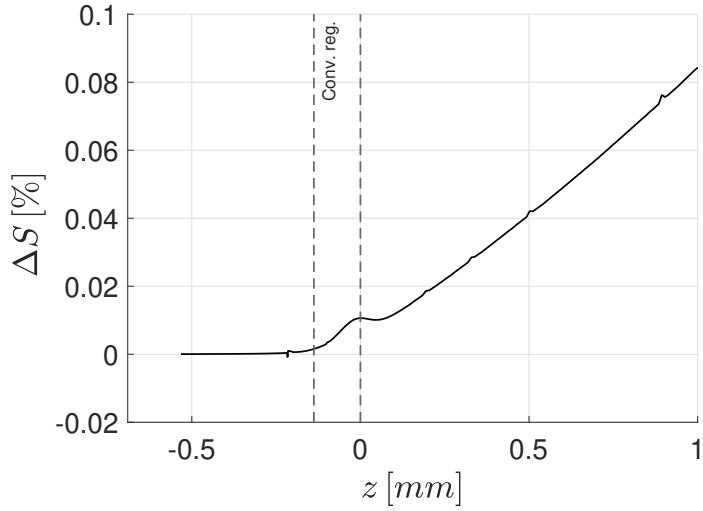


**Figure 4.15:** Surface percentage variation of the cell.

of shear stress computed by using the Eq. (4.54) is reported. It is remarkable how the classic solution overestimates the mean and the maximum shear stress and is unable to follow the trend of the FSI solution in the convergent region.

**Cell kinematics.** Analysing the cell deformation, the surface percentage variation $\Delta S = (S - S_0)/S$ is reported in Fig. 4.15, with $S_0$ corresponding to the initial surface. The deformation shows low values, with an increment in the convergent region, followed by an linear trend in the needle, which recalls the beginning region of the exponential trend of the Couette shear flow in Fig. 4.9. Indeed, in the needle part, the fluid flow is a shear flow, contrarily to the convergent region where is characterized by an extensional regime [74]. The low deformation value could be also qualitatively predicted by the evaluation of the capillarity number. In the needle part the flow is Newtonian and the wall shear rate results from Eq. (3.25) (which is also valid for cylindrical flows) $\dot{\gamma}_{wall} = 4V_0/R_{out} = 800\,1/s$ resulting in a $Ca_{needle} = \mu_\infty \dot{\gamma}_{wall}/G = 3.74 \cdot 10^{-3}$. Thus, from the analysis of the capillarity number-net strain relationship in Fig. 4.10 one can derives that the deformations are almost negligible in this case. Therefore, since the surface variation is in the order of 0.1 %, the cell deformations have been neglected in the following results.

### 4.6.2 Multiple cells extrusion

**Initial position influence.** A first study with multiple cells immersed in the bio-ink regards the analysis of the initial position influence on the cell dynamics during the extrusion process. In particular, four cells with the same initial position coordinates $z'_{0,cell} = 5.2/D$ and $y'_{0,cell} = 0$, and different $x'_{0,cell}$ coordinates starting from $x'_{0,cell\,1} = 0$ to $x'_{0,cell\,4} = 3$ with unit step have been simulated. In Fig. 4.16 it is possible to note how higher $x_{0,cell}$ positions (namely closer to the nozzle

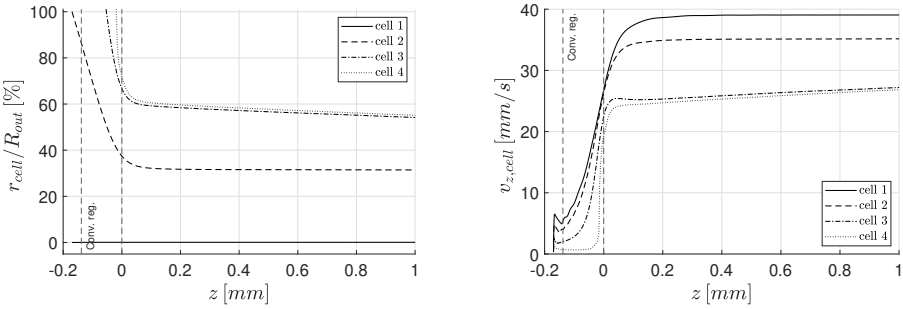


**(a)** Radial cell position. **(b)** Axial cell velocity.

**Figure 4.16:** Percentage radial position $r_{cell}$ (a) and axial velocity $v_{z,cell}$ (b) of the four cells considered as a function of the nozzle axial coordinate $z$.

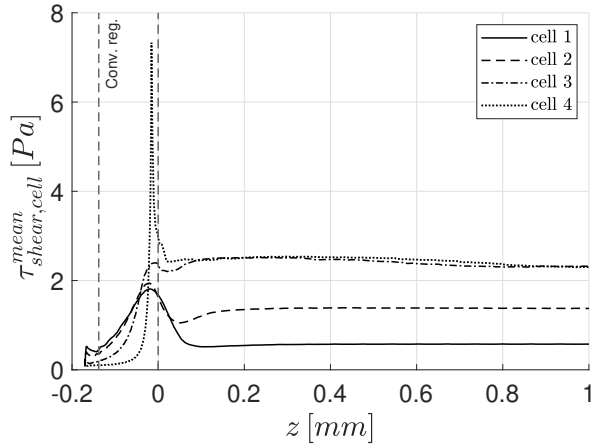


**Figure 4.17:** Mean shear stress of the four cells considered.

wall) correspond to a greater radial equilibrium position in the needle, and thus to lower velocities determined by the flow streamlines. Next, the analysis of the mean shear stress in Fig. 4.17 shows how the most external cell (cell 4) presents a high peak in the convergent region around $7.33\,Pa$ and corresponding to a percentage increment in respect to the cell 1 around $\Delta\tau^{mean}_{shear,cell\,1,4}/\tau^{mean}_{shear,cell\,1} \simeq +307\%$. This stress peak is due to the higher flow resistance encountered by the cell 4, which during the simulation has been blocked at the needle entrance, causing a local flow section reduction, and thus a fluid stress increment nearby the cell. While in the needle part, the outer cells present a higher shear stress, accordingly to the trend of Eq. (4.56).

**Reference case.** Next, it has been performed a more realistic simulation by considering 163 cells immersed in the fluid and corresponding to a bio-ink cell

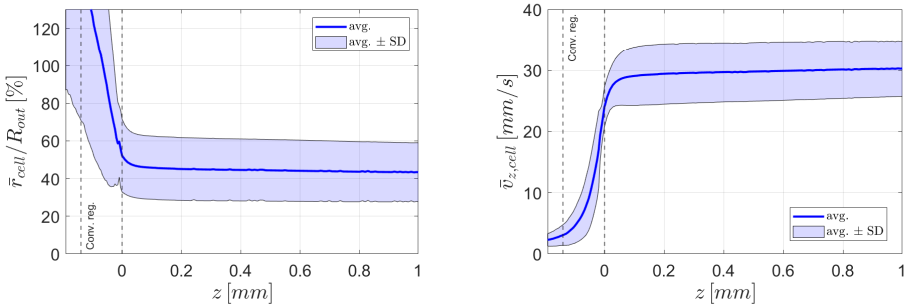


**(a)** Radial position. **(b)** Axial velocity.

**Figure 4.18:** Percentage radial position $\bar{r}_{cell}$ (a) and axial velocity $\bar{v}_{z,cell}$ (b) of the cell population as a function of the nozzle axial coordinate $z$, with the average value (continuous line) and the standard deviation (shaded area).

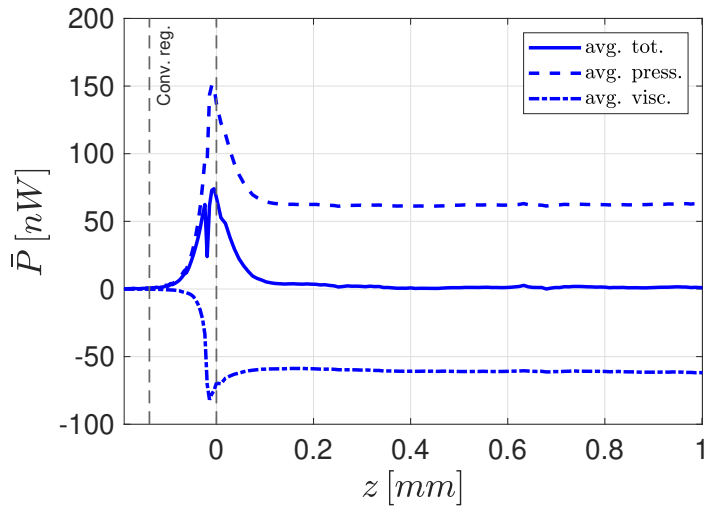


**Figure 4.19:** External powers acting on the surface of the cell population.

density of $0.663 \cdot 10^6\, cells/ml$ as reported in Table 4.4. In order to take into account the load histories of all cells, a statistical analysis on the cell population has been carried out. The average values of the quantities of interest have been marked as $\bar{f}$, and reported together the corresponding standard deviation values (SD).

In Fig. 4.18(a) the radial equilibrium position of the cell population has been reported reaching a value of 44% of the nozzle outlet radius. The velocity plot in Fig. 4.18(b) shows an a rapid acceleration in the convergent region and a stationary value of $30\, mm/s$, coherently to the radial position.

Then, in Fig. 4.19 it has been calculated the powers of the external forces

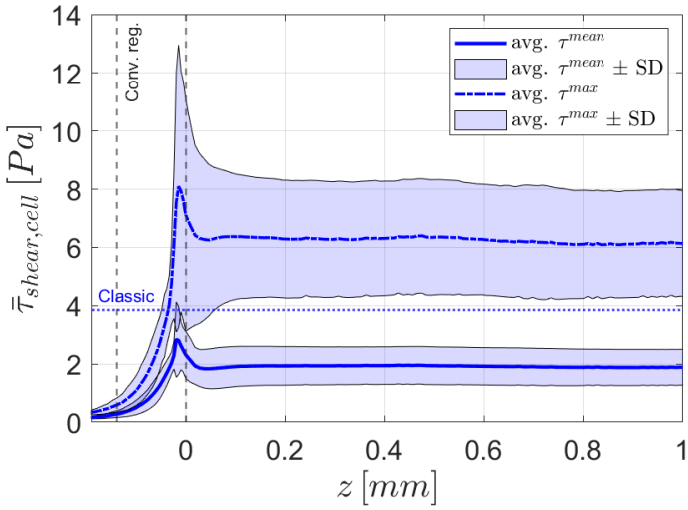


**Figure 4.20:** Mean and maximum shear stress of the cell population.

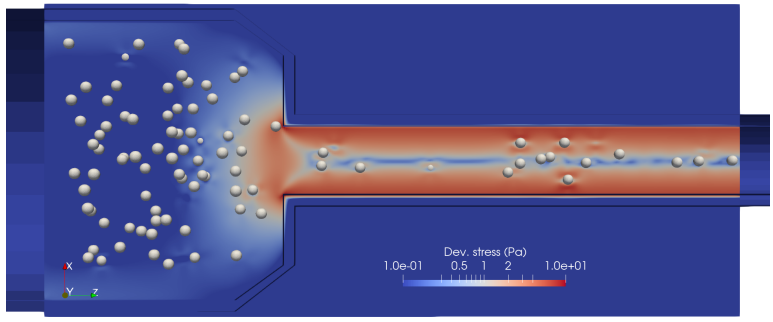


**Figure 4.21:** Deviatoric stress field $\tau$ of the fluid.

of the fluid acting computed through Eqs. (4.55). One can notes how nearby the convergent region the total power is positive accordingly to the acceleration reported in Fig. 4.18(b), and then rapidly vanishes in the needle wherein the viscous forces balance the pressure ones.

Next, the shear stress analysis reported in Fig. 4.20 shows for the mean shear stress a SD value about the 45% of the average in the peak of the convergent region and around the 33% in the needle zone. While the maximum shear stress notably presents an increment of the average value around +189% in the convergent region and +228% in the needle than the mean value counterparts, with a SD value about +204 % larger. This increment is due to the local flow section reduction caused

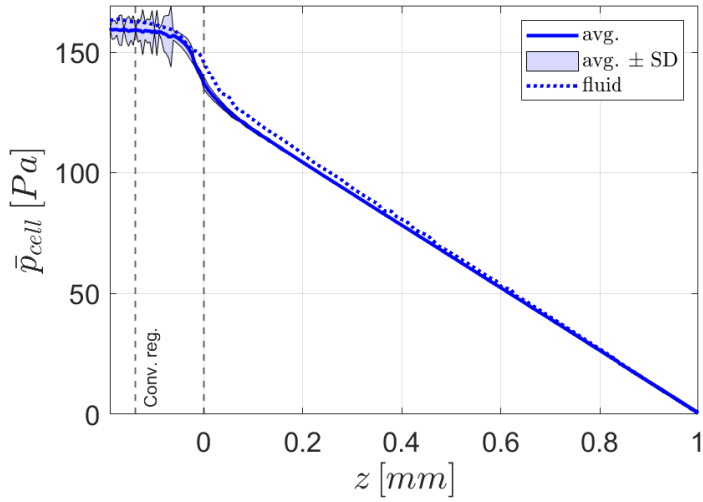


**Figure 4.22:** Pressure of the cell population and of the fluid along the nozzle axis.

| | $\bar{r}_{cell}/R_{out}$ | $\bar{v}_{z,cell}$ | $\bar{\tau}^{mean}_{shear,cell}$ | $\bar{\tau}^{max}_{shear,cell}$ | $\bar{\tau}^{max}_{shear,cell}/\bar{\tau}^{mean}_{shear,cell}$ |
|---|---|---|---|---|---|
| avg. | 44 % | $29.9\,mm/s$ | $1.91\,Pa$ | $6.26\,Pa$ | 328 % |
| SD/avg. | 37 % | 16 % | 50 % | 44 % | - |

**Table 4.5:** statistical analysis results of the cell population at $z = 0.6\,mm$.

by the presence of cells which modify the local stress field as shown in Fig. 4.21. As for the single cell case, the classic solution overestimates the shear stress with a value of $3.84\,Pa$ greater than 98 % of the mean stress, since in this case the effective radial equilibrium position computed through the FSI approach is lower and corresponding to about 44 % of the needle radius.

In Fig. 4.22 the pressure acting on the cell surface is reported and compared to the fluid solution along the axis. The cell population presents an almost negligible SD with exception in the initial nozzle part, and it nearly overlaps to the fluid solution. Assuming a needle length of 12 $mm$, the extrapolation of the pressure drop along all the nozzle gives a value of about $1.6\,kPa$. While the pressure drop in the convergent region is about 20 $Pa$, and therefore can generally be neglected.

As a summary, the main results of the interest variables are reported in Table 4.5.

### 4.6.3 Parametric analyses

For the reference case simulation reported in the previous paragraph the computational cost in terms of simulation time has been around 522 hours (on a workstation equipped with Intel Xeon W-1290 10 cores, 3.2-5.2 GHz, 64 GB RAM), due to the limitation on time step described in Section 4.2. Therefore, to allow for parametric studies, simulations have been performed by adopting a scaling procedure based on

| $D_{out}$ | $\bar{r}_{cell}/R_{out}$ | $\bar{v}_{z,cell}$ | $\bar{\tau}^{mean}_{shear,cell}$ | $\bar{\tau}^{max}_{shear,cell}$ | $\bar{\tau}^{max}_{shear,cell}/\bar{\tau}^{mean}_{shear,cell}$ |
|---|---|---|---|---|---|
| $100\,\mu m$ | 27 % | $33.5\,mm/s$ | $2.88\,Pa$ | $11.4\,Pa$ | 396 % |
| $200\,\mu m$ | 44 % | $29.9\,mm/s$ | $1.91\,Pa$ | $6.26\,Pa$ | 328 % |
| $330\,\mu m$ | 49 % | $27.5\,mm/s$ | $1.26\,Pa$ | $3.71\,Pa$ | 294 % |

**Table 4.6:** Average values of the parametric statistical analysis on the needle diameter at $z = 0.6\,mm$.

Reynolds' number equivalence concepts (see Appendix A). Such procedure allowed to reduce the simulation time down to 41 hours with a loss of accuracy of 6%.

**Needle diameter influence.** A first parametric analysis has been performed in Fig. 4.23 by simulating an extrusion with a needle diameter $D_{out}$ of $100\,\mu m$, $200\,\mu m$ and $330\,\mu m$, and comparing it with the reference case $D_{out} = 200\,\mu m$.

By starting form the smallest to the largest outlet diameter, the cells tend to reach a greater radial equilibrium position, with a $\bar{r}_{cell,100\,\mu m}/R_{out} = 27\,\%$, $\bar{r}_{cell,200\,\mu m}/R_{out} = 44\,\%$ and $\bar{r}_{cell,330\,\mu m}/R_{out} = 49\,\%$ respectively, and thus a larger axial velocity. This trend can be explained with the decrease of the reduced cell size $D_{cell,red.} = D_{cell}/D_{out}$, which reduces from 30 % to 9.1 % determining cells to get closer to the theoretical value $\bar{r}_{cell,id} = 0.6R_{out}$ which is referred to particles with a negligible diameter compared to the channel dimension [89].

Analysing the shear stress in Fig. 4.24, one can note how for the same extrusion velocity $V_0$, a larger diameter leads to lower mean shear stress, even if the cell population moves to a larger percentage radial position where the stress are higher. This is due to the inverse quadratic dependence of pressure drop on needle diameter $\Delta p/L = 32\mu_\infty \bar{V}/D^2_{out}$, which if inserted in the momentum balance Eq. (3.5) results

$$\bar{\tau}_{cell} = \frac{\Delta p}{2L}\bar{r}_{cell} = \frac{16\mu_\infty V_0}{D^2_{out}}\bar{r}_{cell}\ . \tag{4.57}$$

The classic estimates (accordingly to the Eq. (4.54)) are also reported in Fig. 4.24, confirming that these overestimate the effective mean shear stresses and underestimate the maximum shear stress shown in Fig. 4.25. The detailed average values of the stress analysis together the radial equilibrium position and axial velocity analysis as a function of needle diameter are reported in Table 4.6 and in Fig. 4.26. In particular, the Figure 4.26 highlights the greater decrement of the maximum shear stress in respect to the mean value for increasing needle diameters.

**Power law regime in the needle.** Next, it has been analysed the influence of the flow regime on cell stresses, leaving the same printing settings and geometries of the reference case simulation, and varying the fluid rheological properties in order to to obtain a power law regime in the needle. This procedure resulted in choosing the rheological parameters of the BCCY model reported in Table 4.7. In particular the $\lambda$ parameter has been decreased until to obtain a value for the $\dot{\gamma}_0$ and $\dot{\gamma}_\infty$ of the BCCY model in Eq. (2.23) almost coinciding with the shear rates of the printing window $\dot{\gamma}^{print}_{min} = 10.4\,1/s$ and $\dot{\gamma}^{print}_{max} = 1128\,1/s$. The corresponding

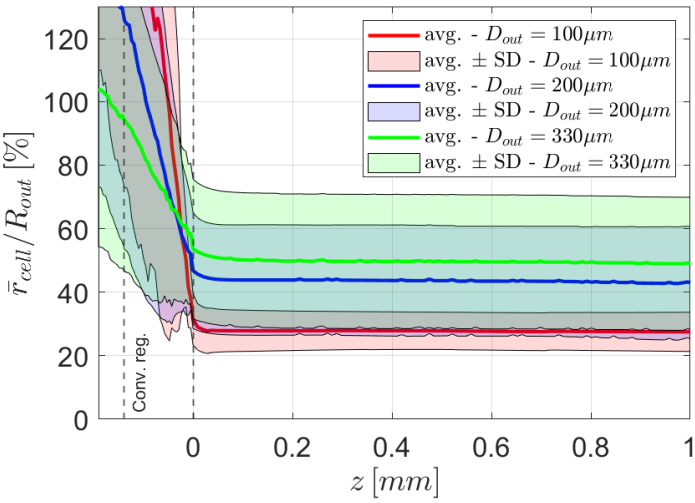


**(a)** Radial position.

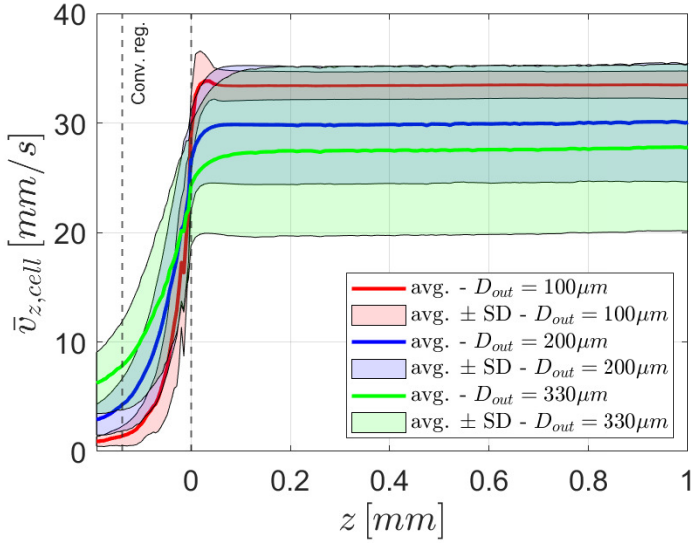


**(b)** Axial velocity.

**Figure 4.23:** Parametric analysis on the needle diameter $D_{out}$. Percentage radial position $\bar{r}_{cell}$ (a) and axial velocity $\bar{v}_{z,cell}$ (b) of the cell population, with the average value (continuous line) and the standard deviation (shaded area).

rheological curve is shown in Fig. 4.27 together the shear rates of the printing window represented by the vertical dashed lines.

As a proof, the shear rate field is plotted in Fig. 4.28, with legend limits

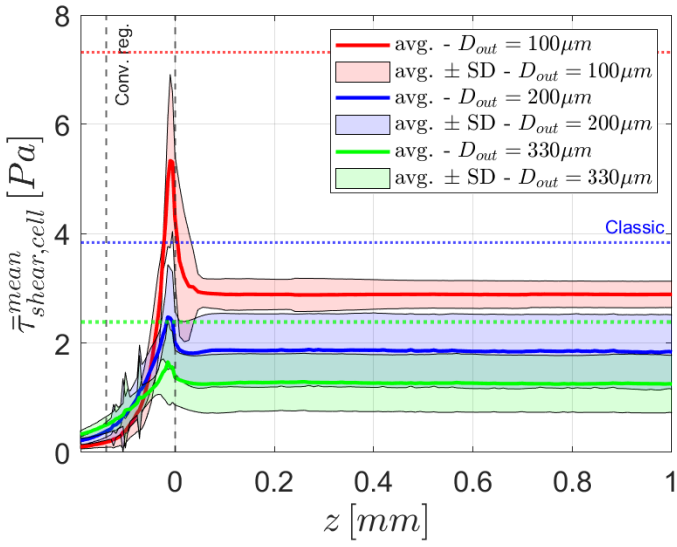


**Figure 4.24:** Mean shear stress of the cell population of the parametric analysis on the needle diameter $D_{out}$. The dotted lines are the classic estimates computed through the Eq. (4.54).

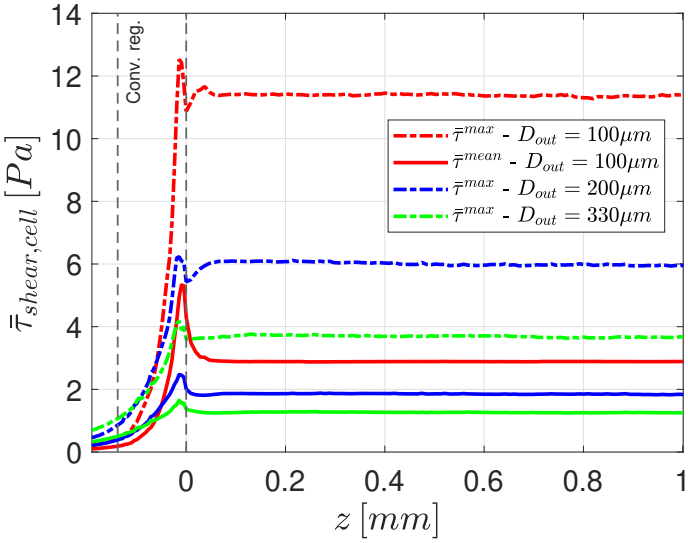


**Figure 4.25:** Maximum shear stress of the cell population of the parametric analysis on the needle diameter $D_{out}$.

corresponding to $\dot{\gamma}^{print}_{min}$ and $\dot{\gamma}^{print}_{max}$. One can note as only at the corners of the convergent region the fluid exceeds the $\dot{\gamma}^{print}_{max}$ value, indicating a full power law

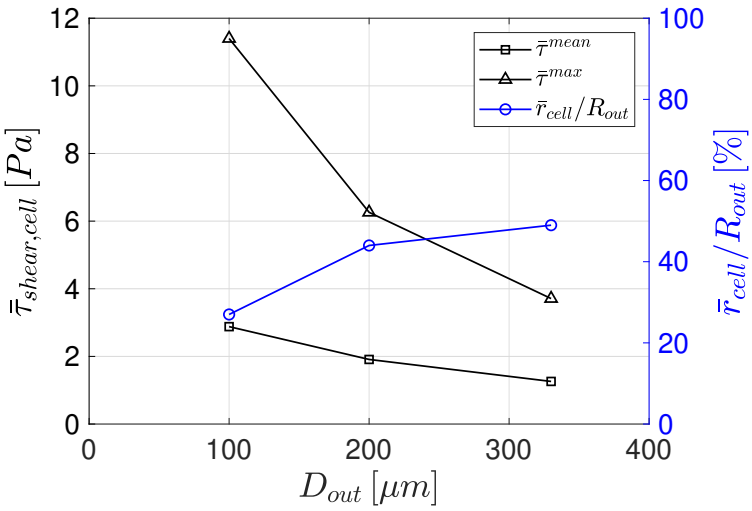


**Figure 4.26:** Mean and maximum shear stress (black, left axis) and percentage radial position $\bar{r}_{cell}/R_{out}$ (blue, right axis) of the cell population as a function of the needle diameter $D_{out}$ reported in Table 4.6.

**Table 4.7:** Rheological parameters of the BCCY model plotted in Fig. 4.27 and used to simulate a fluid with a power law regime in the needle.

| $\mu_0$ | $\mu_\infty$ | $\lambda$ | $n$ | $a$ |
|---|---|---|---|---|
| $59.8\,mPas$ | $7.8\,mPas$ | $5.7 \cdot 10^{-2}\,s$ | 0.259 | 1.76 |

flow in the needle region.

Comparing the results of the cell population with the reference case, Fig. 4.29 shows that the radial position and the axial velocity show almost the same value. On the other hand, the mean shear stress in Fig. 4.30 presents in the needle an average value of $3.44\,Pa$ about 80 % greater than the reference case, since the current fluid has a greater $\dot{\gamma}_0 = 1/\lambda$ value (see Fig. 4.27) which increases the hydraulic resistance of the flow and thus a the dispensing pressure.

**Extrusion velocity.** A parametric analysis by varying the extrusion velocity from $10\,mm/s$ to $40\,mm/s$ and comparing the results with the reference case (with an extrusion velocity of $20\,mm/s$) has been performed. As shown in Fig. 4.31, the simulation with a faster velocity of $40\,mm/s$ presents a radial equilibrium position similar to the reference case. While in the slowest extrusion the cells move closer to the nozzle wall. Next, analysing the mean shear stress in Fig. 4.32 it is possible to note a quasi-linear trend in the needle part between the three cases accordingly to the relationship between the shear stress and extrusion velocity in Eq. (4.57); the values at $z = 0.6\,mm$ compared to the reference case have been reported in the second column of the Table 4.8. While in the convergent region, the faster extrusion case shows a maximum peak value of $6.7\,Pa$ about +171 % larger than

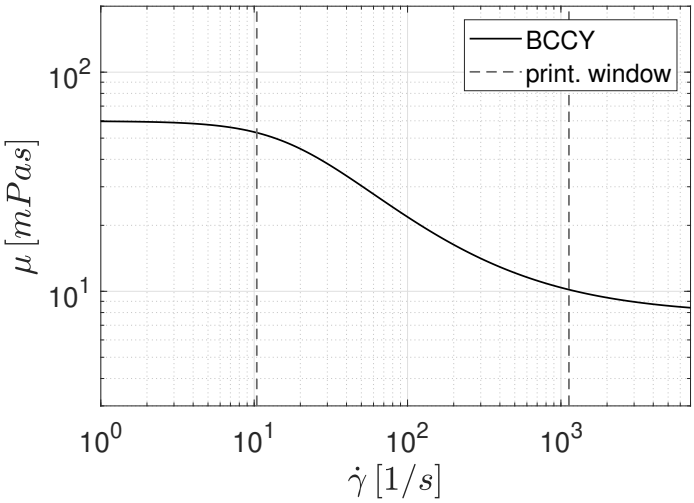


**Figure 4.27:** Rheological curve of the BCCY model in Eq. (2.21) (solid line), and shear rate values of the printing window (dashed lines) for the fluid in the power law regime simulated in the parametric analysis.

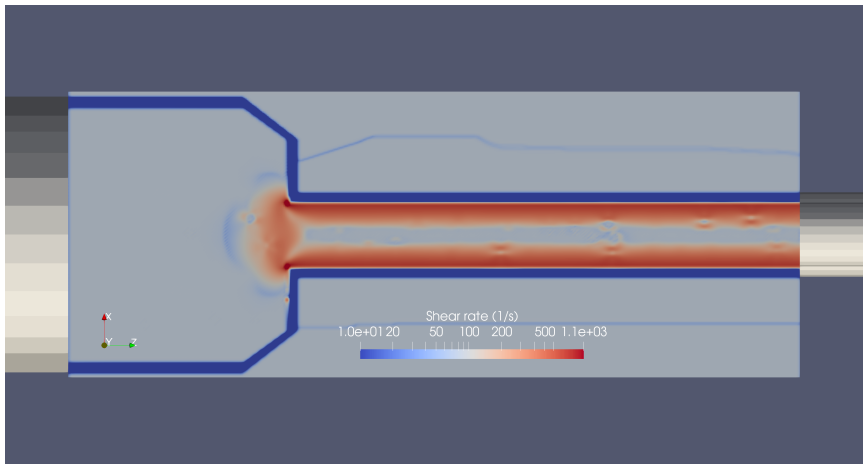


**Figure 4.28:** Shear rate field obtained in the needle for the fluid in the power law regime (see Fig. 4.27).

the reference case.

As a summary, in Table 4.8 the average values of the percentage radial position and of the mean shear stress compared to the reference case have been reported for all the parametric analysis with the same outlet diameter $D_{out} = 200\mu m$. The radial position shows a small deviation from the reference case within $\pm 5\,\%$, indicating that the fluid regime has, in our simulated cases, a minor influence on cell position within the nozzle. Finally, the Figure 4.33 shows the maximum and mean

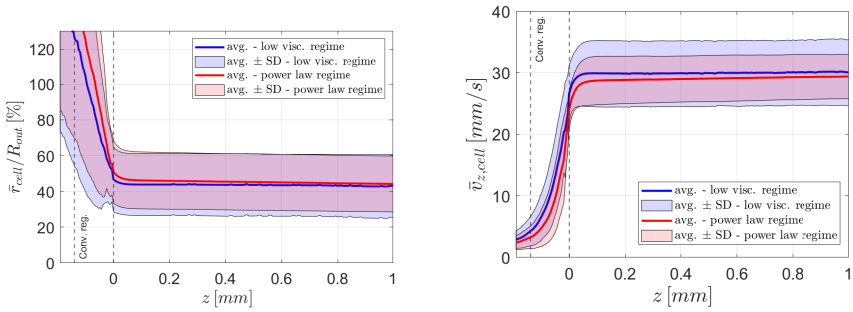


**(a)** Radial position. **(b)** Axial velocity.

**Figure 4.29:** Percentage radial position $\bar{r}_{cell}$ (a) and axial velocity $\bar{v}_{z,cell}$ (b) of the cell population, in the parametric analysis of the needle power law regime, with the average value (continuous line) and the standard deviation (shaded area).

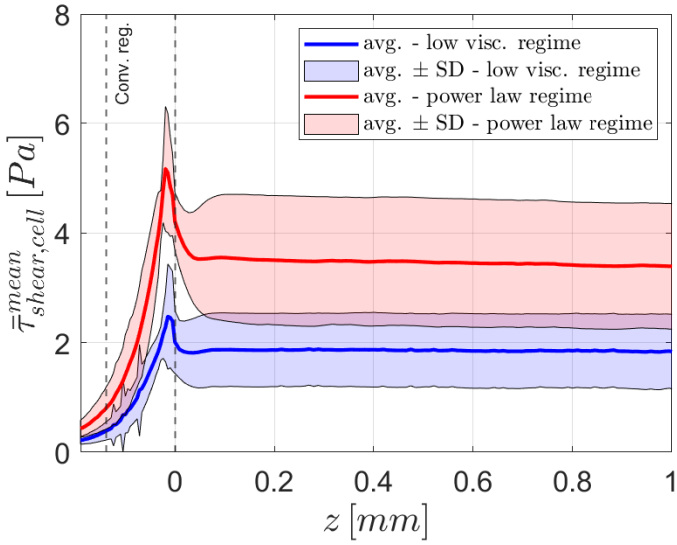


**Figure 4.30:** Mean shear stress of the cell population in the parametric analysis of the needle power law regime.

shear stresses together the radial position of the cell population in the needle at $z = 0.6\,mm$ for increasing extrusion velocities. It is noteworthy that the maximum shear stress presents a greater slope than the mean value of about +380 %.

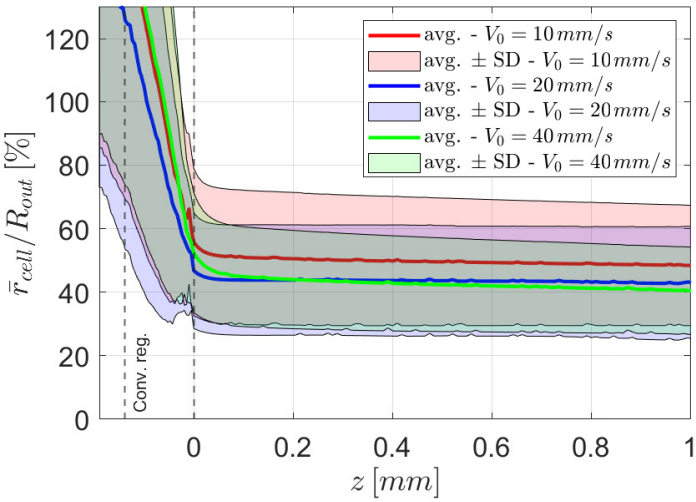


**Figure 4.31:** Percentage radial position $\bar{r}_{cell}$ of the cell population, in the parametric analysis on the extrusion velocity, with the average value (continuous line) and the standard deviation (shaded area).

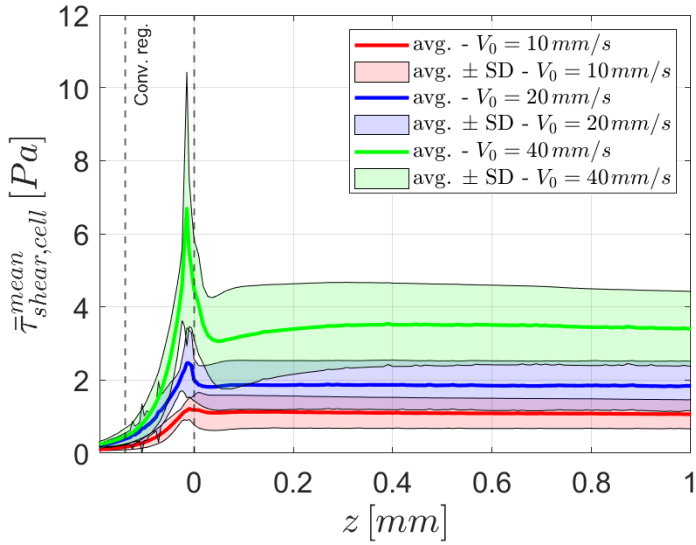


**Figure 4.32:** Mean shear stress of the cell population in the parametric analysis on the extrusion velocity.

| case | $\bar{r}_{cell}/R_{out}$ | $\bar{\tau}^{mean}_{shear,cell}/\bar{\tau}^{mean}_{shear,cell,20\,mm/s}$ |
|---|---|---|
| $V_0 = 10\,mm/s$ | 49 % | 59% |
| $V_0 = 20\,mm/s$ | 44 % | 100 % |
| $V_0 = 40\,mm/s$ | 42 % | 190 % |
| needle pow. law flow | 45 % | 180 % |

**Table 4.8:** Average values of the parametric statistical analyses on the extrusion velocity and on the power law flow in the needle at $z = 0.6\,mm$.

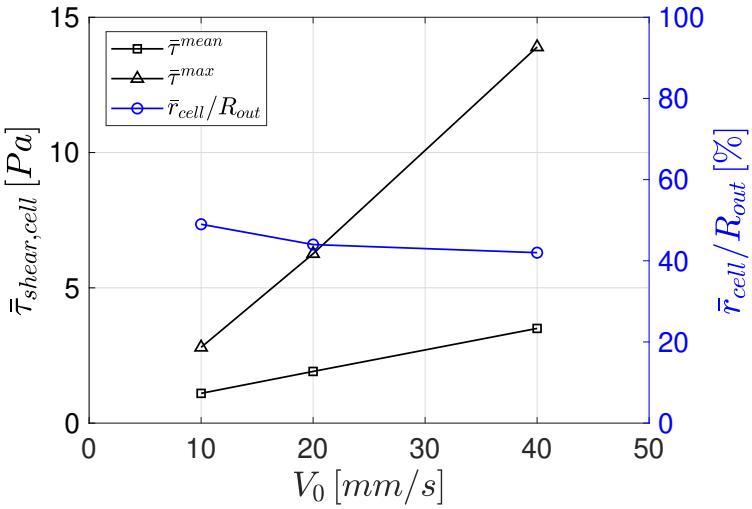


**Figure 4.33:** Mean and maximum shear stress (black, left axis) and percentage radial position $\bar{r}_{cell}/R_{out}$ (blue, right axis) of the cell population as a function of the extrusion velocity $V_0$ reported in Table 4.8.

# Conclusions

In this work two kinds of mathematical approaches for extrusion bioprinting process have been presented. The first one is a quasi-analytical model and assumes the bio-ink as a homogeneous fluid. In literature, several works adopt this assumption and they usually employ simple rheological models, such as the Newtonian model [13] or the power law model [11, 12]. Other works adopt more accurate relationships to describe the rheological behaviour of bio-inks, such as the five-parameters Bird-Cross-Carreau-Yasuda (BCCY) model [15]. However, this model requires an ad hoc optimization procedure for the parameters calibration, since it suffers from an intrinsic problem of parameters identifiability and may lead to unreliable flow solutions [16].

With the aim to overcome this problem, the shear rate based (SRB) model in Eq. (2.24) has been developed in Section 2.3.1, in order to have a more physically-consistent rheological relationship than the BCCY model, and to derive reliable and quasi-analytical solutions for bio-ink flows. In particular, it is able to capture the physical meaning of the shear thinning index $n$ in respect than the BCCY model as shown in the fitting tests reported in Figs. 3.6, 3.7 and in the power law velocity profiles analysis shown in Fig. 3.8. Furthermore, it shows very good fitting capabilities at the expense of a maximum coefficient of determination $R^2_{LMAPE}$ reduction of 5% as reported in Table 3.2.

Next, through the PWM approximation in Eqs. (3.1), (3.2) quasi-analytical solutions of the main flow problem variables for cylindrical and conical nozzles have been provided in Eqs. (3.9)-(3.11) and in Eqs. (3.60)-(3.61) together the Algorithm 1 respectively. In particular for cylindrical flows, the Figure 3.9 allows a direct assessment of the pressure drop applied to the nozzle and of the corresponding extrusion velocity, together to the evaluation of the Newtonian/power law flow conditions of the bio-ink. Regarding the velocity profiles, the comparison reported in Fig. 3.11 between the quai-analytical solution and the finite difference numerical one showed a robust consistency of the analytical approach, with a maximum error

on the computed extrusion velocity well below engineering approximations. The proposed quasi-analytical solution is a novel tool for fast and ready-to-use screening evaluations on the mutual impact of main process variables in the planning of bioprinting. Finally, the quasi-analytical model for slightly tapered nozzles has been applied for the reproduction of an experimental setup, and it showed a good agreement with the experimental data on the pressure drop value (error 6 %).

The Chapter 4 presents the second mathematical approach considering the bio-ink as a heterogeneous flow, and addressing the complex FSI taking place between the fluid and cellular phases within the bio-ink. In this regard, so far only few examples has been found in literature [17–19]. In particular, Müller *et al.*[18] evaluated the stress and strain only of a single cell flowing out the nozzle exit.

The numerical model proposed in this thesis allowed a detailed full-3D dynamic evaluation of the cell extrusion by analysing the radial equilibrium position, the axial velocity and the load history through statistical analysis on the cell population extruded through a nozzle with standard commercial sizes [49, 62]. Results of the FSI simulations have been focused on the mean and maximum shear stress experienced by cells during the bioprinting process and have been compared with the classic approach, which considers a homogeneous fluid and a radial equilibrium position at $0.6\,R_{out}$, with $R_{out}$ the outlet nozzle radius. The results of the reference case with an outlet diameter $D_{out} = 200\,\mu m$ showed how the classic solution overestimates the mean shear stress computed through the FSI approach, and underestimates the maximum shear stress in the needle region. In particular, the FSI solution presents a maximum to mean shear stress ratio up to +328 %. Furthermore, the classic approach is not able to follow the unsteady behaviour of the shear stresses in the convergent region, where the FSI solution reports the maximum peak value. In addition, the numerical solution presents a radial equilibrium position of the cell population at $0.44\,R_{out}$ different from the theoretical value $0.6\,R_{out}$. This could be explained since the not-negligible dimensions of cells considered in respect to the nozzle ones; while the theoretical solution is referred to smaller particle sizes. Next, the parametric analysis results performed by varying the outlet diameter from $100\,\mu m$ to $330\,\mu m$ report in Table 4.6 a shift of the radial equilibrium position towards the nozzle wall for increasing diameters and approaching the theoretical value $0.6\,R_{out}$, since the decreasing $D_{cell}/D_{out}$ ratio with $D_{cell}$ the cell diameter. Finally, by increasing the extrusion velocity the Figure 4.33 shows a maximum shear stress with a greater slope than the mean value about +380 %.

# Future steps

A next step for the quasi-analytical model presented in the Chapter 3 could be to derive a solution for the extensional stresses of the fluid, since in addition to cell damage caused by shear stress damage, also extensional stresses (sometimes referred as elongational stresses) could affect cell vitality as reported in the literature [18, 49, 55, 172–174]. Furthermore, for the flows in slightly tapered nozzles, the solution developed in Section 3.3 could be improved by an approximated solution for the radial velocity component $v_r$, obtainable by not neglecting the radial gradient terms in the momentum balance Eq. (3.15b). This improvement could

shed a light on the radial positioning of cells during extrusion, as analysed in the Chapter 4.

Regarding the numerical FSI model presented in the Chapter 4, next simulations could be to consider higher cell densities, and less stiff cells with lower Young's modulus values to investigate the influence of cell deformations on the extrusion dynamics. Next, the proposed model could be used to support the optimization of the nozzle shape in order to limit the shear stresses experienced by the cells. Another step could be to improve the analysis of cell stresses by taking into account also the extensional contributes, which arise in the convergent region of the nozzle. Then, a further enhancement could be to develop a cell damage criteria based on mechanobiological stimuli applied to local cell surface. Another future step could be to tackle the analysis of more complex process such as the co-axial bioprinting [175, 176], by analysing in addition the extensional stresses arising at the nozzle outlet [18]. Furthermore, thanks to the large amount of parallelism in graphics hardware [177, 178], the numerical solver could be moved in a high performance computing-GPU environment in order to decrease the computational cost of the FSI simulations.

In addition, both for the quasi-analytical and numerical FSI model, a visco-elastic rheological model of the fluid might allow for a better description of the constitutive response of bio-inks mechanics, and then for a higher fidelity in the analysis of stresses and strains experienced by cells during extrusion.

# Appendix A

## Scaling property of Stokes flows

Considering a non-Newtonian inelastic fluid with a constitutive relationship approximated through the PWM model in Eq. (3.1), and thus with a viscosity range delimited by the zero-shear rate $\mu_0$ and infinity-shear rate $\mu_\infty$ viscosity, taking as reference values a diameter $D$, an extrusion velocity $V_0$, the infinity-shear rate viscosity $\mu_\infty$ and a pressure $p_0 = \mu_\infty V_0/D$, the non-dimensional momentum balance Eq. (2.15) results

$$Re_\infty \frac{D\boldsymbol{v}'}{Dt'} = -\nabla p' + \nabla \cdot \boldsymbol{\tau}' \ , \tag{A.1}$$

where the apex $f'$ indicates the corresponding non-dimensional variable and $Re_\infty = \rho V_0 D/\mu_\infty$. Thus, considering a flow at low Reynolds number the previous equations turns out in the Stokes' flow equation

$$\mathbf{0} = -\nabla p' + \nabla \cdot \boldsymbol{\tau}' \ . \tag{A.2}$$

Then, considering as geometry a cylindrical nozzle, and thus implicating a Poiseuille velocity profile $\boldsymbol{v}' = [0 \ 0 \ v_z'(r')]^T$, with flow conditions such as to lead shear rate values high enough to approximate the viscosity with the constant $\mu = \mu_\infty$ value, such as the bioprinting flows analysed in Section 4.6 (the same following demonstration cab be performed by considering low shear rate flows with $\mu = \mu_0$), the previous equation projected along the axial direction turns out

$$z') \qquad 0 = -\frac{dp'}{dz'} + \frac{1}{r'}\frac{d}{dr'}\left(r'\frac{dv_z'}{dr'}\right) \ . \tag{A.3}$$

Next, applying the symmetric flow boundary condition on the nozzle axis and the no-slip boundary condition at the wall, the solutions of the axial velocity and shear stress modulus result

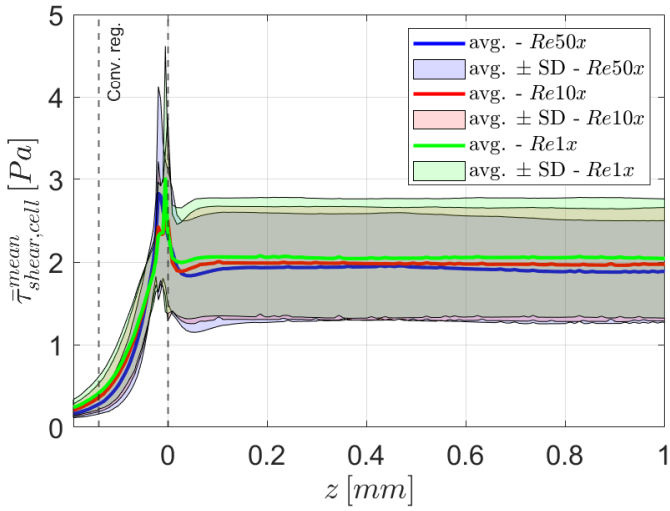


**Figure 34:** Mean and maximum shear stress of the cell.

$$v'_z(r') = 2\left[1 - \left(\frac{r'}{R'}\right)^2\right] , \tag{A.4}$$

$$\tau'_{shear}(r') = |\tau'_{z'r'}(r')| = \left|\frac{dv'_z}{dr'}(r')\right| , \tag{A.5}$$

with $R'$ the non-dimensional nozzle radius.

Thus, the corresponding dimensional shear stress reads

$$\tau_{shear}(r) = \frac{\mu_\infty V_0}{D}\left|\frac{dv'_z}{dr'}(r')\right| = \frac{\rho V_0^2}{Re_\infty}\left|\frac{dv'_z}{dr'}(r')\right| , \tag{A.6}$$

showing how for Stokes' flows in cylindrical nozzles the shear stress modulus is inversely proportional to the Reynolds number. This property has been used in the parametric analyses carried out in Section 4.6.3, to scale the results of simulations performed with the same geometry and extrusion velocities, but at lower viscosity values corresponding to higher Reynolds numbers, but always in the Stokes' flow regime, in order to reduce the limitation on the time step imposed by the condition in Eq. (4.16).

As a proof, in Fig. 34 the shear stress results of two test simulations performed at greater Reynolds number with viscosity values decreased respectively of a factor 10 (with label $Re10x$) and 50 (with label $Re50x$), and compared to those of the reference case in Section 4.6.2 (with label $Re1x$) have been reported. In particular, the mean shear stress acting on the cell population of the two test simulations has been scaled accordingly to the Eq. (A.6), (the non-dimensional term $|dv'_z(r')//dr'|$ does not influence the results, since the geometry and the Poiseuille velocity profiles are the same for all the three simulations). It is possible to note how the three

solutions report almost the same values with a loss of accuracy of 6 % in the needle region, thus validating the scaling procedure adopted.

Considering flow conditions such that to have shear rates intermediated between the $\dot{\gamma}_0$ and the $\dot{\gamma}_\infty$ values of the PWM model, corresponding to a viscosity ranging between $\mu_0$ and $\mu_\infty$, namely a power law flow characterized by a consistency index $K = \mu_\infty \dot{\gamma}_\infty^{1-n}$ and a power law index $n$, the demonstration in analogous to the previous case and the Eqs. (A.4)-(A.6) turn out

$$v'_z(r') = \frac{3n+1}{n+1}\left[1 - \left(\frac{r'}{R'}\right)^{\frac{n+1}{n}}\right] , \tag{A.7}$$

$$\tau'_{shear}(r') = |\tau'_{z'r'}(r')| = \frac{KV_0^{n-1}}{\mu_\infty D^{n-1}}\left|\frac{dv'_z}{dr'}(r')\right|^n = SR_\infty^{n-1}\left|\frac{dv'_z}{dr'}(r')\right|^n , \tag{A.8}$$

$$\tau_{shear}(r) = \frac{\rho V_0^2}{Re_\infty} SR_\infty^{n-1}\left|\frac{dv'_z}{dr'}(r')\right|^n , \tag{A.9}$$

where $SR_\infty = V_0/(D\dot{\gamma}_\infty)$ is the ratio between the shear rate of the flow and the rheological infinity-shear rate of the fluid, indicating an inversely proportional relationship between the shear stress and the Reynolds number also in this case.

# Bibliography


[1] Yu Shrike Zhang, Ghazaleh Haghiashtiani, Tania Hübscher, Daniel J Kelly, Jia Min Lee, et al. "3D extrusion bioprinting". *Nature Reviews Methods Primers* 1.1 (2021), p. 75.

[2] Sean V Murphy and Anthony Atala. "3D bioprinting of tissues and organs". *Nature biotechnology* 32.8 (2014), pp. 773–785.

[3] Andrew C Daly, Margaret E Prendergast, Alex J Hughes, and Jason A Burdick. "Bioprinting for the Biologist". *Cell* 184.1 (2021), pp. 18–32.

[4] Adnan Memic, Ali Navaei, Bahram Mirani, Julio Alvin Vacacela Cordova, Musab Aldhahri, et al. "Bioprinting technologies for disease modeling". *Biotechnology letters* 39 (2017), pp. 1279–1290.

[5] Weijie Peng, Pallab Datta, Bugra Ayan, Veli Ozbolat, Donna Sosnoski, et al. "3D bioprinting for drug discovery and development in pharmaceutics". *Acta biomaterialia* 57 (2017), pp. 26–46.

[6] Wen-Juan Song, Pei-Pei Liu, Zi-Qing Meng, Yan-Yan Zheng, Guang-Hong Zhou, et al. "Identification of porcine adipose progenitor cells by fluorescence-activated cell sorting for the preparation of cultured fat by 3D bioprinting". *Food Research International* 162 (2022), p. 111952.

[7] Nieves Cubo-Mateo, Sandra Podhajsky, Daniela Knickmann, Klaus Slenzka, Tommaso Ghidini, et al. "Can 3D bioprinting be a key for exploratory missions and human settlements on the Moon and Mars?": *Biofabrication* 12.4 (2020), p. 043001.

[8] Hemanth Gudapati, Madhuri Dey, and Ibrahim Ozbolat. "A comprehensive review on droplet-based bioprinting: Past, present and future". *Biomaterials* 102 (2016), pp. 20–42.

[9] Kolin C Hribar, Pranav Soman, John Warner, Peter Chung, and Shaochen Chen. "Light-assisted direct-write of 3D functional biomaterials". *Lab on a chip* 14.2 (2014), pp. 268–275.

[10] Ibrahim T Ozbolat and Monika Hospodiuk. "Current advances and future perspectives in extrusion-based bioprinting". *Biomaterials* 76 (2016), pp. 321–343.

[11] Thomas Billiet, Elien Gevaert, Thomas De Schryver, Maria Cornelissen, and Peter Dubruel. "The 3D printing of gelatin methacrylamide cell-laden tissue-engineered constructs with high cell viability". *Biomaterials* 35.1 (2014), pp. 49–62.

[12] Irene Chiesa, Cosimo Ligorio, Amedeo F Bonatti, Aurora De Acutis, Andrew M Smith, et al. "Modeling the three-dimensional bioprinting process of $\beta$-sheet self-assembling peptide hydrogel scaffolds". *Frontiers in Medical Technology* 2 (2020), p. 571626.

[13] Juan Carlos Gómez Blanco, Enrique Mancha Sánchez, Diego Torrejón Martın, Juan Pablo Carrasco Amador, Francisco Miguel Sánchez Margallo, et al. "Nozzle pressure analysis of several hydrogel on extrusion-based bioprinting using computational fluid dynamics". *Actas de las XXXIX Jornadas de Automática, Badajoz, 5-7 de Septiembre de 2018* (2018).

[14] Simon Ingelsten, Johan Göhl, Andreas Mark, and Fredrik Edelvik. "A virtual framework for simulation of complex viscoelastic flows". *Procedia CIRP* 72 (2018), pp. 392–397.

[15] Harvey Williams, Michael McPhail, Sourav Mondal, and Andreas Münch. "Modeling gel fiber formation in an emerging coaxial flow from a nozzle". *Journal of Fluids Engineering* 141.1 (2019).

[16] Meurig Thomas Gallagher, Richard AJ Wain, Sonia Dari, Justin P Whitty, and David J Smith. "Non-identifiability of parameters for a class of shear-thinning rheological models, with implications for haematological fluid dynamics". *Journal of Biomechanics* 85 (2019), pp. 230–238.

[17] Hassan Abedini, Saeid Movahed, and Nabiollah Abolfathi. "Numerical Simulation of Pressure-Induced Cell Printing". *Journal of Mechanics in Medicine and Biology* 15.05 (2015), p. 1550065.

[18] Sebastian Johannes Mueller, Ben Fabry, and Stephan Gekle. "Predicting cell stress and strain during extrusion bioprinting". *arXiv preprint arXiv:2209.13666* (2022).

[19] Samir Das, Amit Roy Chowdhury, and Pallab Datta. "Modelling cell deformations in bioprinting process using a multicompartment-smooth particle hydrodynamics approach". *Proceedings of the Institution of Mechanical Engineers, Part H: Journal of Engineering in Medicine* 236.6 (2022), pp. 867–881.

[20] Jipeng Li, Mingjiao Chen, Xianqun Fan, and Huifang Zhou. "Recent advances in bioprinting techniques: approaches, applications and future prospects". *Journal of translational medicine* 14.1 (2016), pp. 1–15.

[21] Lorenzo Moroni, Thomas Boland, Jason A Burdick, Carmelo De Maria, Brian Derby, et al. "Biofabrication: a guide to technology and terminology". *Trends in biotechnology* 36.4 (2018), pp. 384–402.

[22] *Bioprinting - Wikimedia Commons*. 2017. URL: `https://commons.wikimedia.org/wiki/`.

[23] Adriene Pavek, Christopher Nartker, Maamoon Saleh, Matthew Kirkham, Sana Khajeh Pour, et al. "Tissue engineering through 3D bioprinting to recreate and study bone disease". *Biomedicines* 9.5 (2021), p. 551.

[24] Serge Ostrovidov, Sahar Salehi, Marco Costantini, Kasinan Suthiwanich, Majid Ebrahimi, et al. "3D bioprinting in skeletal muscle tissue engineering". *Small* 15.24 (2019), p. 1805530.

[25] Melissa Cadena, Liqun Ning, Alexia King, Boeun Hwang, Linqi Jin, et al. "3D bioprinting of neural tissues". *Advanced healthcare materials* 10.15 (2021), p. 2001600.

[26] MP Sealy, KLM Avegnon, A Garrett, Laurent Delbreilh, S Bapat, et al. "Understanding biomanufacturing of soy-based scaffolds for cell-cultured meat by vat polymerization". *CIRP Annals* 71.1 (2022), pp. 209–212.

[27] Lynn J Rothschild. "Synthetic biology meets bioprinting: enabling technologies for humans on Mars (and Earth)". *Biochemical Society Transactions* 44.4 (2016), pp. 1158–1164.

[28] Željka P Kačarević, Patrick M Rider, Said Alkildani, Sujith Retnasingh, Ralf Smeets, et al. "An introduction to 3D bioprinting: possibilities, challenges and future aspects". *Materials* 11.11 (2018), p. 2199.

[29] Roberto Pantani and Lih-Sheng Turng. *Manufacturing of advanced biodegradable polymeric components*. 2015.

[30] Janarthanan Gopinathan and Insup Noh. "Recent trends in bioinks for 3D printing". *Biomaterials research* 22 (2018), pp. 1–15.

[31] Fatemeh Kabirian and Masoud Mozafari. "Decellularized ECM-derived bioinks: Prospects for the future". *Methods* 171 (2020), pp. 108–118.

[32] Byoung Soo Kim, Hyeonji Kim, Ge Gao, Jinah Jang, and Dong-Woo Cho. "Decellularized extracellular matrix: a step towards the next generation source for bioink manufacturing". *Biofabrication* 9.3 (2017), p. 034104.

[33] Falguni Pati, Jinah Jang, Dong-Heon Ha, Sung Won Kim, Jong-Won Rhie, et al. "Printing three-dimensional tissue analogues with decellularized extracellular matrix bioink". *Nature communications* 5.1 (2014), p. 3935.

[34] Ashley N Leberfinger, Shantanab Dinda, Yang Wu, Srinivas V Koduru, Veli Ozbolat, et al. "Bioprinting functional tissues". *Acta biomaterialia* 95 (2019), pp. 32–49.

[35] Behnaz Bakhshandeh, Payam Zarrintaj, Mohammad Omid Oftadeh, Farid Keramati, Hamideh Fouladiha, et al. "Tissue engineering; strategies, tissues, and biomaterials". *Biotechnology and genetic engineering reviews* 33.2 (2017), pp. 144–172.

[36] Amedeo Franco Bonatti, Gabriele Maria Fortunato, Carmelo De Maria, and Giovanni Vozzi. "Bioprinting technologies: an overview". *Bioprinting* (2022), pp. 19–49.

[37] Previn Ramiah, Lisa C Du Toit, Yahya E Choonara, Pierre PD Kondiah, and Viness Pillay. "Hydrogel-based bioinks for 3D bioprinting in tissue regeneration". *Frontiers in Materials* 7 (2020), p. 76.

[38] Rúben F Pereira and Paulo J Bártolo. "3D bioprinting of photocrosslinkable hydrogel constructs". *Journal of Applied Polymer Science* 132.48 (2015).

[39] MM Stanton, J Samitier, and Samuel Sanchez. "Bioprinting of 3D hydrogels". *Lab on a Chip* 15.15 (2015), pp. 3111–3115.

[40] Mengxiang Zhu, Yingying Wang, Gaia Ferracci, Jing Zheng, Nam-Joon Cho, et al. "Gelatin methacryloyl and its hydrogels with an exceptional degree of controllability and batch-to-batch consistency". *Scientific reports* 9.1 (2019), pp. 1–13.

[41] Zeyu Luo, Xuan Mu, and Yu Shrike Zhang. "Biomaterials for bioprinting". *Bioprinting*. Elsevier, 2022, pp. 51–86.

[42] Amin GhavamiNejad, Nureddin Ashammakhi, Xiao Yu Wu, and Ali Khademhosseini. "Crosslinking strategies for 3D bioprinting of polymeric hydrogels". *Small* 16.35 (2020), p. 2002931.

[43] Jos Malda, Jetze Visser, Ferry P Melchels, Tomasz Jüngst, Wim E Hennink, et al. "25th anniversary article: engineering hydrogels for biofabrication". *Advanced materials* 25.36 (2013), pp. 5011–5028.

[44] Bruce Alberts, Dennis Bray, Karen Hopkin, Alexander D Johnson, Julian Lewis, et al. *Essential cell biology*. Garland Science, 2015.

[45] *Scitable by Nature Education - What is a cell*. 2014. URL: `https://www.nature.com/scitable/topicpage/what-is-a-cell-14023083/`.

[46] Eustace Anthony Evans. *Mechanics and thermodynamics of biomembranes*. CRC press, 2018.

[47] Julia Emmermacher, David Spura, Jasmina Cziommer, David Kilian, Tobias Wollborn, et al. "Engineering considerations on extrusion-based bioprinting: interactions of material behavior, mechanical forces and cells in the printing needle". *Biofabrication* 12.2 (2020), p. 025022.

[48] Johan Göhl, Kajsa Markstedt, Andreas Mark, Karl Håkansson, Paul Gatenholm, et al. "Simulations of 3D bioprinting: predicting bioprintability of nanofibrillar inks". *Biofabrication* 10.3 (2018), p. 034105.

[49] Liqun Ning, Nicholas Betancourt, David J Schreyer, and Xiongbiao Chen. "Characterization of cell damage and proliferative ability during and after bioprinting". *ACS Biomaterials Science & Engineering* 4.11 (2018), pp. 3906–3918.

[50] Michele Conti, Gianluca Santesarti, Franca Scocozza, and Michele Marino. "Models and simulations as enabling technologies for bioprinting process design". *Bioprinting*. Elsevier, 2022, pp. 137–206.

[51] Naomi Paxton, Willi Smolan, Thomas Böck, Ferry Melchels, Jürgen Groll, et al. "Proposal to assess printability of bioinks for extrusion-based bioprinting and evaluation of rheological properties governing bioprintability". *Biofabrication* 9.4 (2017), p. 044107.

[52] Kalyani Nair, Milind Gandhi, Saif Khalil, Karen Chang Yan, Michele Marcolongo, et al. "Characterization of cell viability during bioprinting processes". *Biotechnology Journal: Healthcare Nutrition Technology* 4.8 (2009), pp. 1168–1177.

[53] Jia Shi, Bin Wu, Shihao Li, Jinchun Song, Bin Song, et al. "Shear stress analysis and its effects on cell viability and cell proliferation in drop-on-demand bioprinting". *Biomedical Physics & Engineering Express* 4.4 (2018), p. 045028.

[54] Minggan Li, Xiaoyu Tian, Janusz A Kozinski, Xiongbiao Chen, and Dae Kun Hwang. "Modeling mechanical cell damage in the bioprinting process employing a conical needle". *Journal of Mechanics in Medicine and Biology* 15.05 (2015), p. 1550073.

[55] Selwa Boularaoui, Ghada Al Hussein, Kamran A Khan, Nicolas Christoforou, and Cesare Stefanini. "An overview of extrusion-based bioprinting with a focus on induced shear stress and its effect on cell viability". *Bioprinting* 20 (2020), e00093.

[56] Robert Chang, JAE Nam, and WEI Sun. "Effects of dispensing pressure and nozzle diameter on cell survival from solid freeform fabrication–based direct cell writing". *Tissue Engineering Part A* 14.1 (2008), pp. 41–48.

[57] Linlin Zhu, Feng Wang, Hongfeng Yang, Junjie Zhang, and Shaoliang Chen. "Low shear stress damages endothelial function through STAT1 in endothelial cells (ECs)". *Journal of physiology and biochemistry* 76.1 (2020), pp. 147–157.

[58] Kai-Yin Lo, Yun Zhu, Hsieh-Fu Tsai, and Yung-Shin Sun. "Effects of shear stresses and antioxidant concentrations on the production of reactive oxygen species in lung cancer cells". *Biomicrofluidics* 7.6 (2013), p. 064108.

[59] Deekshitha Jetta, Philip A Gottlieb, Deepika Verma, Frederick Sachs, and Susan Z Hua. "Shear stress-induced nuclear shrinkage through activation of Piezo1 channels in epithelial cells". *Journal of Cell Science* 132.11 (2019), jcs226076.

[60] Jing Zhou, Yi-Shuan Li, and Shu Chien. "Shear stress–initiated signaling and its regulation of endothelial function". *Arteriosclerosis, thrombosis, and vascular biology* 34.10 (2014), pp. 2191–2198.

[61] Sudipto Datta, Ankita Das, Amit Roy Chowdhury, and Pallab Datta. "Bioink formulations to ameliorate bioprinting-induced loss of cellular viability". *Biointerphases* 14.5 (2019), p. 051006.

[62] *Nordson - General purpose dispense tips*. 2023. URL: `https://www.nordson.com/en/products/efd-products/general-purpose-dispense-tips`.

[63] Cx K Batchelor and GK Batchelor. *An introduction to fluid dynamics*. Cambridge university press, 1967.

[64] Bastian E Rapp. *Microfluidics: modeling, mechanics and mathematics*. Elsevier, 2022.

[65] Sean V Murphy, Aleksander Skardal, and Anthony Atala. "Evaluation of hydrogels for bio-printing applications". *Journal of Biomedical Materials Research Part A* 101.1 (2013), pp. 272–284.

[66] Shuai Wang, Jia Min Lee, and Wai Yee Yeong. "Smart hydrogels for 3D bioprinting". *International Journal of Bioprinting* 1.1 (2015).

[67] Farhad Abasalizadeh, Sevil Vaghefi Moghaddam, Effat Alizadeh, Elmira Kashani, Seyyed Mohammad Bagher Fazljou, et al. "Alginate-based hydrogels as drug delivery vehicles in cancer treatment and their applications in wound dressing and 3D bioprinting". *Journal of biological engineering* 14.1 (2020), pp. 1–22.

[68] Katja Hölzl, Shengmao Lin, Liesbeth Tytgat, Sandra Van Vlierberghe, Linxia Gu, et al. "Bioink properties before, during and after 3D bioprinting". *Biofabrication* 8.3 (2016), p. 032002.

[69] Christopher E Brennen. *Fundamentals of multiphase flow*. Cambridge university press, 2005.

[70] WZ Song, AQ Liu, S Swaminathan, CS Lim, PH Yap, et al. "Determination of single living cell's dry/water mass using optofluidic chip". *Applied physics letters* 91.22 (2007), p. 223902.

[71] MS Manoussaka, DJ Jackson, RJ Lock, SR Sooranna, and BM Kumpel. "Flow cytometric characterisation of cells of differing densities isolated from human term placentae and enrichment of villous trophoblast cells". *Placenta* 26.4 (2005), pp. 308–318.

[72] William H Grover, Andrea K Bryan, Monica Diez-Silva, Subra Suresh, John M Higgins, et al. "Measuring single-cell density". *Proceedings of the National Academy of Sciences* 108.27 (2011), pp. 10992–10996.

[73] Raj P Chhabra and John Francis Richardson. *Non-Newtonian flow and applied rheology: engineering applications*. Butterworth-Heinemann, 2011.

[74] Robert Byron Bird, Robert C Armstrong, and Ole Hassager. *Dynamics of polymeric liquids. Vol. 1: Fluid mechanics*. Wiley, 1987.

[75] Wo Ostwald and R Auerbach. "Ueber die Viskosität kolloider Lösungen im Struktur-, Laminar-und Turbulenzgebiet: Ueber die Geschwindigkeitsfunktion der Viskosität disperser Systeme, V". *Kolloid-Zeitschrift* 38 (1926), pp. 261–280.

[76] Armand Waele. *Viscometry and plastometry*. Oil and Colour Chemists' Association, 1923.

[77] Pierre J Carreau. "Rheological equations from molecular network theories". *Transactions of the Society of Rheology* 16.1 (1972), pp. 99–127.

[78] Frank JH Gijsen, Frans N van de Vosse, and JD Janssen. "The influence of the non-Newtonian properties of blood on the flow in large arteries: steady flow in a carotid bifurcation model". *Journal of biomechanics* 32.6 (1999), pp. 601–608.

[79] V Mazzanti, F Mollica, and N El Kissi. “Rheological and mechanical characterization of polypropylene-based wood plastic composites”. *Polymer Composites* 37.12 (2016), pp. 3460–3473.

[80] Scott Bair. “A more complete description of the shear rheology of high-temperature, high-shear journal bearing lubrication”. *Tribology transactions* 49.1 (2006), pp. 39–45.

[81] Bárbara E Meza, Juan Manuel Peralta, and Susana E Zorrilla. “Effect of temperature and composition on rheological behaviour and sagging capacity of glaze materials for foods”. *Food Hydrocolloids* 117 (2021), p. 106689.

[82] Seikichi Matsuhisa and R Byron Bird. “Analytical and numerical solutions for laminar flow of the non-Newtonian ellis fluid”. *AIChE Journal* 11.4 (1965), pp. 588–595.

[83] Kenji Yasuda. “Investigation of the analogies between viscometric and linear viscoelastic properties of polystyrene fluids”. PhD thesis. Massachusetts Institute of Technology, 1979.

[84] Shangjing Xin, Kaivalya A Deo, Jing Dai, Navaneeth Krishna Rajeeva Pandian, David Chimene, et al. “Generalizing hydrogel microparticles into a new class of bioinks for extrusion bioprinting”. *Science Advances* 7.42 (2021), eabk3087.

[85] Martin Maxey. “Simulation methods for particulate flows and concentrated suspensions”. *Annual Review of Fluid Mechanics* 49 (2017), pp. 171–193.

[86] Diana Massai, Giuseppe Isu, Denise Madeddu, Giulia Cerino, Angela Falco, et al. “A versatile bioreactor for dynamic suspension cell culture. Application to the culture of cancer cell spheroids”. *PloS one* 11.5 (2016), e0154610.

[87] Emil Prodan, Camelia Prodan, and John H Miller. “The dielectric response of spherical live cells in suspension: an analytic solution”. *Biophysical journal* 95.9 (2008), pp. 4174–4182.

[88] OO Oyeleye, ST Ogundeji, SI Ola, and OG Omitogun. “Basics of animal cell culture: Foundation for modern science”. *Academic Journals* (2016).

[89] Michelle E Staben and Robert H Davis. “Particle transport in Poiseuille flow in narrow channels”. *International journal of multiphase flow* 31.5 (2005), pp. 529–547.

[90] Jean-Philippe Matas, Jeffrey F Morris, and Élisabeth Guazzelli. “Inertial migration of rigid spherical particles in Poiseuille flow”. *Journal of fluid mechanics* 515 (2004), pp. 171–195.

[91] Francis P Bretherton. “The motion of rigid particles in a shear flow at low Reynolds number”. *Journal of Fluid Mechanics* 14.2 (1962), pp. 284–304.

[92] Ali Asgar S Bhagat, Sathyakumar S Kuntaegowdanahalli, and Ian Papautsky. “Inertial microfluidics for continuous particle filtration and extraction”. *Microfluidics and nanofluidics* 7 (2009), pp. 217–226.

[93] Dino Di Carlo, Daniel Irimia, Ronald G Tompkins, and Mehmet Toner. “Continuous inertial focusing, ordering, and separation of particles in microchannels”. *Proceedings of the National Academy of Sciences* 104.48 (2007), pp. 18892–18897.

[94] G Segre and Alex Silberberg. "Behaviour of macroscopic rigid spheres in Poiseuille flow Part 2. Experimental results and interpretation". *Journal of fluid mechanics* 14.1 (1962), pp. 136–157.

[95] Minsoo Han, Chongyoup Kim, Minchul Kim, and Soonchil Lee. "Particle migration in tube flow of suspensions". *Journal of rheology* 43.5 (1999), pp. 1157–1174.

[96] Philip Geoffrey Saffman. "The lift on a small sphere in a slow shear flow". *Journal of fluid mechanics* 22.2 (1965), pp. 385–400.

[97] Sebastian J Müller, Elham Mirzahossein, Emil N Iftekhar, Christian Bächer, Stefan Schrüfer, et al. "Flow and hydrodynamic shear stress inside a printing needle during biofabrication". *PLoS One* 15.7 (2020), e0236371.

[98] Fridtjov Irgens. *Rheology and non-newtonian fluids*. Springer, 2014.

[99] Ratima Suntornnond, Edgar Yong Sheng Tan, Jia An, and Chee Kai Chua. "A mathematical model on the resolution of extrusion bioprinting for the development of new bioinks". *Materials* 9.9 (2016), p. 756.

[100] John R Pearson. *Mechanics of polymer processing*. Springer Science & Business Media, 1985.

[101] DW Dodge and AB Metzner. "Turbulent flow of non-Newtonian systems". *AIChE journal* 5.2 (1959), pp. 189–204.

[102] Maedeh Rahimnejad, Thierry Labonte-Dupuis, Nicole R Demarquette, and Sophie Lerouge. "A rheological approach to assess the printability of thermosensitive chitosan-based biomaterial inks". *Biomedical Materials* 16.1 (2020), p. 015003.

[103] Cristina Colosi, Su Ryon Shin, Vijayan Manoharan, Solange Massa, Marco Costantini, et al. "Microfluidic bioprinting of heterogeneous 3D tissue constructs using low-viscosity bioink". *Advanced materials* 28.4 (2016), pp. 677–684.

[104] Lucas Lemarié, Aravind Anandan, Emma Petiot, Christophe Marquette, and Edwin-Joffrey Courtial. "Rheology, simulation and data analysis toward bioprinting cell viability awareness". *Bioprinting* 21 (2021), e00119.

[105] Beatrice Belgio, Sara Mantero, et al. "Ottimizzazione di idrogeli per la realizzazione di scaffold nell'ingegneria dei tessuti della retina mediante 3D bioprinting" (2021).

[106] Jinchen Sun and Huaping Tan. "Alginate-based biomaterials for regenerative medicine applications". *Materials* 6.4 (2013), pp. 1285–1309.

[107] Tao Jiang, Jose G Munguia-Lopez, Kevin Gu, Maeva M Bavoux, Salvador Flores-Torres, et al. "Engineering bioprintable alginate/gelatin composite hydrogels with tunable mechanical and cell adhesive properties to modulate tumor spheroid growth kinetics". *Biofabrication* 12.1 (2019), p. 015024.

[108] Samuel M Hart, Eric O McGhee, Juan Manuel Urueña, Padraic P Levings, Stephen S Eikenberry, et al. "Surface gel layers reduce shear stress and damage of corneal epithelial cells". *Tribology Letters* 68 (2020), pp. 1–9.

[109] Joel H Ferziger, Milovan Perić, and Robert L Street. *Computational methods for fluid dynamics*. Vol. 3. Springer, 2002.

[110] Michael P Paıdoussis, Stuart J Price, and Emmanuel De Langre. *Fluid-structure interactions: cross-flow-induced instabilities*. Cambridge University Press, 2010.

[111] Yuri Bazilevs, Kenji Takizawa, and Tayfun E Tezduyar. *Computational fluid-structure interaction: methods and applications*. John Wiley & Sons, 2013.

[112] Gene Hou, Jin Wang, and Anita Layton. "Numerical methods for fluid-structure interaction—a review". *Communications in Computational Physics* 12.2 (2012), pp. 337–377.

[113] Stefan Turek and Jaroslav Hron. *Proposal for numerical benchmarking of fluid-structure interaction between an elastic object and laminar incompressible flow*. Springer, 2006.

[114] Patrick Le Tallec and Jean Mouro. "Fluid structure interaction with large structural displacements". *Computer methods in applied mechanics and engineering* 190.24-25 (2001), pp. 3039–3067.

[115] M Bukač, S Čanić, and Boris Muha. "A partitioned scheme for fluid–composite structure interaction problems". *Journal of Computational Physics* 281 (2015), pp. 493–517.

[116] Yuqi Wu and Xiao-Chuan Cai. "A fully implicit domain decomposition based ALE framework for three-dimensional fluid–structure interaction with application in blood flow computation". *Journal of Computational Physics* 258 (2014), pp. 524–537.

[117] Marco D de Tullio and Giuseppe Pascazio. "A moving-least-squares immersed boundary method for simulating the fluid-structure interaction of elastic bodies with arbitrary thickness". *Journal of Computational Physics* 325 (2016), pp. 201–225.

[118] Tomohiro Sawada and Toshiaki Hisada. "Fluid–structure interaction analysis of the two-dimensional flag-in-wind problem by an interface-tracking ALE finite element method". *Computers & Fluids* 36.1 (2007), pp. 136–146.

[119] Andrea Chierici. "Mathematical and Numerical Models for Boundary Optimal Control Problems Applied to Fluid-Structure Interaction". PhD thesis. alma, 2021. URL: `http://amsdottorato.unibo.it/9856/`.

[120] Charles S Peskin. "Flow patterns around heart valves: a numerical method". *Journal of computational physics* 10.2 (1972), pp. 252–271.

[121] Rajat Mittal and Gianluca Iaccarino. "Immersed boundary methods". *Annu. Rev. Fluid Mech.* 37 (2005), pp. 239–261.

[122] Núria Gavara and Richard S Chadwick. "Determination of the elastic moduli of thin samples and adherent cells using conical atomic force microscope tips". *Nature nanotechnology* 7.11 (2012), pp. 733–736.

[123] Qiuquan Guo, Ying Xia, Martin Sandig, and Jun Yang. "Characterization of cell elasticity correlated with cell morphology by atomic force microscope". *Journal of biomechanics* 45.2 (2012), pp. 304–309.

[124] Tatyana G Kuznetsova, Maria N Starodubtseva, Nicolai I Yegorenkov, Sergey A Chizhik, and Renat I Zhdanov. "Atomic force microscopy probing of cell elasticity". *Micron* 38.8 (2007), pp. 824–833.

[125] Valentin Lulevich, Tiffany Zink, Huan-Yuan Chen, Fu-Tong Liu, and Gang-yu Liu. "Cell mechanics using atomic force microscopy-based single-cell compression". *Langmuir* 22.19 (2006), pp. 8151–8155.

[126] Yue Ding, Guang-Kui Xu, and Gang-Feng Wang. "On the determination of elastic moduli of cells by AFM based indentation". *Scientific reports* 7.1 (2017), p. 45575.

[127] *BioNumbers - Harvard University*. 2023. URL: `https://bionumbers.hms.harvard.edu/`.

[128] EA Fadlun, Roberto Verzicco, Paolo Orlandi, and J Mohd-Yusof. "Combined immersed-boundary finite-difference methods for three-dimensional complex flow simulations". *Journal of computational physics* 161.1 (2000), pp. 35–60.

[129] Marcos Vanella and Elias Balaras. "Short note: A moving-least-squares reconstruction for embedded-boundary formulations". *Journal of Computational Physics* 228.18 (2009), pp. 6617–6628.

[130] DJ Jeffrey and RM Corless. "Forces and stresslets for the axisymmetric motion of nearly touching unequal spheres". *PhysicoChemHydrodyn* 10 (1988), p. 461.

[131] Laurentiu Pasol, Mohamed Chaoui, Samir Yahiaoui, and François Feuillebois. "Analytical solutions for a spherical particle near a wall in axisymmetrical polynomial creeping flows". *Physics of fluids* 17.7 (2005), p. 073602.

[132] R Verzicco and G Querzoli. "On the collision of a rigid sphere with a deformable membrane in a viscous fluid". *Journal of fluid mechanics* 914 (2021), A19.

[133] Roland Glowinski, T-W Pan, Todd I Hesla, and Daniel D Joseph. "A distributed Lagrange multiplier/fictitious domain method for particulate flows". *International Journal of Multiphase Flow* 25.5 (1999), pp. 755–794.

[134] Anil Rao. *Dynamics of particles and rigid bodies: a systematic approach*. Cambridge University Press, 2006.

[135] Roberto Zenit and Melany L Hunt. "Mechanics of immersed particle collisions" (1999).

[136] Howard Brenner. "The slow motion of a sphere through a viscous fluid towards a plane surface". *Chemical engineering science* 16.3-4 (1961), pp. 242–251.

[137] R Verzicco and Paolo Orlandi. "A finite-difference scheme for three-dimensional incompressible flows in cylindrical coordinates". *Journal of Computational Physics* 123.2 (1996), pp. 402–414.

[138] Paolo Orlandi. *Fluid flow phenomena: a numerical toolkit*. Vol. 55. Springer Science & Business Media, 2000.

[139] John Kim and Parviz Moin. “Application of a fractional-step method to incompressible Navier-Stokes equations”. *Journal of computational physics* 59.2 (1985), pp. 308–323.

[140] Baohua Ji and Gang Bao. “Cell and molecular biomechanics: perspectives and challenges”. *Acta Mechanica Solida Sinica* 24.1 (2011), pp. 27–51.

[141] J Li, M Dao, CT Lim, and Subra Suresh. “Spectrin-level modeling of the cytoskeleton and optical tweezers stretching of the erythrocyte”. *Biophysical journal* 88.5 (2005), pp. 3707–3719.

[142] JC Hansen, R Skalak, S Chien, and A Hoger. “Influence of network topology on the elasticity of the red blood cell membrane skeleton”. *Biophysical journal* 72.5 (1997), pp. 2369–2381.

[143] Saša Svetina, Drago Kuzman, Richard E Waugh, Primož Ziherl, and Boštjan Žekš. “The cooperative role of membrane skeleton and bilayer in the mechanical behaviour of red blood cells”. *Bioelectrochemistry* 62.2 (2004), pp. 107–113.

[144] Dmitry A Fedosov, Bruce Caswell, and George Em Karniadakis. “Systematic coarse-graining of spectrin-level red blood cell models”. *Computer Methods in Applied Mechanics and Engineering* 199.29-32 (2010), pp. 1937–1948.

[145] Wolfgang Helfrich. “Elastic properties of lipid bilayers: theory and possible experiments”. *Zeitschrift für Naturforschung c* 28.11-12 (1973), pp. 693–703.

[146] CT Lim, EH Zhou, and ST Quek. “Mechanical models for living cells—a review”. *Journal of biomechanics* 39.2 (2006), pp. 195–216.

[147] Robert M Hochmuth. “Micropipette aspiration of living cells”. *Journal of biomechanics* 33.1 (2000), pp. 15–22.

[148] JZ Wu and W Herzog. “Finite element simulation of location-and time-dependent mechanical behavior of chondrocytes in unconfined compression tests”. *Annals of biomedical engineering* 28 (2000), pp. 318–330.

[149] Karel Svoboda, Christoph F Schmidt, Daniel Branton, and Steven M Block. “Conformation and elasticity of the isolated red blood cell membrane skeleton”. *Biophysical journal* 63.3 (1992), pp. 784–793.

[150] Alexander Mietke, Oliver Otto, Salvatore Girardo, Philipp Rosendahl, Anna Taubenberger, et al. “Extracting cell stiffness from real-time deformability cytometry: theory and experiment”. *Biophysical journal* 109.10 (2015), pp. 2023–2036.

[151] Luana Scheffer, Arkady Bitler, Eshel Ben-Jacob, and Rafi Korenstein. “Atomic force pulling: probing the local elasticity of the cell membrane”. *European Biophysics Journal* 30.2 (2001), pp. 83–90.

[152] Gidon Ofek, Roman M Natoli, and Kyriacos A Athanasiou. “In situ mechanical properties of the chondrocyte cytoplasm and nucleus”. *Journal of biomechanics* 42.7 (2009), pp. 873–877.

[153] Nathalie Caille, Olivier Thoumine, Yanik Tardy, and Jean-Jacques Meister. “Contribution of the nucleus to the mechanical properties of endothelial cells”. *Journal of biomechanics* 35.2 (2002), pp. 177–187.

[154] Subra Suresh, J Spatz, John P Mills, Alexandre Micoulet, Ming Dao, et al. "Connections between single-cell biomechanics and human disease states: gastrointestinal cancer and malaria". *Acta biomaterialia* 1.1 (2005), pp. 15–30.

[155] Vinay Swaminathan, Karthikeyan Mythreye, E Tim O'Brien, Andrew Berchuck, Gerard C Blobe, et al. "Mechanical stiffness grades metastatic potential in patient tumor cells and in cancer cell linesmechanical stiffness of cells dictates cancer cell invasion". *Cancer research* 71.15 (2011), pp. 5075–5080.

[156] Valentin Gensbittel, Martin Kräter, Sébastien Harlepp, Ignacio Busnelli, Jochen Guck, et al. "Mechanical adaptability of tumor cells in metastasis". *Developmental cell* 56.2 (2021), pp. 164–179.

[157] Sebastian J Müller, Franziska Weigl, Carina Bezold, Christian Bächer, Krystyna Albrecht, et al. "A hyperelastic model for simulating cells in flow". *Biomechanics and modeling in mechanobiology* 20 (2021), pp. 509–520.

[158] Masao Tanaka, Shigeo Wada, and Masanori Nakamura. *Computational biomechanics: theoretical background and biological/biomedical problems*. Vol. 3. Springer Science & Business Media, 2012.

[159] Allen Van Gelder. "Approximate simulation of elastic membranes by triangulated spring meshes". *Journal of graphics tools* 3.2 (1998), pp. 21–41.

[160] Yacov Kantor and David R Nelson. "Phase transitions in flexible polymeric surfaces". *Physical Review A* 36.8 (1987), p. 4020.

[161] David H Boal and Madan Rao. "Topology changes in quid membranes" (1992).

[162] Stephen Timoshenko, Sergius Woinowsky-Krieger, et al. *Theory of plates and shells*. Vol. 2. McGraw-hill New York, 1959.

[163] Julien Sigüenza, Simon Mendez, and Franck Nicoud. "How should the optical tweezers experiment be used to characterize the red blood cell membrane mechanics?": *Biomechanics and modeling in mechanobiology* 16 (2017), pp. 1645–1657.

[164] Margarita Staykova, Douglas P Holmes, Clarke Read, and Howard A Stone. "Mechanics of surface area regulation in cells examined with confined lipid membranes". *Proceedings of the National Academy of Sciences* 108.22 (2011), pp. 9084–9088.

[165] David Steigmann, Eveline Baesu, Robert E Rudd, Jim Belak, and Mike McElfresh. "On the variational theory of cell-membrane equilibria". *Interfaces and Free Boundaries* 5.4 (2003), pp. 357–366.

[166] Jongho Lee, Jungwoo Kim, Haecheon Choi, and Kyung-Soo Yang. "Sources of spurious force oscillations from an immersed boundary method for moving-body problems". *Journal of computational physics* 230.7 (2011), pp. 2677–2695.

[167] Markus Uhlmann. "An immersed boundary method with direct forcing for the simulation of particulate flows". *Journal of computational physics* 209.2 (2005), pp. 448–476.

[168] Jianming Yang and Elias Balaras. "An embedded-boundary formulation for large-eddy simulation of turbulent flows interacting with moving boundaries". *Journal of Computational Physics* 215.1 (2006), pp. 12–40.

[169] L Gary Leal. *Advanced transport phenomena: fluid mechanics and convective transport processes*. Vol. 7. Cambridge University Press, 2007.

[170] Norman R Draper and Harry Smith. *Applied regression analysis*. Vol. 326. John Wiley & Sons, 1998.

[171] Tong Gao, Howard H Hu, and Pedro Ponte Castañeda. "Rheology of a suspension of elastic particles in a viscous shear flow". *Journal of fluid mechanics* 687 (2011), pp. 209–237.

[172] Young Bok Bae, Hye Kyeong Jang, Tae Hwan Shin, Geetika Phukan, Thanh Tinh Tran, et al. "Microfluidic assessment of mechanical cell damage by extensional stress". *Lab on a Chip* 16.1 (2016), pp. 96–103.

[173] Daniel XB Chen and Daniel XB Chen. *Extrusion bioprinting of scaffolds*. Springer, 2019.

[174] Liqun Ning and Xiongbiao Chen. "A brief review of extrusion-based tissue scaffold bio-printing". *Biotechnology journal* 12.8 (2017), p. 1600671.

[175] Marco Costantini, Cristina Colosi, Wojciech Swieszkowski, and Andrea Barbetta. "Co-axial wet-spinning in 3D bioprinting: state of the art and future perspective of microfluidic integration". *Biofabrication* 11.1 (2018), p. 012001.

[176] Marco Costantini, Stefano Testa, Pamela Mozetic, Andrea Barbetta, Claudia Fuoco, et al. "Microfluidic-enhanced 3D bioprinting of aligned myoblast-laden hydrogels leads to functionally organized myofibers in vitro and in vivo". *Biomaterials* 131 (2017), pp. 98–110.

[177] Zhe Fan, Feng Qiu, Arie Kaufman, and Suzanne Yoakum-Stover. "GPU cluster for high performance computing". *SC'04: Proceedings of the 2004 ACM/IEEE conference on Supercomputing*. IEEE. 2004, pp. 47–47.

[178] Mario Vestias and Horácio Neto. "Trends of CPU, GPU and FPGA for high-performance computing". *2014 24th International Conference on Field Programmable Logic and Applications (FPL)*. IEEE. 2014, pp. 1–6.